AFRL-RQ-WP-TR-2017-0152

EXPLORING CAPABILITIES OF ELECTRICAL CAPACITANCE TOMOGRAPHY SENSOR AND VELOCITY ANALYSIS OF TWO-PHASE R-134A FLOW THROUGH A SUDDEN EXPANSION

Joseph Michael Cronin

University of Dayton Research Institute

MAY 2017
Interim Report

AIR FORCE RESEARCH LABORATORY
AEROSPACE SYSTEMS DIRECTORATE
WRIGHT-PATTERSON AIR FORCE BASE, OH 45433-7542
AIR FORCE MATERIEL COMMAND
UNITED STATES AIR FORCE

NOTICE AND SIGNATURE PAGE

This paper was cleared for public release by the USAF 88th Air Base Wing (88 ABW) Public Affairs Office (PAO) and is available to the general public, including foreign nationals.

Copies may be obtained from the Defense Technical Information Center (DTIC) (http://www.dtic.mil).

AFRL-RQ-WP-TR-2017-0152 has been reviewed and is approved for publication in accordance with assigned distribution statement.

*//Signature//
TRAVIS E. MICHALAK
Program Engineer
Mechanical and Thermal Systems Branch
Power and Control Division

//Signature//
EARL M. GREGORY, Technical Advisor
Mechanical and Thermal Systems Branch
Power and Control Division
Aerospace Systems Directorate

//Signature//
JOHN G. NAIRUS, Chief Engineer
Power and Control Division
Aerospace Systems Directorate

REPORT DOCUMENTATION PAGE

Form Approved
OMB No. 0704-0188

1. REPORT DATE *(DD-MM-YY)*	2. REPORT TYPE	3. DATES COVERED *(From - To)*
May 2017	Interim	01 January 2015 – 30 April 2017

4. TITLE AND SUBTITLE
EXPLORING CAPABILITIES OF ELECTRICAL CAPACITANCE TOMOGRAPHY SENSOR AND VELOCITY ANALYSIS OF TWO-PHASE R-134A FLOW THROUGH A SUDDEN EXPANSION

5a. CONTRACT NUMBER
In-house

5b. GRANT NUMBER

5c. PROGRAM ELEMENT NUMBER
62203F

6. AUTHOR(S)
Joseph Michael Cronin

5d. PROJECT NUMBER
3145

5e. TASK NUMBER

5f. WORK UNIT NUMBER
Q0LA

7. PERFORMING ORGANIZATION NAME(S) AND ADDRESS(ES)
University of Dayton Research Institute
300 College Park Avenue
Dayton, OH 45469

8. PERFORMING ORGANIZATION REPORT NUMBER
AFRL-RQ-WP-TR-2017-0152

9. SPONSORING/MONITORING AGENCY NAME(S) AND ADDRESS(ES)
Air Force Research Laboratory
Aerospace Systems Directorate
Wright-Patterson Air Force Base, OH 45433-7542
Air Force Materiel Command
United States Air Force

10. SPONSORING/MONITORING AGENCY ACRONYM(S)
AFRL/RQQM

11. SPONSORING/MONITORING AGENCY REPORT NUMBER(S)
AFRL-RQ-WP-TR-2017-0152

12. DISTRIBUTION/AVAILABILITY STATEMENT
DISTRIBUTION STATEMENT A: Approved for public release. Distribution is unlimited.

13. SUPPLEMENTARY NOTES
PA Case Number: 88ABW-2017-2296; Clearance Date: 15 May 2015.
This thesis is in partial fulfillment of the requirements for the degree of Master of Science in Mechanical Engineering to University of Dayton Research Institute in 2017. This is a work of the U.S. Government and is not subject to copyright protection in the United States.

14. ABSTRACT
Future high-performance aircraft will require advances in the understanding of two-phase heat transfer in order to manage the ever-increasing airframe and engine heat loads. Two-phase liquid-vapor refrigerant systems are one solution for the heat removal from these systems. However, they require more study before implementation. This study examines the velocities of two-phase liquid-vapor flows with the use of high speed visualization. In flow channels where high speed visualization cannot be used, there are other noninvasive techniques for analyzing flow the flow, such as electrical capacitance tomography (ECT). In this thesis, capabilities of ECT sensors such as the location in the sensor where there is a detected change in permittivity as well as the sensor's ability of determining simple surfaces are explored to assist in future work. Four sensors were tested and static experiments were able to determine location along the length of the sensor where a change in permittivity was detected. Each sensor tested showed a detection of permittivity at a different location than expected when comparing with the physical location of the electrodes according to the dimensional drawings of the sensors. Experiments testing the sensor's ability to detect a surface showed that with a well-defined surface there was a noticeable change when the surface was rotated to different orientations. In fluid flow tests, high speed video analysis showed the velocities of 71 tracked points at varying level of qualities. These velocities were analyzed and the data from these experiments were compared with pressure drop correlations.

15. SUBJECT TERMS thermal management, two-phase flow, flow visualization, electric capacitance tomography

16. SECURITY CLASSIFICATION OF:			17. LIMITATION OF ABSTRACT:	18. NUMBER OF PAGES	19a. NAME OF RESPONSIBLE PERSON (Monitor)
a. REPORT Unclassified	**b. ABSTRACT** Unclassified	**c. THIS PAGE** Unclassified	SAR	80	Travis E. Michalak
					19b. TELEPHONE NUMBER *(Include Area Code)* N/A

Standard Form 298 (Rev. 8-98)
Prescribed by ANSI Std. Z39-18

Dedicated to my family.

TABLE OF CONTENTS

LIST OF FIGURES

Figure **Page**

LIST OF TABLES

LIST OF ABBREVIATIONS AND SYMBOLS

α	void fraction
Δ%	change in percentage
ΔP	change in pressure (Pa)
ECT	electrical capacitance tomography
ε	permittivity (F/m)
$\varepsilon_{Theoretical}$	theoretical permittivity (F/m)
$\varepsilon_{Theoretical,upper}$	theoretical permittivity of upper half of angled surface(F/m)
$\varepsilon_{Theoretical,lower}$	theoretical permittivity of lower half of angled surface (F/m)
fps	frames per second
G	mass flux ($\frac{kg}{m^2 s}$)
HDR	high dielectric reconstruction
ID	inner diameter (mm)
$\frac{kg}{m^2 s}$	kilograms per cubic meter
$L_{electrode}$	length of electrode (mm)
L_{plug}	length of plug inserted inside sensor (mm)
L_{sensor}	length of sensor (mm)
LBP	linear back projection
mm	millimeters
μ_l	dynamic liquid viscosity (Ns/m^2)
μ_v	dynamic vapor viscosity (Ns/m^2)
σ_A	area ratio
φ	angle of rod
ρ_l	density of liquid phase (kg/m^3)
ρ_v	density of vapor phase (kg/m^3)
Re_l	liquid Reynolds number
Re_v	vapor Reynolds number
V_{lower}	volume of lower half of angled surface experiment (m^3)
V_{upper}	volume of upper half of angled surface experiment (m^3)
Z_{edge}	length from edge of sensor to edge of electrode (mm)

CHAPTER 1
INTRODUCTION

Future aircraft electronics, weapons systems, and environmental control systems will generate more heat and, thus, require advanced thermal management systems (Chen et al., 2012). Two-phase liquid-vapor refrigerant systems can potentially provide a solution to solving thermal management problems as they arise with new aircraft designs. An important step in the development of two-phase thermal management systems is being able to understand how varying physical parameters affect the flow and heat transfer. This task is further complicated by the existence of multiple flow patterns which may occur with two-phase flow. Two-phase flow can be categorized into different flow patterns based on the amount and distribution of each phase present in the flow. (Thome, 2010). In order to select and use appropriate heat transfer correlations for two-phase systems, knowledge of the flow patterns inside of the system is necessary (Thome, 2010). Experiments may be performed using electrical capacitance tomography (ECT) and high speed visualization to help provide an improved understanding of liquid-vapor flows.

Previous investigations have studied two-phase flow characteristics involving sudden expansions. (Chen et al., 2007; Ahmed et al., 2008; Ahmed et al., 2007; Pakhomov and Terekhov, 2016; Yin et al., 2014; Balakhrisna et al., 2010; Wang et al., 2010; Hwang et al., 1997). Some of these previous studies involved two-phase air-oil mixtures (Ahmed et al., 2007; Ahmed et al., 2008), air-water mixtures (Chen et al., 2007; Yin et al., 2014), or oil-water mixtures (Hwang et al., 1997; Balakhrisna et al., 2010). However the behavior of refrigerants, rather than air-oil, air-water, or oil-water mixtures, has been less studied and is of recent interest for the design of advanced, high performance aircraft. Moreover, the pressure drop may strongly influence the transition between the liquid and vapor phases as R-134a flows through a passage. The current work studies the flow of liquid-vapor R-134a through a sudden expansion. The sudden expansion in this experiment consists of a 7 mm inner diameter (ID) tube that abruptly increases to a 10.5mm ID tube. This is in contrast to the previous investigations that studied the merging of round tubes into rectangular channels (Chen et al., 2007), or abrupt expansions using different sized tube diameters than were studied in this work (Ahmed et al., 2007; Ahmed et al., 2008; Pakhomov and Terekhov, 2016; Yin et al., 2014; Balakhrisna, 2009; Hwang et al., 1997).

In the present research, electrical capacitance tomography (ECT) is used to measure the void fraction and study two-phase characteristics. Capacitance sensors have been used in previous investigations to distinguish between phases in two-phase liquid-vapor flows (Warsito and Fan, 2001; Huang et al., 2003; Caniere et al., 2008; Caniere et al., 2010). The ECT sensor takes measurements of the electrical capacitance within the flow by measuring the voltage differences between electrodes. From these voltage differences the distributions of the permittivity can be calculated (Loser et al., 2001). This is ideal for a two-phase flow where the liquid and vapor phases differ in permittivity. The permittivity distribution within the tube corresponds to the distribution of the liquid and vapor volumes within the tube. Several different methods have been explored in the past on how to convert a permittivity distribution into a digital image (Yang and Peng, 2002; Loser et al., 2001) which is of interest in this thesis.

Other technologies, such as electrical resistance tomography (ERT) and x-rays, have been used to determine the phase distribution (Cui et al., 2009; Tan et al., 2007; Hu et al., 2014; Kendoush and Sarkis, 2002). ERT is limited to use in aqueous-based systems (Cui et al., 2009). Since R-134a has a relatively low electrical conductivity, ERT technology was dismissed from

consideration in this study. X-ray systems have inherent dangers with safety concerns, ruling out this technology for the present work (Hu et al., 2014). This led to the use of ECT sensors in the current research as they are safe, compatible with R-134a, and noninvasive.

This thesis focuses on using ECT sensors to characterize the two-phase refrigerant flow. One objective was to explore the measurement capabilities of the ECT using salt and angled wooden rods. These experiments attempted to determine the region in which the electrode is able to detect a known, well-defined change in permittivity as well as the capabilities to define interfaces between phases. The salt experiments sought to determine the region in which the sensor electrodes were able to define the salt boundary caused by the permittivity difference between the salt and air. Salt was chosen because its dielectric constant values are similar to those of R-134a (Barao, T., 1995; Clipper Controls, 2016). The angled surface studies sought to determine the capacity of the sensor to define different surface shapes. The wood used in these experiments was covered in masking tape in order to match the inner diameter of the sensor. In addition, paper of the masking tape has a permittivity value similar to that of R-134a (Barao, T., 1995, Clipper Controls, 2016).

Visualization of horizontal two-phase flow has been considered previously (Chen et al., 2008, Ahmed et al., 2008). Additionally, the combination of capacitance sensors and high speed videos have been used to identify flow regimes in two-phase flow (Caniere et al., 2008). However unlike the previous investigations, this work was performed using liquid-vapor R-134a as opposed to air-water or air-oil mixtures. The present work included visualization with the use of a high speed camera. Another objective of this thesis was to use flow visualization to study a horizontal sudden expansion involving liquid-vapor R-134a with a high speed camera and motion analysis software.

CHAPTER 2
EXPERIMENTAL

The previous chapter provided the background information on two-phase refrigerant flow, the use of ECT sensors, and the goals for this work. The experimental and computational procedures used to obtain and process the output from the ECT sensor are described in this chapter. The first section of this chapter provides a physical description of the ECT sensor as well as a description of how the sensor works. The second section describes a test to measure the dimensional capabilities of the sensor, and the third section details an experiment to characterize the ability of the ECT System to define interface shapes. The fourth section discusses computational methods used to process the data obtained from the experiments.

2.1 Electrical capacitance tomography

Electrical capacitance tomography (ECT) is a measurement technique that was developed in the 1980s for characterizing flows containing multiple phases which have different permittivity values (Huang et al., 1988; Xie et al., 1989). The ECT system measures the difference in capacitance within a two-phase flow and calculates the related difference in permittivity between the phases (Clark, et al., 2015). A two-dimensional cross sectional image of the permittivity distribution in the flow channel is then constructed using reconstruction algorithms (Yang, 1996). Since initial development, the technology has improved in terms of accuracy and speed of measurement. The ECT system consists of three main components: a sensor, electronic circuitry for capacitance measurement, and a computer which controls and stores the measurements. In addition the computer is used to reconstruct the tomographic image (Loser et al., 2001; Yang, 1996 225). In this thesis work, the linear back projection (LBP) and high dielectric reconstruction (HDR) reconstruction algorithms were used to generate the tomogram. These algorithms were built into the software developed by the sensor manufacturer (Industrial Tomography Systems, 2010). LBP algorithms are typically used with tomography as it is a fast process that can allow live updates. HDR algorithms are typically used for high dielectric media such as water, however the algorithms typically produce accurate averages, as the algorithm reduces sensitivity between neighboring electrodes to focus on the media in the flow channel. This results in an improved average at the sacrifice of a less accurate local section on the edges of the tomogram. Details of these reconstruction techniques can be found elsewhere (Dyakowski et al., 2000; Yang and Peng, 2002; Jaworski and Bolton, 2000). The sensors are built around the flow channel and measure the capacitance values between pairs of electrodes. ECT sensors typically consist of a set of either 8, 12, or 16 electrodes mounted around the flow channel. The electrodes have radial and axial shielding to homogenize the electrical field lines inside the sensor in order to create a quasi-two-dimensional measurement within the flow volume (Loser et al., 2001). In this research, an 8 electrode sensor was used. Figure 2.1a shows the orientation of electrodes which probe the flow and the axial shield. Figure 2.1b shows the cross sectional distribution of the eight electrodes as well as the insulation and shielding surrounding the flow channel.
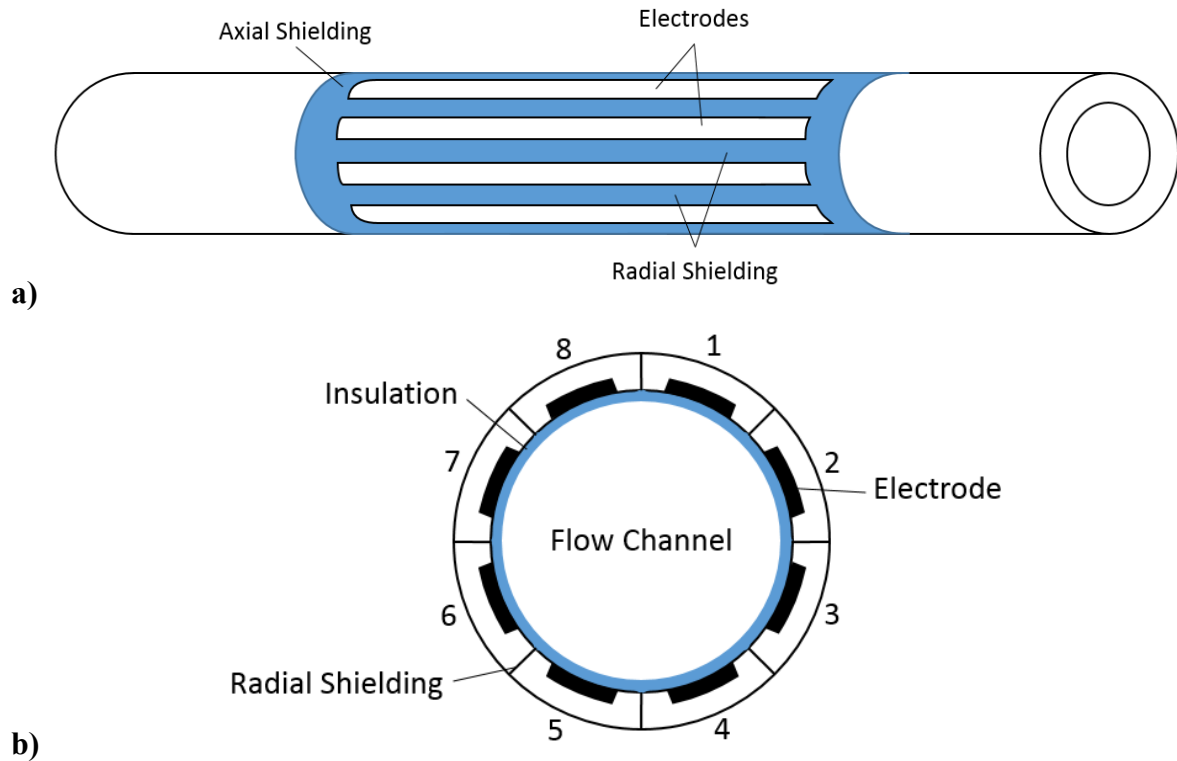
Figure 2.1: Schematic of ECT Sensor: a) view of tube exterior and b) cross-sectional view.

The measurement process begins in an 8 electrode sensor with the application of a voltage to electrode 1. This electrode becomes the sending electrode and electrodes 2-8 each become the receiving electrode in the electrode pairs, measuring the capacitance through the flow channel. A voltage is applied to electrode 2, and electrodes 3-8 measure the capacitance in the flow channel. This process is repeated around the sensor for each electrode pair until a total of 28 measurements are taken. The electric field inside the ECT is interpreted by the capacitance measurement circuit based on the change in permittivity in the flow in between each electrode pair. The measured capacitances are recorded by the computer which processes the capacitance measurements and ultimately calculates a tomogram. Details of the measurement process can be found elsewhere. (Loser et al., 2001; Yang, 1996; Yang, 2010).

The tomogram displays the normalized distribution of the permittivity in 812 pixels displayed in a circular shape to represent the cross section of the measured volume from the sensor. These pixels are derived from voxels which are volume elements. The three-dimensional voxel recorded by the electrodes is a function of the pixel height, width, and time. These voxels are averaged along the length of the sensor to produce a two-dimensional tomogram pixel. Together, these 812 pixels form a tomogram image representative of the permittivity distribution inside the sensor (Industrial Tomography Systems, 2010). The tomogram showing the distribution of the permittivity, ε, is constructed through normalization of the ECT measurements for each voxel. The reconstruction algorithm creates a numerical value for ε with a range of 0 to 1, with $\varepsilon = 0$ for a measurement containing only vapor and $\varepsilon = 1$ for one comprised entirely of liquid. Since a volume is measured, voxels can contain a mixture of liquid and vapor. For these transition voxels, a value between 0 and 1 is assigned based on the amount of each phase in the measured voxel. Figure 2.2 shows an example of a tomogram. In this tomogram image, the blue

4

represents vapor, the red represents liquid, and the yellow and gradient colors between blue and red represent the transition measurement voxels.
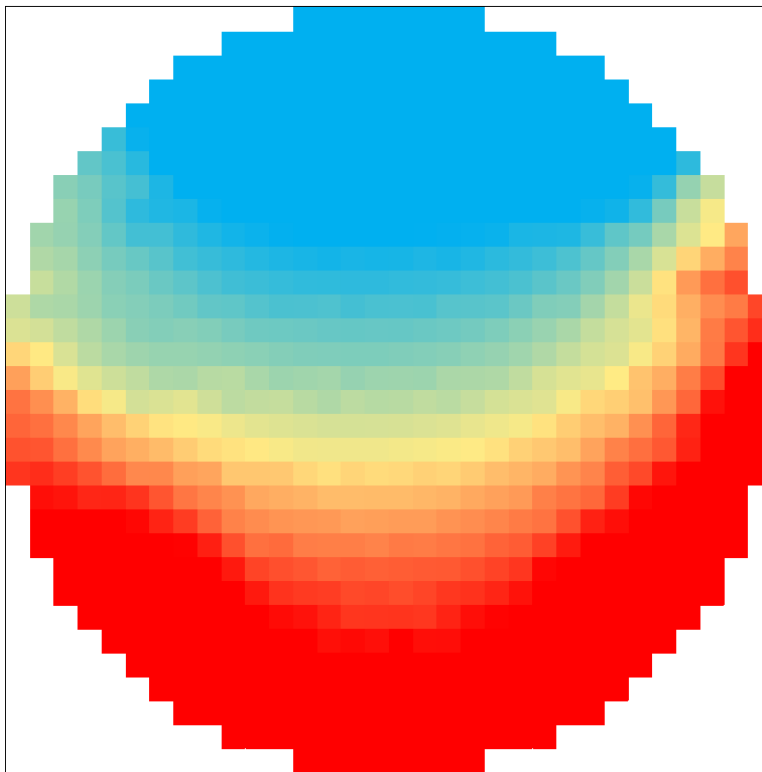
Figure 2.2: Tomography showing liquid and vapor with a transition phase in between.

2.2 ECT Permittivity Measurement

Permittivity measurements were performed to determine the measurement capabilities of the ECT sensor. The first experiment involved salt filled to specified heights inside of the sensor. This experiment attempted to determine the region in which the electrodes of the sensor were able to detect a known change in permittivity caused by the addition of salt into an empty sensor. Salt was chosen because it has dielectric constant values that are similar to R-134a (Clipper Controls, 2016). Two sensors with an inner diameter of 7 millimeters (mm) were used along with two sensors with an inner diameter of 10.5 mm.

2.2.1 Electrode Locating Experiment

For this experiment, the sensor was secured in a vertical orientation and was capped on one end using a stainless steel threaded high-pressure pipe plug. The technical drawings showed the physical location of the electrodes, but in order to detect fringing effects, small increments in salt volume were added to find the location in each sensor where a change in permittivity was detected (Naini and Green, 1977). The height of each level of salt was measured with a wooden rod either in 4.5 mm or 9.25 mm diameters, for the 7 mm and 10.5 mm sensors respectively, marked with height measurements every 2.5 mm. The rod was also used to pack down the salt and ensure a level surface before measurements were taken with the ECT. Figure 2.3 shows the schematic of the sensor containing salt. The length of the electrode varies with the inner diameter of the sensor. The 7 mm ID sensor has electrodes 55 mm long and the 10.5 mm ID sensor has electrodes 45 mm long. Each edge of the electrodes was located by adding salt from both ends of

the sensor to determine where each edge of the sensor was detecting the change in permittivity. This test resulted in quantifying the distance from the edge of the sensor to the edge of the electrodes as described in Figure 2.4.
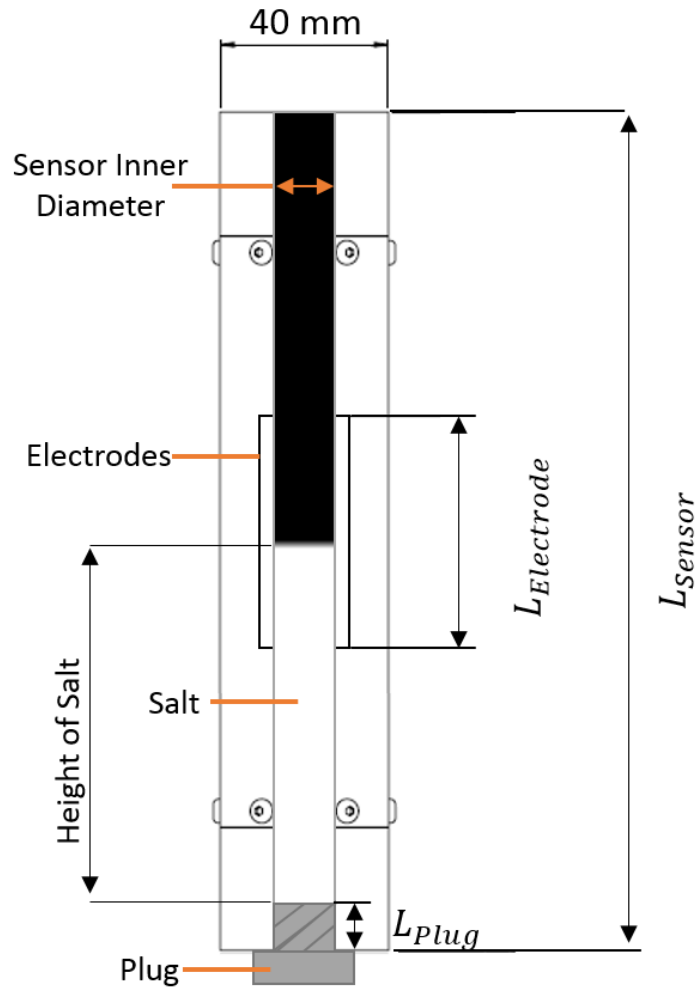
Figure 2.3: Schematic of the sensor with salt in the electrode locating experiment.
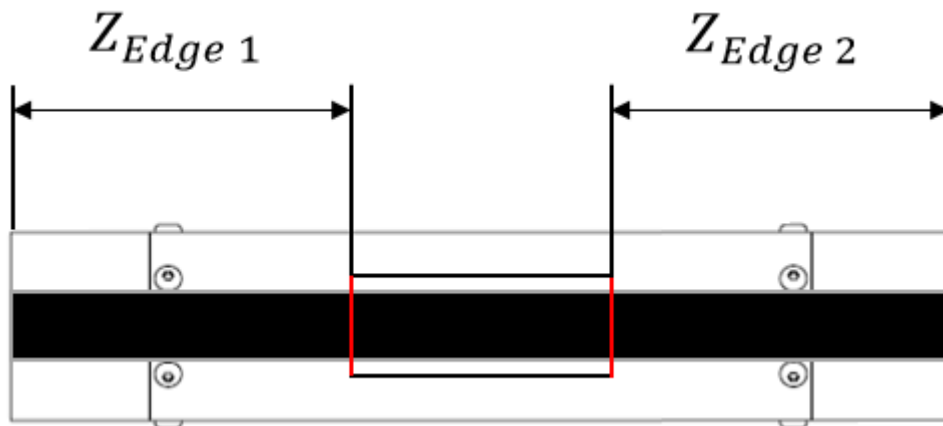
Figure 2.4: Physical distances on ECT sensor calculated from the electrode locating experiment.

2.2.2 Angled Surface Experiment

Another experiment that was performed involved angled surfaces of salt and wood. This experiment sought to determine the ability of the ECT system to define different surfaces. Two wooden rods were fabricated, one with an end cut at 30 degrees and the other with an end cut at 45 degrees. The angles of the rods were more accurately measured with TEMA software and were found to be 30.30°±0.25° and 45.89°±0.27°, respectively. The exterior of the wooden rod was wrapped in masking tape in order to match the inner diameter of the sensor. The masking tape paper and wood samples have permittivity values similar to R-134a (8). Two marks were made on the centerline of wooden rods 180° apart from one another to determine their orientation of the angle. Figure 2.5 shows the wooden rods used in this experiment.
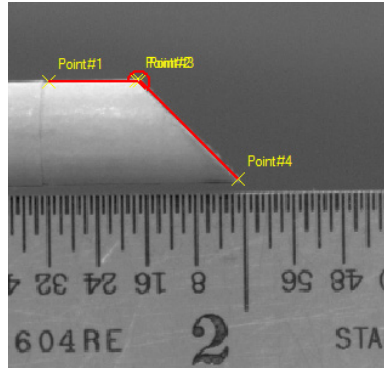
a) 45° wooden rod.
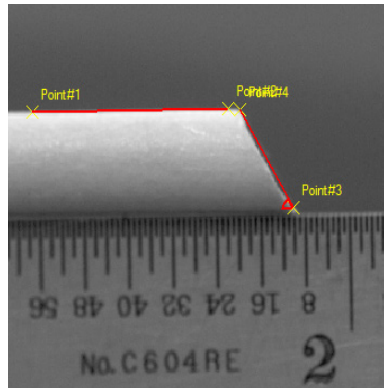
b) 30° wooden rod.

c) 30° and 45° wooden rods.

Figure 2.5: Angled wooden rods used to measure ECT capabilities
a) TEMA angle measurement of end of 45° wooden rod b) TEMA angle measurement of end of 30° wooden rod c) 45° and 30° wooden rods.

    Experiments with the angled surface were conducted with only the wooden rod inside the sensor or tests only containing salt inside the sensor. The trials with salt included filling the sensor with salt halfway similar to the salt experiment previously described. Before the measurement was taken, an angled wooden rod was inserted to mold the surface of the salt into

the desired angle. Since the salt and wood have similar permittivity values to one another, the wooden rod was removed before the ECT measurement was taken, creating an angled surface containing only salt. For the wood only experiment, horizontal marks were added to the rod to ensure the depth was consistent with each measurement. This experiment involved lowering the angled rod into the empty ECT sensor a specified depth and measuring the known surface with the sensor. ECT measurements with both salt and wood were taken in two different orientations for each angle. The first orientation was taken with the long edge of the sensor along the top of the ECT, and the second orientation was rotated 180° from the previous with the short edge along the top of the ECT. This provided four different surfaces for the sensor to evaluate. Figure 2.6 shows a schematic of the angled wood sample.
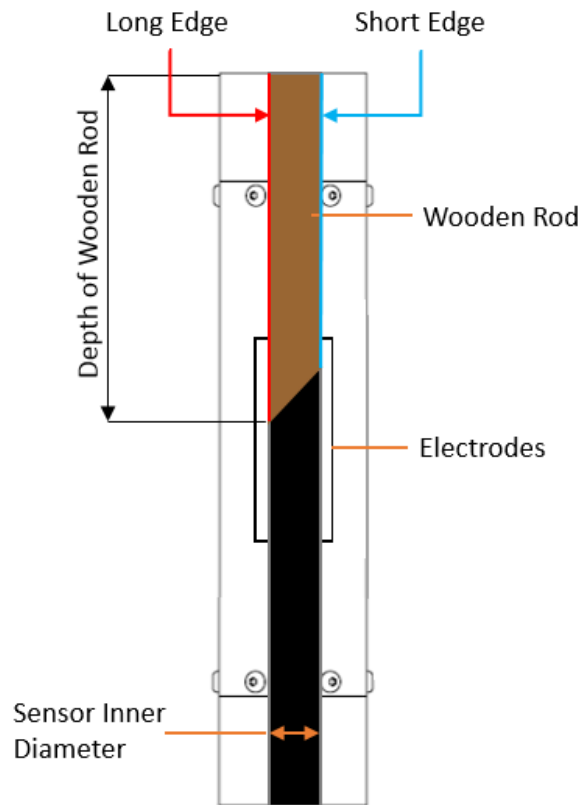
Figure 2.6: Schematic of angled wood sample together with the ECT sensor.

2.3   TEMA Expansion Velocity Measurements

The horizontal two-phase flow expansion study used a high speed camera for visualizing the flow. Flow visualization using a high speed camera is a more effective method than standard visualization observation for understanding flow because it can be played back in slow motion which assists in observation and analysis. The camera used was a Vision Research Phantom v4.2 high speed camera. This model is capable of capturing the two-phase system at up to 2,100 frames per second (fps) at 512 x 512 pixels and can be increased up to 90,000 fps when using smaller frame sizes (Phantom v4.2 Datasheet). For this work, videos were captured at 2900 fps with a resolution of 512 x 384 and an exposure of 310 microseconds for analysis. The lighting that was used in this work consisted of four model 900415 Visual Instrumentation Corporation single LED module lights controlled by a model 200950G Visual Instrumentation Corporation

controller. This frame rate and exposure were selected to provide the clearest videos for the available light intensity and lens capabilities, while still providing an adequate frame rate for high speed analysis.

TEMA Motion Analysis (TEMA) software was used to analyze the videos and determine an object's position, velocity, and acceleration. A detailed account of the capabilities as well as a tutorial on the software's use can be found in Appendix B. High speed video in combination with TEMA was used to analyze two-phase flow of R-134a through an abrupt expansion. The expansion used in these experiments was fabricated from fused quartz tubing and had an internal diameter of 7 mm which abruptly increased to a 10.5 mm internal diameter. This expansion results in an area ratio (σ_A) of 0.444 which is similar to area ratios studied elsewhere (Ahmed et al., 2008). The flows used to generate the data for this had a steady mass flux of $262 \pm 4 \frac{kg}{m^2 s}$ while the heater power was varied from 13-900 watts to produce two-phase flows of different qualities ranging from 0.002 to 0.489. The flow system configuration with the sudden expansion can be seen in Figure 2.7.
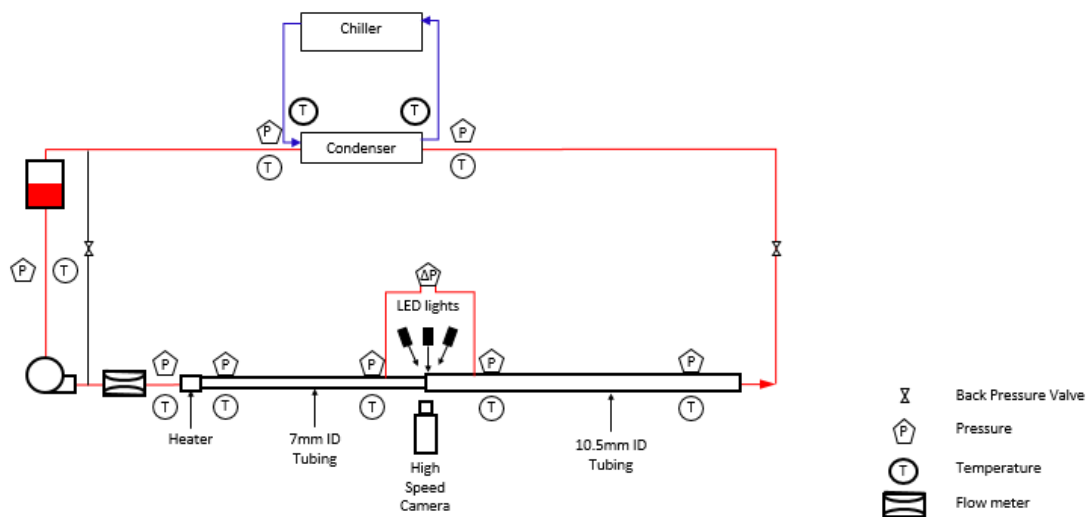
Figure 2.7: Laboratory setup for two-phase R-134a flow through sudden expansion and high speed video recording.

2.4   Computational Methods Used To Process The Measurements

Measurements from the salt experiment were analyzed using the numerical values from the tomogram produced by the ECT system. At each height of salt, a collection of roughly 100 frames were recorded by the ECT system. Each frame consists of 812 unique numerical values representing each pixel on the tomogram. In order to facilitate data processing, an average value for each frame was calculated from the tomogram data in order to filter out possible artifacts in the sensor or to filter out areas where the level of salt was not entirely flat. An artifact with the ECT sensors used in this test can be characterized as a false high capacitance reading in a concentrated area along the edge of the tomogram. This results because of the high sensitivity between neighboring electrodes. These artifacts can typically be remedied with an appropriate sensitivity map provided by the sensor manufacturer or through calibration of the sensor (Loser et al., 2001). However as an extra precaution, filtering was done in order to account for any

possibility of artifacts in the tomogram. In order to compare different heights of salt, an average and standard deviation was calculated from the collection of frames recorded by the ECT. The calculated averages were plotted for each salt height and compared with a theoretical value based on the dimensional drawings from the sensor manufacturer. The numerical data from these plots can be found in Appendix A. This theoretical value, Z_{Edge}, of where the sensor is physically located relative to the end of the sensor, Z_{Edge1} and Z_{Edge2} in Figure 2.4, was recalculated using equation 2.1 to account for the length of the plug inserted into the sensor.

$$Z_{Edge} = (height\ of\ salt) + L_{Plug} \tag{2.1}$$

The value found for Z_{Edge} can then be used to calculate the theoretical permittivity value based on a linear relationship of the permittivity along the electrode length as shown in Equation 2.2. With Equations 2.1 and 2.2, the results from the salt experiment could be compared with theoretical values to determine axially where the sensor detects a change in permittivity, accounting for any physical tolerances as well as fringing effects that may affect each individual sensor.

$$\varepsilon_{Theoretical} = \frac{(height\ of\ salt) - Z_{Edge}}{L_{Electrode}} \tag{2.2}$$

In order to analyze the data from the angled surface experiment, the tomograms created by the ECT were analyzed using a program that recreates the tomogram given the numerical data created by the ECT sensor. Using this program, each frame could be visually analyzed to determine if the sensor was able to detect different surface interfaces. In addition to visual interpretation, the program displays the numerical averages of the quadrants of the tomogram to assist in providing a quantitative analysis of the ECT sensor's ability to recognize the different surfaces.

In order to compare the measured angled surface results with a theoretical value, volume integrals were evaluated for the upper and lower half of the sensor, as shown in Figure 2.8. The volume under the slanted surface at angle ϕ relative to the xy plane is split into upper and lower halves. The volume of each half can be calculated using Equations 2.3 and 2.4. To find the theoretical permittivity one of the halves, the respective volume is divided by the half of the total measured volume as shown in Equations 2.5 and 2.6.
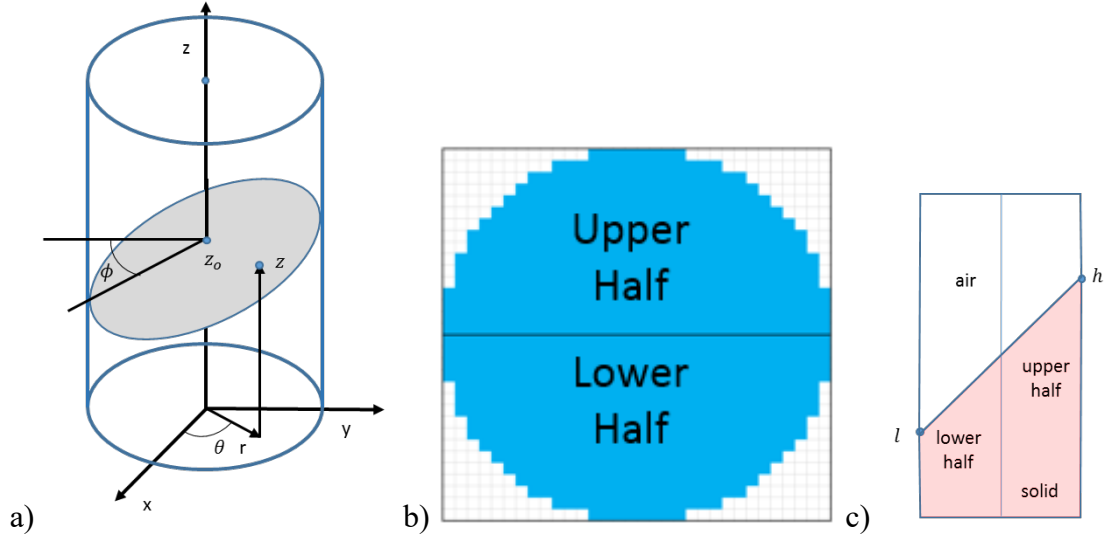
Figure 2.8: Diagrams of angled surface experiment to determine theoretical ε value for angled surface test

a) Schematic of coordinate system used in equations for finding ε. b) Axial view denoting upper and lower halves. c) Side view of upper and lower halves being evaluated in the integrals of Equations 2.3 and 2.4.

$$V_{upper} = \int_{\theta=0}^{\pi} \int_{r=0}^{R} [z_o + \tan(\phi)\, r\sin(\theta)] r\, dr\, d\theta \tag{2.3}$$

$$V_{lower} = \int_{\theta=\pi}^{2\pi} \int_{r=0}^{R} [z_o + \tan(\phi)\, r\sin(\theta)] r\, dr\, d\theta \tag{2.4}$$

$$\varepsilon_{Theoretical,upper} = \frac{V_{upper}}{\left(\frac{V_{total}}{2}\right)} \tag{2.5}$$

$$\varepsilon_{Theoretical,lower} = \frac{V_{lower}}{\left(\frac{V_{total}}{2}\right)} \tag{2.6}$$

Analysis of the horizontal two-phase expansion was done with TEMA software. For each flow of a given vapor quality, the high speed video was analyzed immediately upstream from the expansion in the 7 mm section and 40 diameters downstream from the expansion to capture the fully developed flow (Ahmed et al., 2008). In this study, fully developed flow is defined by flow that is repeating features and is no longer changing. In each of the video recordings, two to six features were tracked that best represented the bulk liquid flow. The velocities of these features were then averaged to form a single value representative of the vapor quality and the diameter of tubing for the observed flow.

CHAPTER 3
RESULTS

In the previous section, the experimental procedures and involved computational methods for data processing were discussed. The results section presents and describes the results from the salt experiment, angled surface experiments, and the two-phase expansion high speed video analysis. The results from the salt experiment were used to determine the physical location in each sensor where the electrodes begin to detect a change in permittivity. This information can be helpful for future studies where a sudden expansion incurs within an ECT sensor. The angled surface experiment was used to help determine the sensor's capability of detecting surface features such as waves inside the sensor. The high speed video analysis provided information on the velocities as the two phase flow traveled through a horizontal sudden expansion.

3.1   Permittivity Measurement Results

An objective of this work was to explore the measurement capabilities of the ECT sensor. This objective was met by conducting the salt and the angled surface experiment. The salt experiment was conducted in order to detect the axial height in each sensor where a change in permittivity was detected by adding salt to an empty sensor. Four sensors were tested, two with an inner diameter of 7 mm and two with an inner diameter of 10.5 mm. The tomograms output from the ECT sensors in each of these tests were reconstructed with LBP and are shown in comparison to the theoretical results in Figure 3.1a-d. The results from this experiment reconstructed with HDR can be found in Appendix A. The plotted values are averaged values of 100 tomogram frames, with values having a standard deviation less than 0.0070 using LBP and a standard deviation less than 0.0050 when using HDR reconstruction. In each of the results from the tests, the height in the Z direction of the sensor, Z_{Edge}, was marked where there was an initial change in permittivity. The theoretical values were calculated from the physical location of the electrodes in the sensor using Equation 2.2 to create theoretical permittivity values throughout the height of the electrode. The raw data from these experiments appears in Appendix A. A minimum threshold of 0.015 was chosen as a numerical value to represent a change in permittivity. This was chosen to filter out noise that occurred throughout experimentation and to ensure that a change in permittivity was being detected.
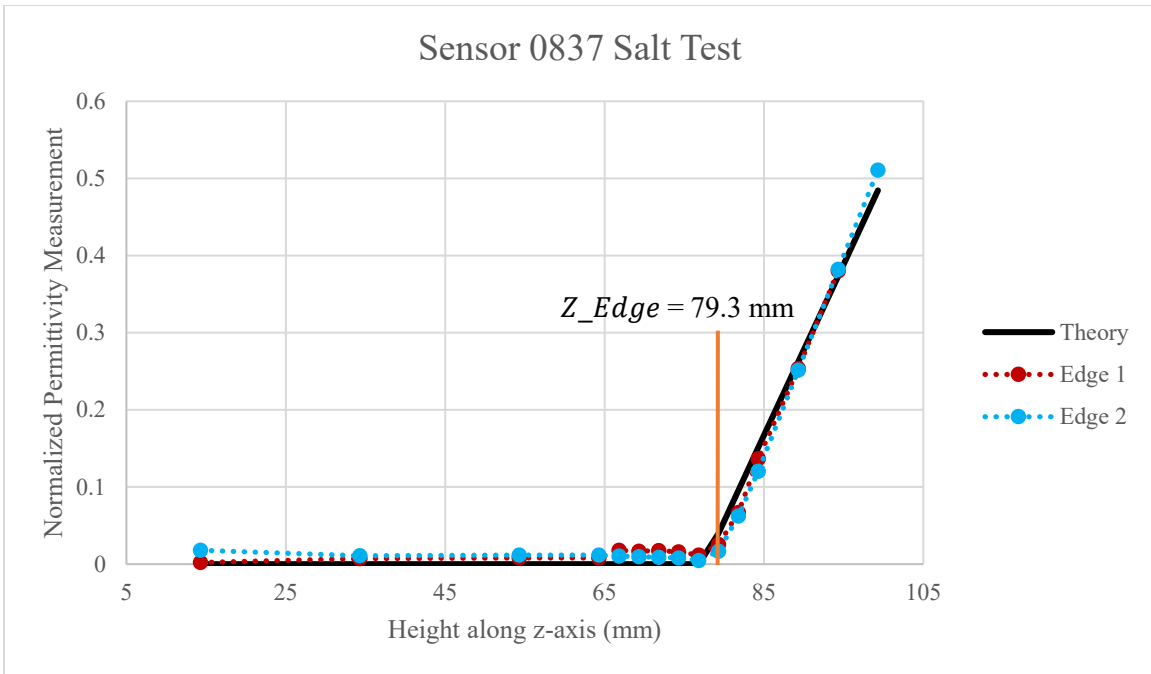
Figure 3.1a: Salt test measurement results using LBP for sensor number 0837 with 10.5 mm inner diameter.
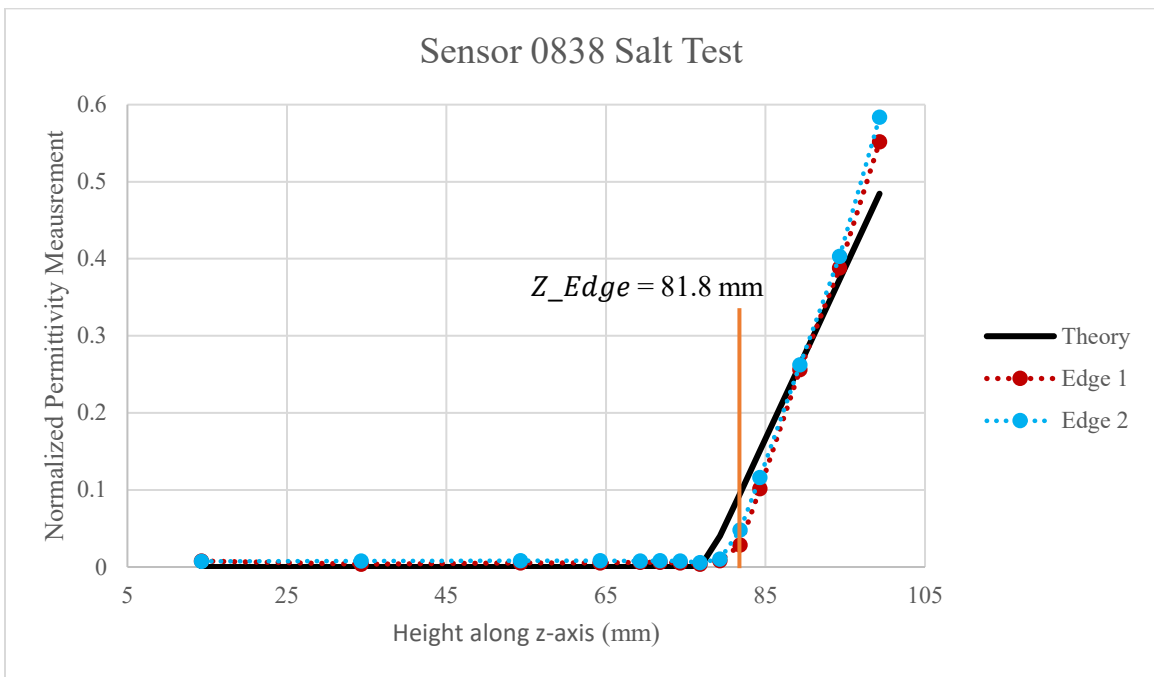
Figure 3.1b: Salt test measurement results using LBP for sensor number 0838 with 10.5 mm inner diameter.
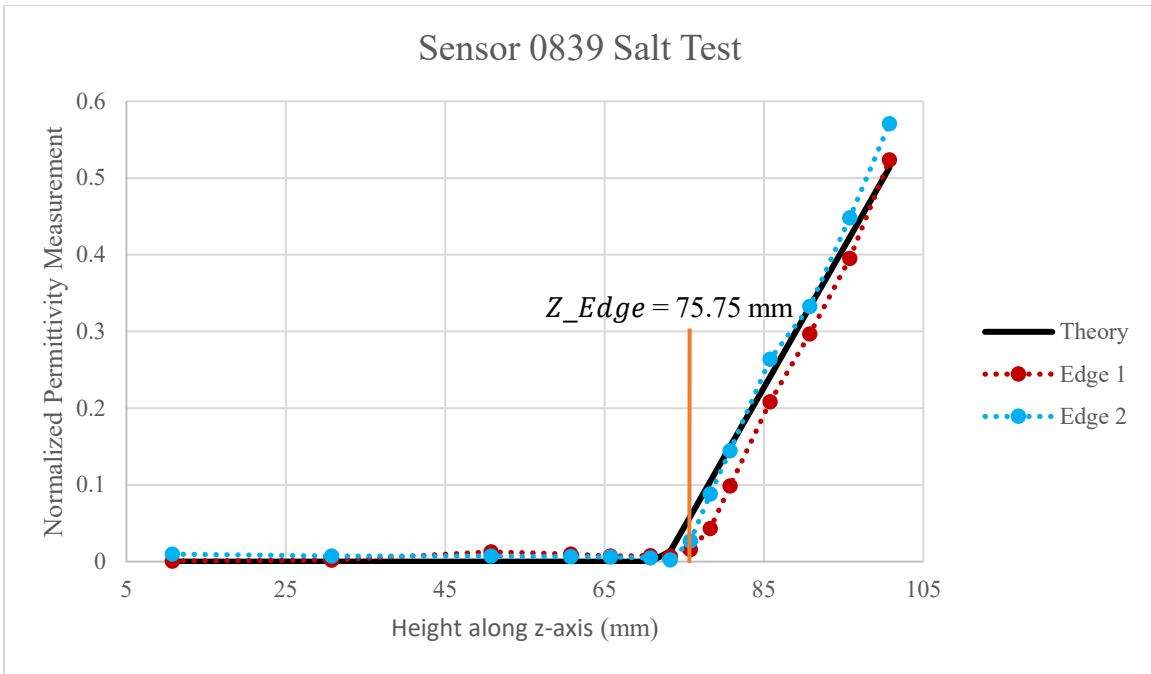
Figure 3.1c: Salt test measurement results using LBP for sensor number 0839 with 7 mm inner diameter.
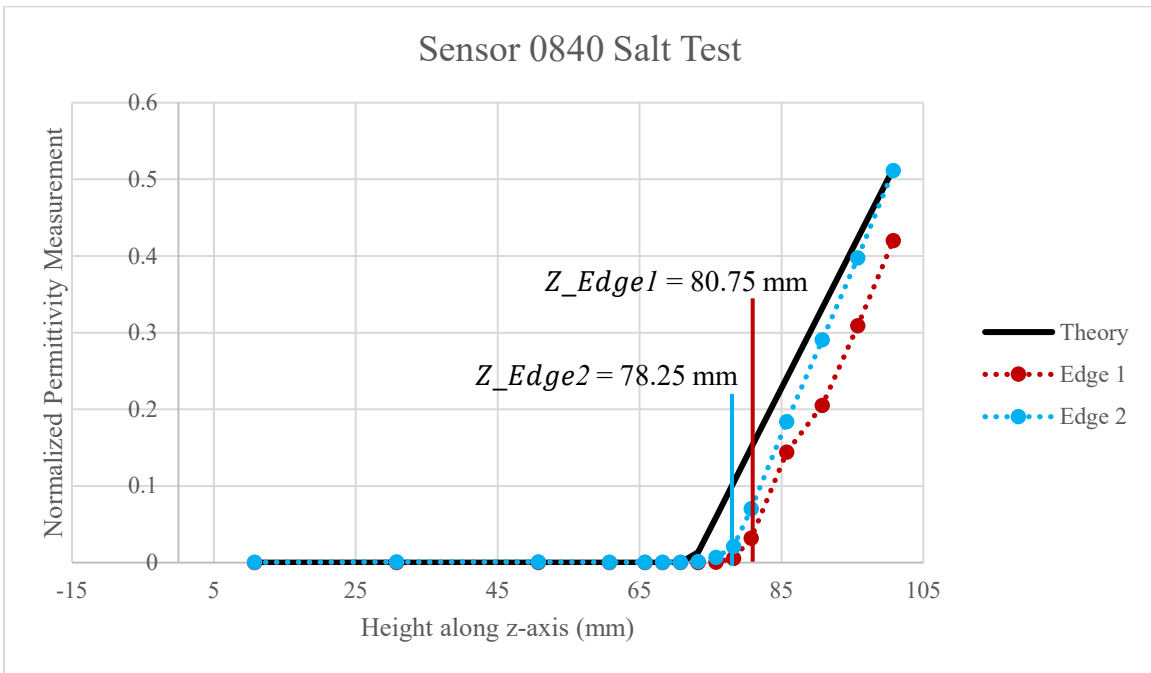
Figure 3.1d: Salt test measurement results using LBP for sensor number 0840 with 7 mm inner diameter.

The results shown in Figure 3.1 depict a different location inside the sensor than was expected where there was a detected change in permittivity. This was true for all four sensors on both edges of the electrodes using both tomographic reconstruction techniques. In each of the sensors, both edges detected a change in permittivity further into the sensor than expected. This

could possibly be the result of the electrodes being shorter than was specified in the dimensional drawings or perhaps something written into the reconstruction algorithms to ignore smaller tomography values as a way to filter fringing effects. This information will be useful in future research where sudden expansions can occur inside of the ECT sensor at the location where the electrodes detect a change in permittivity.

Another experiment that was conducted in order to better understand the measurement capabilities of the ECT sensors was using angled surfaces of salt and wood. These angled surface experiments were conducted using a single 7 mm ID sensor. The first experiments were comprised of using the wooden rod to mold the salt into a surface of a known angle. Measurements were taken using the long edge and short edge of the rod to note the orientation of the salt surface. With the long edge along the top of the tomogram, it was expected to show a higher average permittivity value in the top half compared with the bottom. The tomograms of the salt angled surface using LBP reconstruction are shown in Figure 3.2a-d and the results are displayed in Table 3.1. The tomograms for each of these four configurations were also reconstructed using HDR and can be found in Appendix A.

a) 30° Orientation 1, with long edge on top.

c) 45° Orientation 1, with long edge on top.

b) 30° Orientation 2, with long edge on bottom.

d) 45° Orientation 2, with long edge on bottom.
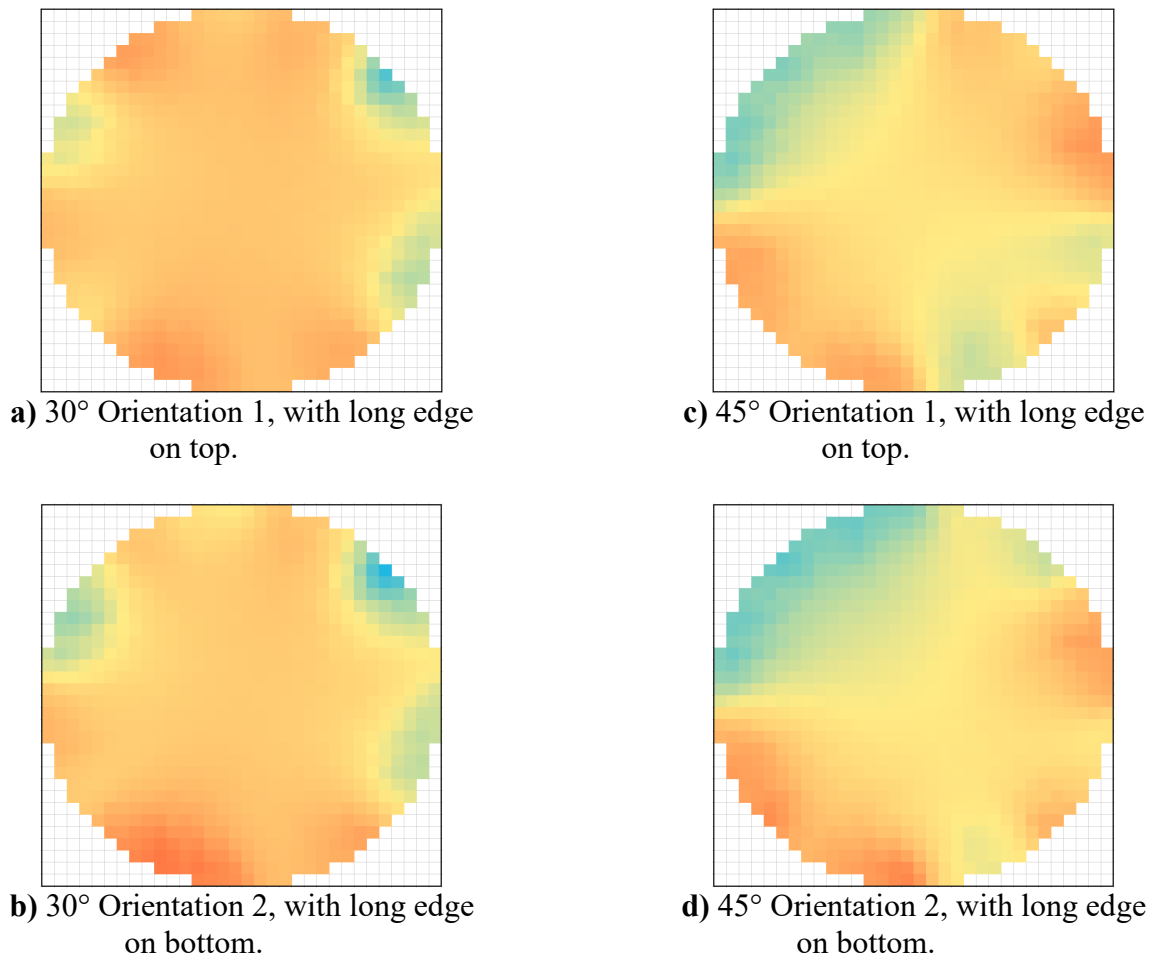
Figure 3.2: Angled salt surface tomograms
a) 30° Orientation 1, b) 30° Orientation 2, c) 45° Orientation 1, and d) 45° Orientation 2.

Table 3.1: Normalized permittivity ECT output with angled salt surface.

Material	Angle	Orientation	Permittivity Value		Upper Half Δ%	Lower Half Δ%
			Upper Half	Lower Half		
Salt	30°	1	0.549	0.512	-2.00	1.95
	30°	2	0.538	0.522		
	45°	1	0.527	0.560	6.26	-6.61
	45°	2	0.560	0.523		

Figure 3.2 shows that there is minimal difference in the top and bottom halves of the tomograms between the different angles at each orientation. When comparing the values from Table 3.1, the results were not as expected. The Upper Half Δ% was calculated as the change in percentage of the values from Orientation 1 to Orientation 2 in the upper half of the tomographic image. The expected results would have higher readings for the upper half in orientation 1 when the long edge faces upwards inside the sensor, and lower readings in orientation 2 when the long edge faces downwards. In theory, when changing the angle between orientation 1 and orientation 2, the upper half should decrease in the ECT output value and the lower half should increase for both angles. The results from the test show this pattern with the 30° surface, however with the 45° surface this form was not followed. This could have been the result of the salt not properly staying in place when the wooden rod was removed or the salt not fully forming to the surface of the angled wooden rod. As a result, to eliminate these potential errors, the experiment was run using just the angled rod inside of the ECT sensor. The tomograms for the experiments involving only the wooden rod that were reconstructed using LBP are shown in Figure 3.3a-d. The numerical values are shown in Table 3.2. The tomograms for these experiments were also reconstructed using HDR and can be found in Appendix A.

a) 30° Orientation 1, with long edge on top.

c) 45° Orientation 1, with long edge on top.

b) 30° Orientation 2, with long edge on bottom.

d) 45° Orientation 2, with long edge on bottom.
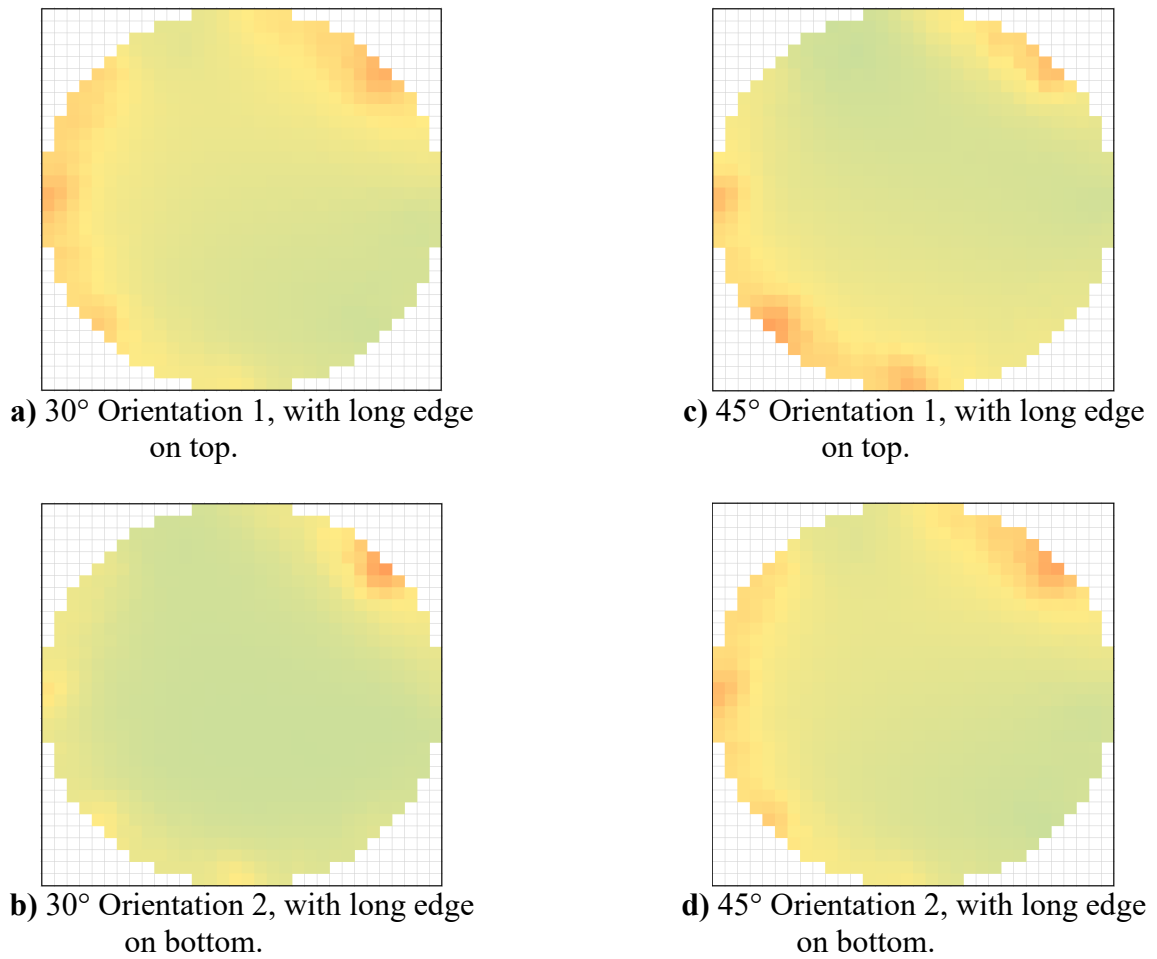
Figure 3.3: Angled wooden rod tomograms

a) 30° Orientation 1, b) 30° Orientation 2, c) 45° Orientation 1, and d) 45° Orientation 2.

Table 3.2: Normalized permittivity ECT output with angled wooden rod.

Material	Angle	Orientation	Permittivity Value		Upper Half Δ%	Lower Half Δ%
			Upper Half	Lower Half		
Wood	30°	1	0.425	0.448	-6.35	3.57
	30°	2	0.398	0.464		
	45°	1	0.406	0.441	-11.33	6.58
	45°	2	0.36	0.47		

Table 3.3: Theoretical permittivity values for angled surfaces of 30 and 45

φ	Upper Volume (mm³)	Lower Volume (mm³)	Total Volume (mm³)	ε, upper	ε, lower	Δ% ε
30°	449.45	416.45	1058.32	0.424	0.393	3.12
45°	461.53	404.37	1058.32	0.436	0.382	5.40

Δ% ε shows the expected change in permittivity when rotating the rod from orientation 1 to orientation 2

In contrast to Table 3.1, Table 3.2 shows that with the wooden rod and a better defined surface, the ECT detects a change when rotating from orientation 1 to orientation 2. The values in Table 3.2 can be compared with the theoretical values of Table 3.3 as described in Chapter 2. When comparing with a theoretical value, the permittivity change determined from the experiments is larger than the theoretical values. This could be due to noise in the ECT readings as changes in the permittivity value are relatively small when rotating from orientation 1 to orientation 2. As a consequence, it is believed that additional experiments need to be conducted in the future with steeper ϕ to verify that the sensors can detect more complex surfaces. These values of ϕ would provide greater changes in permittivity inside the ECT sensor and reduce the uncertainty in the sensor's capability to detect the surface. The ability of the ECT system to accurately represent a feature such as an angled surface could ultimately be useful, for example, in identifying a single wave inside a flow channel.

3.2 TEMA Expansion Velocity Analysis Results

In addition to exploring the measurement capabilities of the ECT sensor, another objective of this thesis was to use flow visualization to study a horizontal sudden expansion involving liquid-vapor R-134a and a high speed camera with TEMA motion analysis software. The use of the high speed camera and motion analysis software allows for the tracking of individual points in the flow to determine velocities. In this work, the mass flux (G) was kept constant at $262 \frac{kg}{m^2 s}$ in the 7 mm ID tube and heater power was adjusted to control the vapor quality (x) in the range 0.002 to 0.489. Screen captures from the high speed videos that are representative of the flow for the sudden expansion and fully developed flow channels at the mass flux of $262 \frac{kg}{m^2 s}$ are shown in Figures 3.4a-k. From these high speed videos, features were chosen that were representative of the bulk liquid flow in the channel. These features were tracked using TEMA software and their velocities were recorded. The results from this analysis are shown in Figure 3.5.

Figure 3.4 shows flow patterns for different qualities at the expansion and at 40 diameters downstream from the expansion. The flow regimes were identified from flow regime data from a previous investigation with two-phase liquid-vapor flow using R-134a (Roman et al., 2016). The low qualities of 0.002 and 0.011 show little change in flow regime as the flow travels from the smaller diameter through the expansion to the larger diameter. This trait is shown in Figure 3.4a which shows bubbly flow in the smaller diameter before the sudden expansion as well as the fully developed section 40 diameters downstream from the expansion. As the quality increases however, the flow regime changes at different rates in the 7 mm ID tubing relative to the 10.5 mm ID tubing. This observation is particularly striking when compared to Figures 2.4f-k. As the quality increased from 0.206 to 0.489, the flow regime in the 7 mm ID tube transformed from a stratified wavy pattern with chaotic behavior in the expansion into an annular flow regime with a full film around the entire tube. In this same quality range, the 10.5 mm ID tube went from a stratified wavy flow regime to a stratified wavy-transitional flow with the only notable change in flow pattern being smaller amplitude and more frequent waves with a rough surface. This behavior shows that at higher quality levels, the large diameter tube downstream from the expansion is less effected by a change in quality than the small diameter tubing upstream from the expansion.
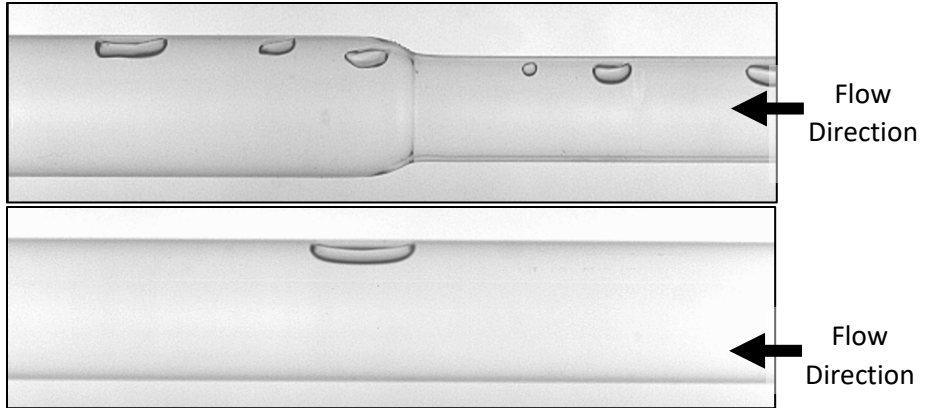
Figure 3.4a: x = 0.002, bubbly flow regime upstream of the expansion in the 7 mm ID tubing as well as in the downstream 10.5 mm ID section.
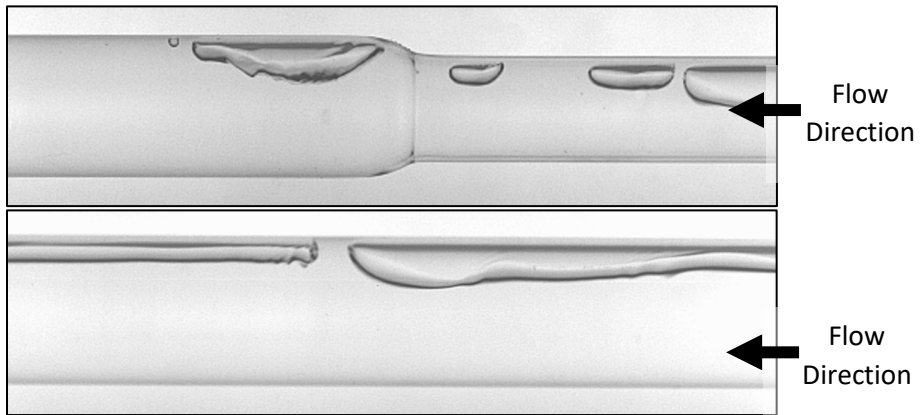
Figure 3.4b: x = 0.011, bubbly flow regime upstream of the expansion in the 7 mm ID tubing
Bubbly-transitional flow pattern evident by the elongated bubbles in the 10.5 mm ID tubing.
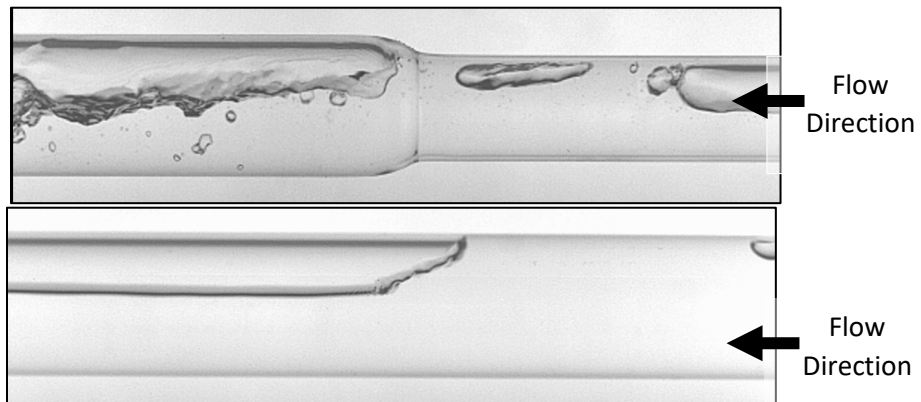
Figure 3.4c: x = 0.055, bubbly-transitional flow regime upstream of the expansion in the 7 mm ID tubing
Plug flow pattern in the 10.5 mm ID tubing.
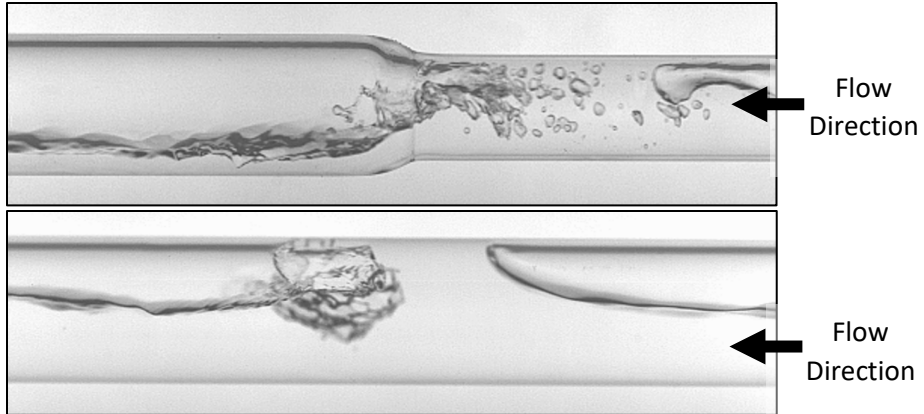
Figure 3.4d: x = 0.094, slug flow regime upstream of the expansion in the 7 mm ID tubing
Slug flow pattern in the 10.5 mm ID tubing. When the slug flow has a wave collide inside a slug of vapor, the small vapor bubbles become dispersed throughout the liquid.
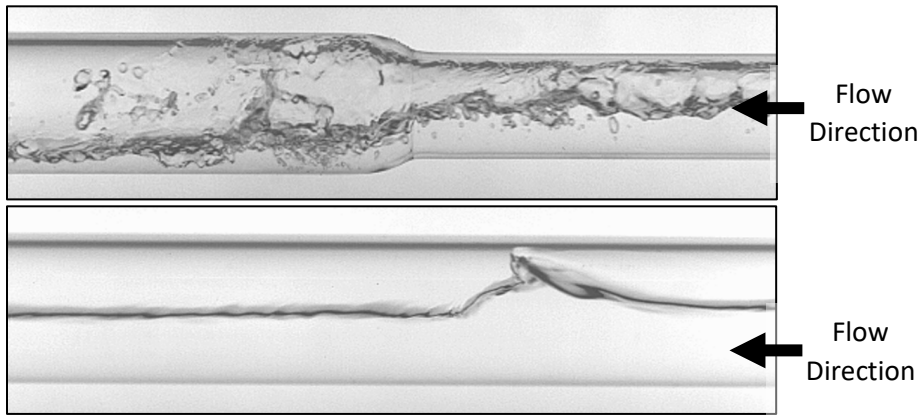
Figure 3.4e: x = 0.149, stratified wavy flow regime upstream of the expansion in the 7 mm ID tubing
Slug-transitional flow pattern in the 10.5 mm ID tubing. In the 7 mm ID tubing, the stratified wavy flow becomes chaotic traveling through the expansion, but diminishes to slug-transitional when fully developed.
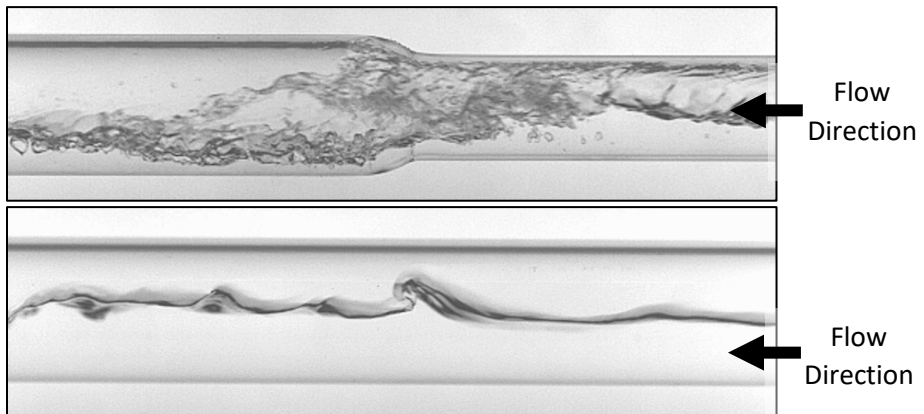
Figure 3.4f: x = 0.206, stratified wavy-transition flow regime evident by colliding waves cause slight film on top inner surface of the 7 mm ID tubing
Chaotic mixture of liquid and vapor in the expansion. Stratified wavy flow pattern in the 10.5 mm ID tubing.
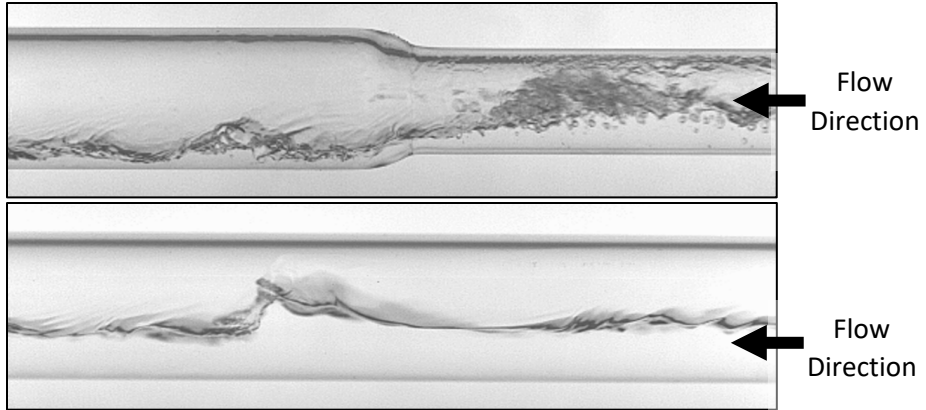
Figure 3.4g: x = 0.263, stratified wavy-transitional regime upstream of the expansion in the 7 mm ID tubing showing more liquid film on top of the tube compared with observations at lower qualities

10.5 mm ID tubing shows stratified wavy with large single waves forming.
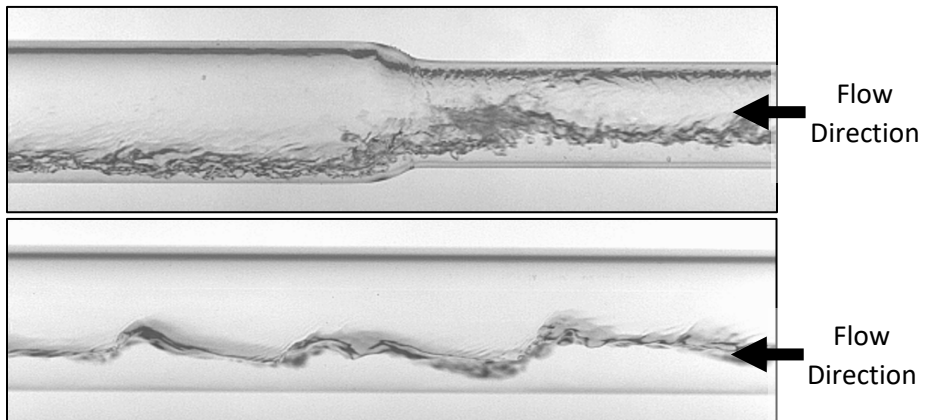
Figure 3.4h: x = 0.320, stratified wavy-transitional regime upstream from the expansion in the 7 mm ID tubing

This flow produces a liquid film on the top surface of the tube that is still caused by waves. Stratified wavy in the 10.5 mm ID tubing with rough surface of liquid.
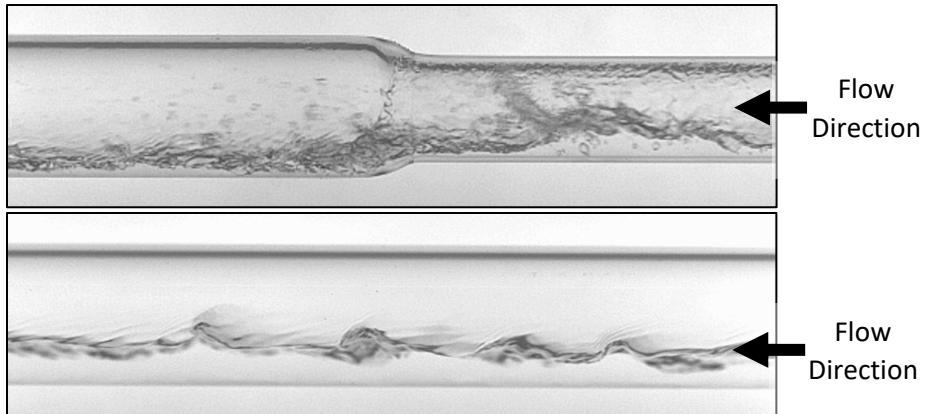
Figure 3.4i: x = 0.375, stratified wavy-transitional flow pattern upstream of the expansion in the 7 mm ID tubing
. This flow pattern has waves traveling on the lower part of the tube as well as a relatively thick liquid flow on the bottom of the tube compared with flows of higher quality. Stratified wavy flow pattern in the 10.5 mm ID tubing.
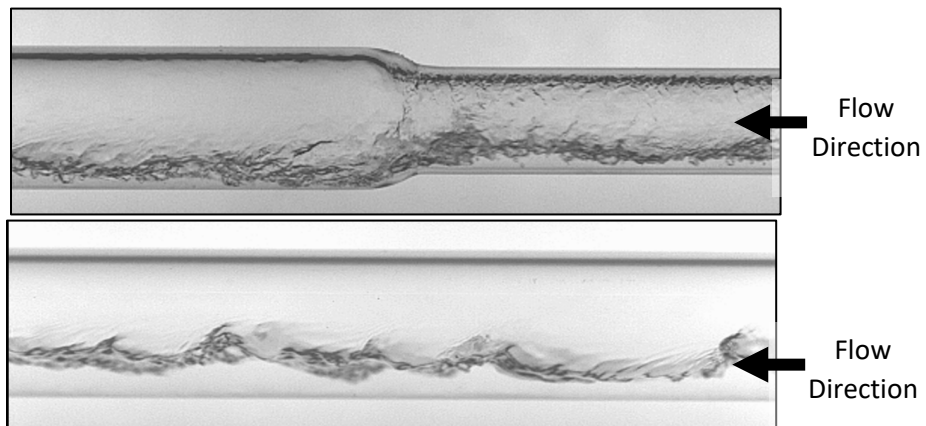
Figure 3.4j: x = 0.433, annular flow regime upstream of the expansion in the 7 mm ID tubing evident by only a liquid film on top of tube and no waves in lower portion of tube
Stratified wavy-transitional flow pattern in the 10.5 mm ID tubing demonstrated by the frequency and amplitude of waves as well as the roughness of the surface of liquid.
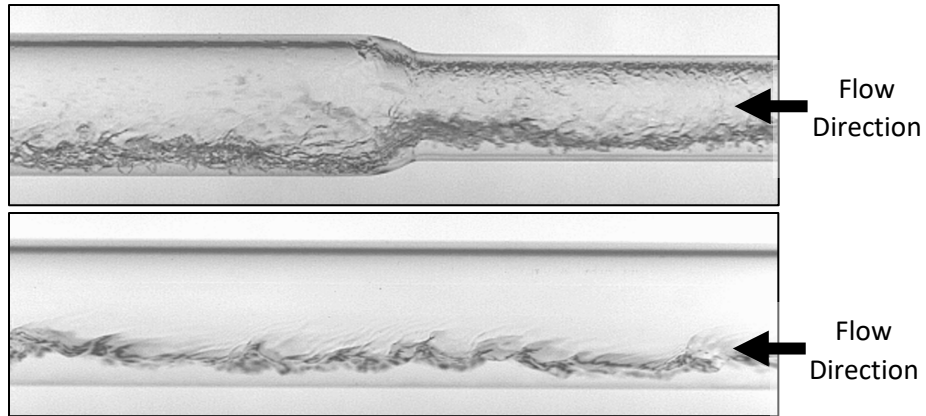
Figure 3.4k: x = 0.489, annular flow regime upstream of the expansion in the 7 mm ID tubing
evident by the film along the top of tube
Stratified wavy-transitional flow pattern in the 10.5 mm ID tubing.

Figure 3.5 shows the measured velocities for 71 features tracked in the high speed videos at varying qualities in the experiment. The features tracked in each of the high speed videos were chosen as representative of the two-phase flow. As a result, they are selected on the liquid-vapor interface, since this is where the velocity of the liquid is equal to the velocity of the vapor. Consequently, qualities with chaotic behavior between the liquid and vapor interface such as those shown in Figures 3.4e-g have a higher range in measured velocities as shown in Figure 3.5. With such chaotic events, tracked points could include small droplets of liquid R-134a being accelerated by the flow of the vapor, or small bubbles of vapor being impeded by the liquid flow and thus, may not individually be representative of the bulk two-phase flow. This chaotic behavior was more pronounced in the 7 mm ID tubing than the 10.5 mm ID tubing, as evident in qualitative observations from the high speed video (Figures 3.4e-g) and visible in the plot of Figure 3.5. To further examine this chaotic behavior, the Reynolds number was calculated for both the vapor and liquid phases in both small and large tubes. The Reynolds numbers were calculated using equations from Carey (1992) and are given here as Equations 3.1 and 3.2. As shown in the plot of Figure 3.6, a source of the turbulence comes from the high Reynolds numbers found in the vapor phases of both the 7 mm and 10.5 mm tubing. The liquid phase of both diameters was also found to be turbulent, although their respective Reynolds numbers decreased as the quality increased. Future work could involve investigating how this decrease in Reynolds number effects the flow pattern of the liquid phase. As shown in the plot of Figure 3.6, the Reynolds number of the 7 mm tube is larger than the Reynolds number of the 10.5 mm tube in both the liquid and vapor phases throughout the entire measured quality range. Since the 7 mm ID tube has a higher Reynolds number in both phases, this may explain why the chaotic behavior occurs more often in this section rather than in the large tube. Once the chaotic behavior causes large-scale mixing of the two phases, difficulties arise for velocity measurements.
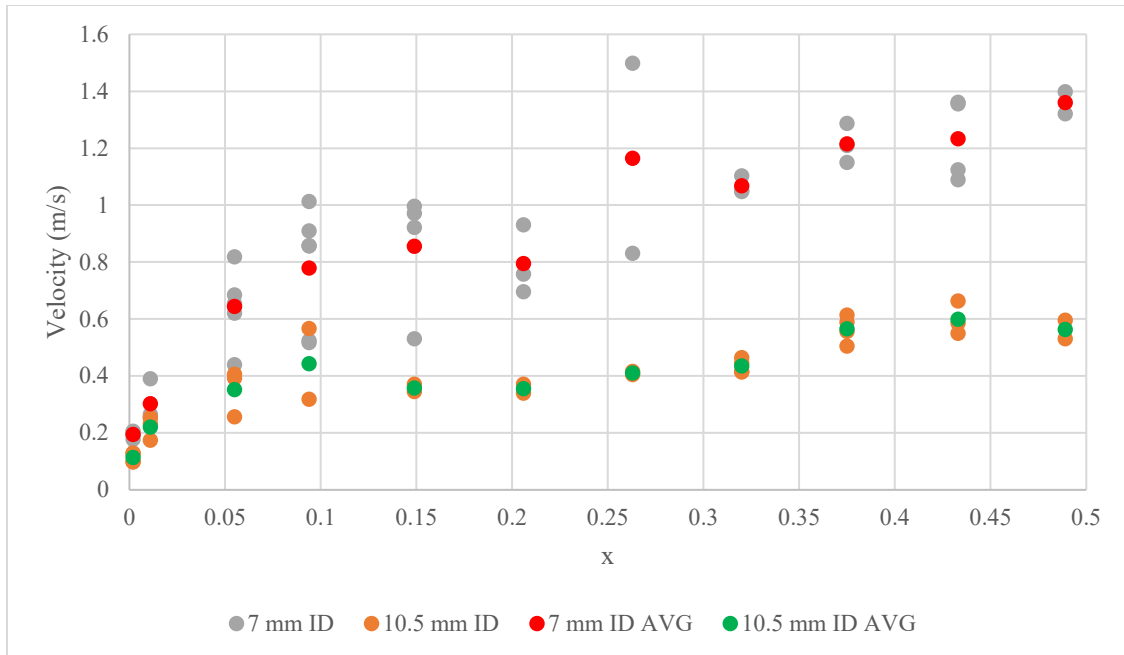
Figure 3.5: Measured liquid-vapor interface velocities for features in 7 mm and 10.5 mm ID tubing with horizontal sudden expansion of two-phase liquid-vapor flow. $G = 262 \frac{kg}{m^2 s}$.

$$Re_v = \frac{2r_0 G x}{\mu_v} \tag{3.1}$$

$$Re_l = \frac{2r_0 G(1-x)}{\mu_l} \tag{3.2}$$
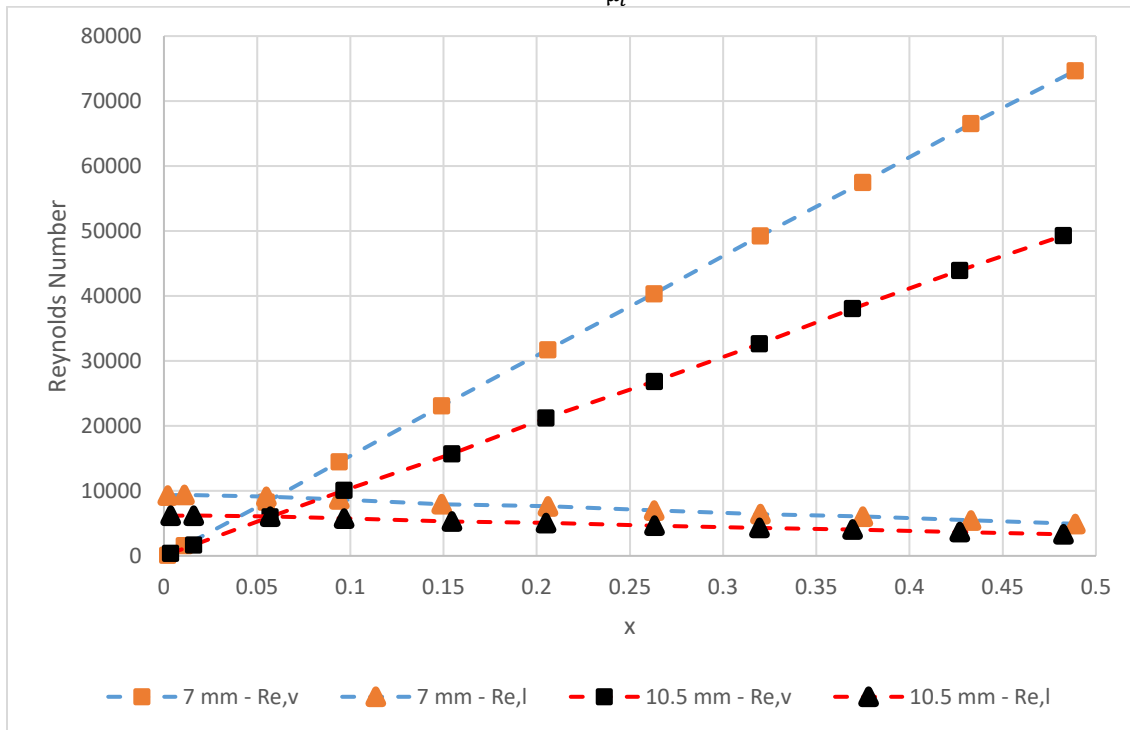
Figure 3.6: Calculated Reynolds number for vapor and liquid phases in 7 mm and 10.5 mm ID tubes.

One cause for the observed chaotic interface in the stratified wavy-transitional phase is the pressure drop that occurs when the flow travels through the sudden expansion. To measure the pressure drop caused by the sudden expansion, two Omega model PX409-150GV-XL pressure transducers were placed 200 mm upstream and 200 mm downstream from the sudden expansion. These transducers measured experimental values of the pressure. Their differences in readings were compared with the three two-phase pressure drop correlations shown in Figure 3.7 which are given by Equations 3.3, 3.4 and 3.5 (Chen et al., 2007). The first correlation (Equation 3.3) is the Collier and Thome correlation for homogeneous flow through a sudden expansion. This correlation ignores wall shear and gravitational forces and assumes the void fraction remains unchanged across the expansion (Collier and Thome, 1994).Collier and Thome admit the assumption of a constant void fraction is approximately true as there are large changes in void fraction across the expansion that do not return to the initial value until further downstream. This correlation has a relatively good fit at qualities below 0.375. At higher qualities, the correlation provided a poorer fit, as perhaps there was a larger change in void fraction where the pressure was measured, approximately 19 diameters from the expansion. The next correlation (Equation 3.4) considered assumed a heterogeneous flow and a loss of pressure in the liquid phase (Lottes, 1961).The experimental data seems to fit well with the correlation and seemed to match the exponential curve of the experimental data at higher qualities. However, even though the correlation matched the shape of the curve, it over predicts the pressure drop at higher qualities. The last correlation (Equation 3.5), the homogeneous Romie model, appears to predict pressure drop similar to Collier and Thome's (Lottes, 1961). However, the Romie model does not take into account the dissipation of heat (Collier and Thome, 1994). Similar to Collier and Thome (1994), the Romie model predicts relatively accurate pressure drop values for qualities below 0.375. However, it under predicts pressure drop for qualities above 0.375. When comparing measured pressure drop data with these three correlations, the Collier and Thome (1994) and Romie models (Lottes, 1961) were able to accurately predict the pressure drop for qualities below 0.375. For higher qualities, the Lottes model (Lottes, 1961) was able to predict the shape of the curve for the pressure drop, however it over predicted the measured values. Tabular data from the experimental pressure drops as well as the calculated pressure drops from the correlations can be found in Appendix A.

$$\Delta P = \frac{-G^2(1-\sigma_A^2)}{2\left(\frac{x}{\rho_v}+\frac{(1-x)}{\rho_l}\right)}\left[\frac{(1-x)^3}{(1-\alpha)^2\rho_l^2} + \frac{x^3}{\alpha^2\rho_v^2}\right] \tag{3.3}$$

$$\Delta P = \frac{-G^2\sigma_A(1-\sigma_A)}{\rho_l(1-\alpha)^2} \tag{3.4}$$

$$\Delta P = -G\sigma_A(1-\sigma_A)\left[\frac{(1-x)}{\rho_l} + \frac{x}{\rho_v}\right] \tag{3.5}$$
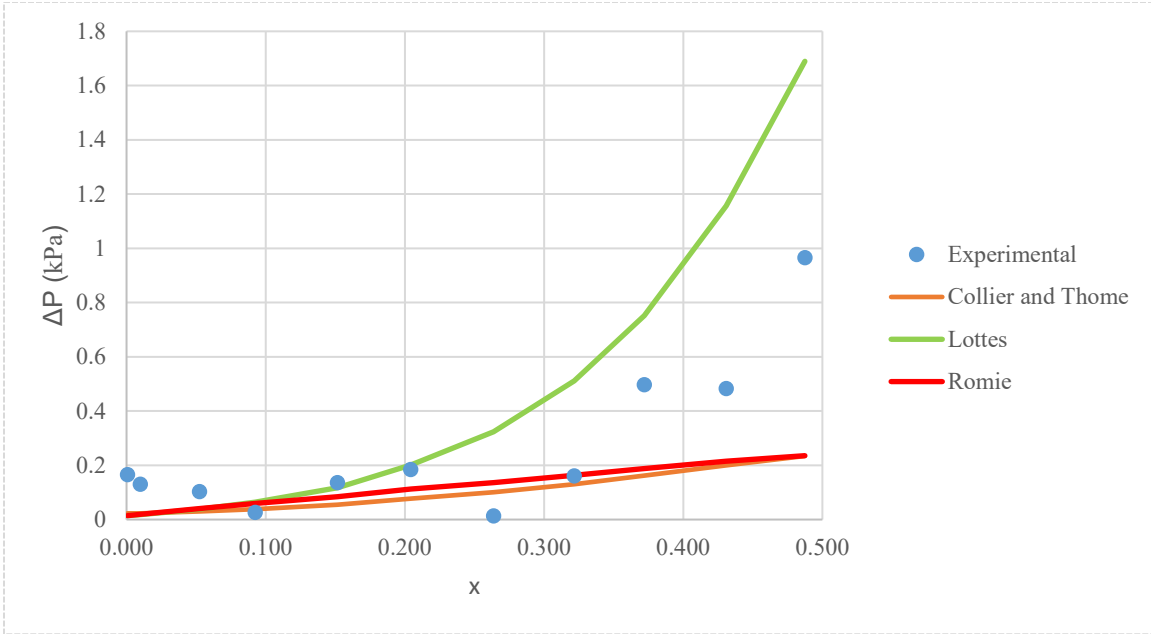
Figure 3.7: Measured pressure differences for two-phase flow through sudden expansion compared with Collier and Thome (1994), and Lottes (Lottes, 1961), and Romie's homogeneous (Lottes, 1961) correlations.

CHAPTER 4
CONCLUSIONS AND FUTURE WORK

4.1 Summary

The measurement capabilities of the electrical capacitance tomography (ECT) sensor were explored with experiments using salt and angled wooden rods. For the salt test, known levels of salt were added to an empty sensor to determine the location in the sensor, Z_{Edge}, that the sensor's electrodes were able to detect a change in permittivity. Four different sensors of two different inner diameters were tested to create a baseline of dimensions that could be used for future work. Another experiment testing the measurement capabilities of the ECT sensor were the angled surface investigations. These experiments sought to determine the sensor's capability of detecting different surface features. The final objective of this thesis was to visualize horizontal two-phase R-134a flow with a high speed camera and perform a velocity analysis on the different flow patterns observed. Mass flux rates of $262 \frac{kg}{m^2 s}$ were used and experiments varying the quality of the flow were performed to bring about a variety of flow regimes for analysis. Lastly, the pressures were measured on either side of the sudden expansion to compare with other two-phase correlations.

4.2 Conclusions and Future Work

The salt experiments performed for this thesis showed that in each of the sensors, the electrodes were not detecting a change in permittivity at their physical location according to the dimensional drawings. The experiments determined the location along the length of the sensor where a change in permittivity was detected at an electrode edge for each of the four sensors. This information will be useful for future work such as having a sudden expansion occur at an electrode edge to study the involved changes in permittivity.

The angled surface experiments demonstrated the ECT system's ability to detect a surface. These experiments showed that with a well-defined surface, the ECT was able to detect a change when the sample was rotated to different orientations. Future work should involve more drastic changes in the surface along the measured volume. This may be ultimately useful for tracking waves or other two-phase flow features inside a flow channel.

The velocity analysis was able to demonstrate how the velocities changed in a two-phase refrigerant flow through a sudden expansion. This experiment also showed that the larger diameter tube was less effected by a change in quality than the tube of smaller diameter. As a result, the velocities in the small tube increased at a higher rate than those in the large tube. At certain qualities, chaotic behavior involving both the liquid and vapor phases made it difficult to measure the fluid velocities. An initial investigation involving the liquid and vapor Reynolds numbers suggested that the chaotic behavior could be due to turbulence in both phases. This complex phenomena should be studied in more detail in the future.

The pressure drop was recorded across the sudden expansion and compared with several two-phase pressure drop correlations. Among the correlations, the Collier and Thome (1994) and Romie models (Lottes, 1961) were able to accurately predict the pressure drop for qualities below 0.375. For higher qualities, the Lottes model (Lottes, 1961) was able to predict the shape of the curve for the pressure drop. However, it over-predicted the measured values. In conclusion, none of the correlations selected for study accurately predicted the pressure drop throughout the observed quality range. Future studies should consider additional two-phase pressure drop correlations.

BIBLIOGRAPHY

Ahmed, Wael H., Chan Y. Ching, and Mamdouh Shoukri. "Development of two-phase flow downstream of a horizontal sudden expansion." *International Journal of Heat and Fluid Flow* 29.1 (2008): 194-206.

Ahmed, Wael H., Chan Y. Ching, and Mamdouh Shoukri. "Pressure recovery of two-phase flow across sudden expansions." *International journal of multiphase flow* 33.6 (2007): 575-594.

Balakhrisna, T., et al. "Oil–water flows through sudden contraction and expansion in a horizontal pipe–Phase distribution and pressure drop." *International Journal of Multiphase Flow* 36.1 (2010): 13-24.

Barao, Teresa, et al. "Dielectric constant, dielectric virial coefficients, and dipole moments of 1, 1, 1, 2-tetrafluoroethane." *Journal of Chemical and Engineering Data* 40.6 (1995).

Canière, Hugo, et al. "Capacitance signal analysis of horizontal two-phase flow in a small diameter tube." *Experimental Thermal and Fluid Science* 32.3 (2008): 892-904.

Canière, Hugo, et al. "Mapping of horizontal refrigerant two-phase flow patterns based on clustering of capacitive sensor signals." *International Journal of Heat and Mass Transfer* 53.23 (2010): 5298-5307.

Carey, Van P. "Liquid-vapor phase-change phenomena." (1992). Eqn. 10.63 and 10.68.

Chen, Youn, et al. "Two-phase flow characteristics across sudden expansion in small rectangular channels." *Experimental Thermal and Fluid Science* 32.2 (2007): 696-706.

Chen, Youn, et al. "Two-phase flow characteristics across sudden contraction in small rectangular channels." *Experimental Thermal and Fluid Science* 32.8 (2008): 1609-1619.

Chen, Weibo, et al. *A Highly Stable Two-Phase Thermal Management System for Aircraft*. No. 2012-01-2186. SAE Technical Paper, 2012.

Clark, P. J., et al. "A comparison of methods for in situ discrimination of imaged phase boundaries using electrical capacitance tomography." *Measurement Science and Technology* 27.2 (2015): 025401.

Collier, John G., and Thome, John R. *Convective Boiling and Condensation, Third Edition*. Oxford University Press Inc., 1994. P. 108-110.

Cui, Ziqiang, et al. "An integrated ECT/ERT dual modality sensor." *Instrumentation and Measurement Technology Conference, 2009. I2MTC'09. IEEE*. IEEE, 2009.

"Dielectric Constants of Various Materials." Clipper Controls. N.p., n.d. Web. 09 Aug. 2016, http://www.clippercontrols.com/pages/Dielectric-Constant-Values.html

Dyakowski, Tomasz, Laurent FC Jeanmeure, and Artur J. Jaworski. "Applications of electrical tomography for gas–solids and liquid–solids flows—a review." *Powder technology* 112.3 (2000): 174-192.

Hu, Bin, et al. "Flow structure and phase distribution in stratified and slug flows measured by X-ray tomography." *International Journal of Multiphase Flow* 67 (2014): 162-179.

Huang, Zhiyao, Baoliang Wang, and Haiqing Li. "Application of electrical capacitance tomography to the void fraction measurement of two-phase flow." *IEEE Transactions on Instrumentation and Measurement* 52.1 (2003): 7-12.

Huang, S. M., et al. "Capacitance-based tomographic flow imaging system." *Electronics letters* 24.7 (1988): 418-419.

Hwang, Ching-Yi J., and Rajinder Pal. "Flow of two-phase oil/water mixtures through sudden expansions and contractions." *Chemical Engineering Journal* 68.2 (1997): 157-163.

Industrial Tomography Systems, Inc. *ITS Tomography Toolsuite v7.0 User's Manual*, April 2010.

Jaworski, A. J., and G. T. Bolton. "The design of an electrical capacitance tomography sensor for use with media of high dielectric permittivity." *Measurement Science and Technology* 11.6 (2000): 743.

Kendoush, Abdullah Abbas, and Zareh Azat Sarkis. "Void fraction measurement by X-ray absorption." *Experimental Thermal and Fluid Science* 25.8 (2002): 615-621.

Loser, Thomas, Radoslaw Wajman, and Dieter Mewes. "Electrical capacitance tomography: image reconstruction along electrical field lines." *Measurement Science and Technology* 12.8 (2001): 1083.

Lottes, P. A. "Expansion losses in two-phase flow." *Nuclear Science and Engineering* 9.1 (1961): 26-31.

Naini, Ali, and Mark Green. "Fringing fields in a parallel-plate capacitor." *American Journal of Physics* 45.9 (1977): 877-879.

Pakhomov, M. A., and V. I. Terekhov. "Modeling of the flow patterns and heat transfer in a turbulent bubbly polydispersed flow downstream of a sudden pipe expansion." *International Journal of Heat and Mass Transfer* 101 (2016): 1251-1262.

Roman, Abdeel J., et al. "Flow pattern identification of horizontal two-phase refrigerant flow using neural networks." *International Communications in Heat and Mass Transfer* 71 (2016): 254-264.

Thome, John R. *Wolverine Tube, Inc., Engineering Data Book III.* Wolverine Tube, Inc. 2010. Chapter 10 and Chapter 12.

Tan, Chao, Feng Dong, and Mengmeng Wu. "Identification of gas/liquid two-phase flow regime through ERT-based measurement and feature extraction." *Flow Measurement and Instrumentation* 18.5 (2007): 255-261.

Wang, Chi-Chuan, Chih-Yung Tseng, and Youn Chen. "A new correlation and the review of two-phase flow pressure change across sudden expansion in small channels." *International Journal of Heat and Mass Transfer* 53.19 (2010): 4287-4295.

Warsito, W., and L-S. Fan. "Measurement of real-time flow structures in gas–liquid and gas–liquid–solid flow systems using electrical capacitance tomography (ECT)." *Chemical Engineering Science* 56.21 (2001): 6455-6462.

Xie, C. G., A. Plaskowski, and M. S. Beck. "8-electrode capacitance system for two-component flow identification. I. Tomographic flow imaging." *IEE Proceedings A-Physical Science, Measurement and Instrumentation, Management and Education* 136.4 (1989): 173-183.

Yang, W. Q. "Hardware design of electrical capacitance tomography systems." *Measurement Science and Technology* 7.3 (1996): 225.

Yang, W. Q. "Calibration of capacitance tomography systems: a new method for setting system measurement range." *Measurement Science and Technology* 7.6 (1996): L863.

Yang, W. Q., and Lihui Peng. "Image reconstruction algorithms for electrical capacitance tomography." *Measurement science and technology* 14.1 (2002): R1.

Yang, Wuqiang. "Design of electrical capacitance tomography sensors." *Measurement Science and Technology* 21.4 (2010): 042001.

Yin, Ze-gao, et al. "Oxygen transfer characteristics of water and bubble mixture pipe flow through two sudden contractions and expansions." *Journal of Hydrodynamics, Ser. B* 26.5 (2014): 745-750.
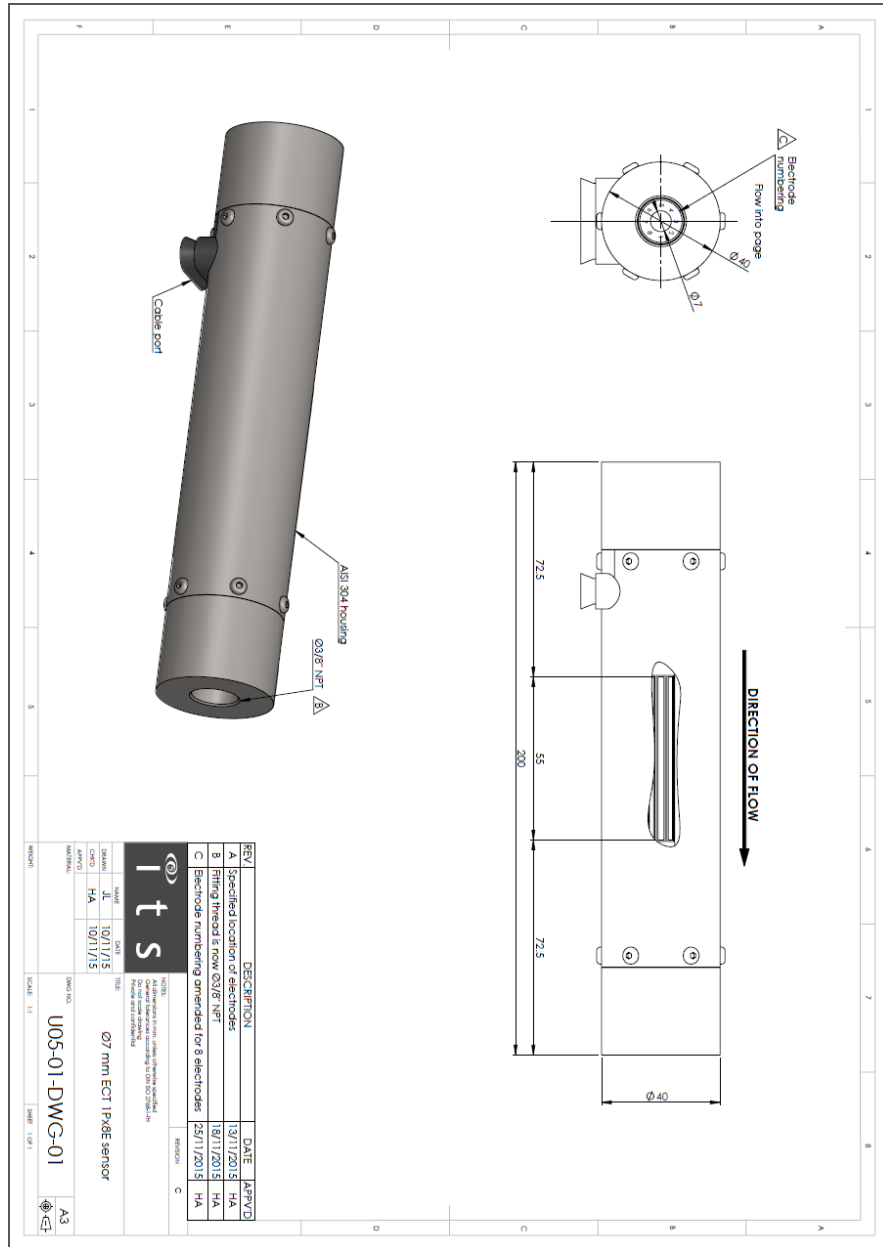
Figure A-1: Manufacturer's dimensional drawing for 7 mm ID sensor.

Figure A-2: Manufacturer's dimensional drawing for 10.5 mm ID sensor.
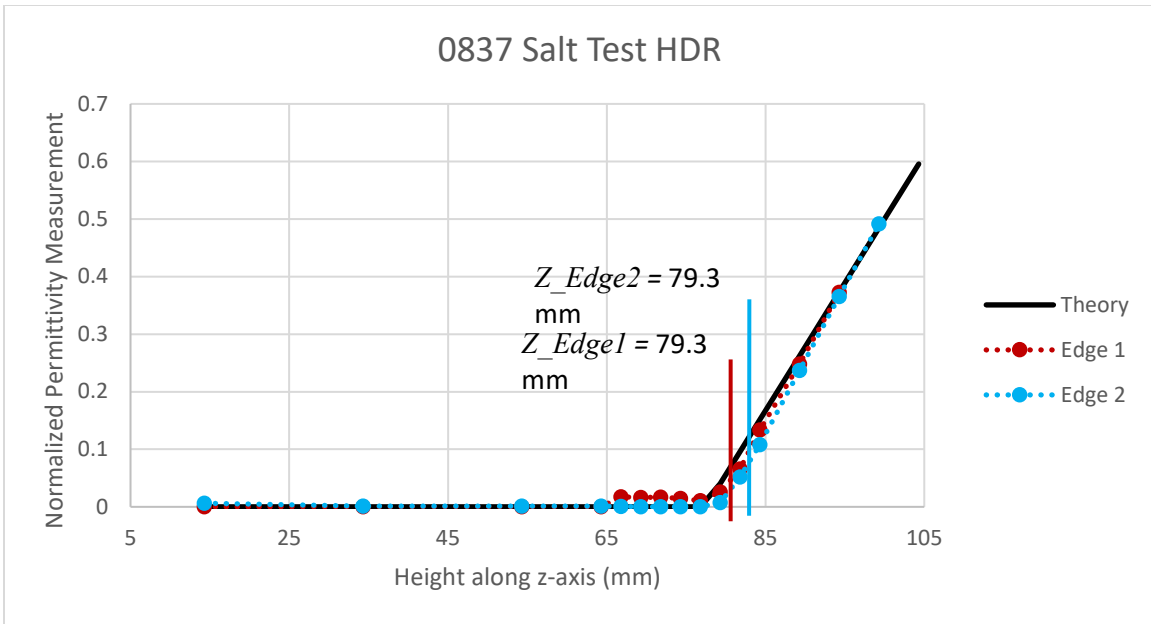
Figure A-3a: Salt test measurement results using HDR for sensor number 0837 with 10.5 mm inner diameter.
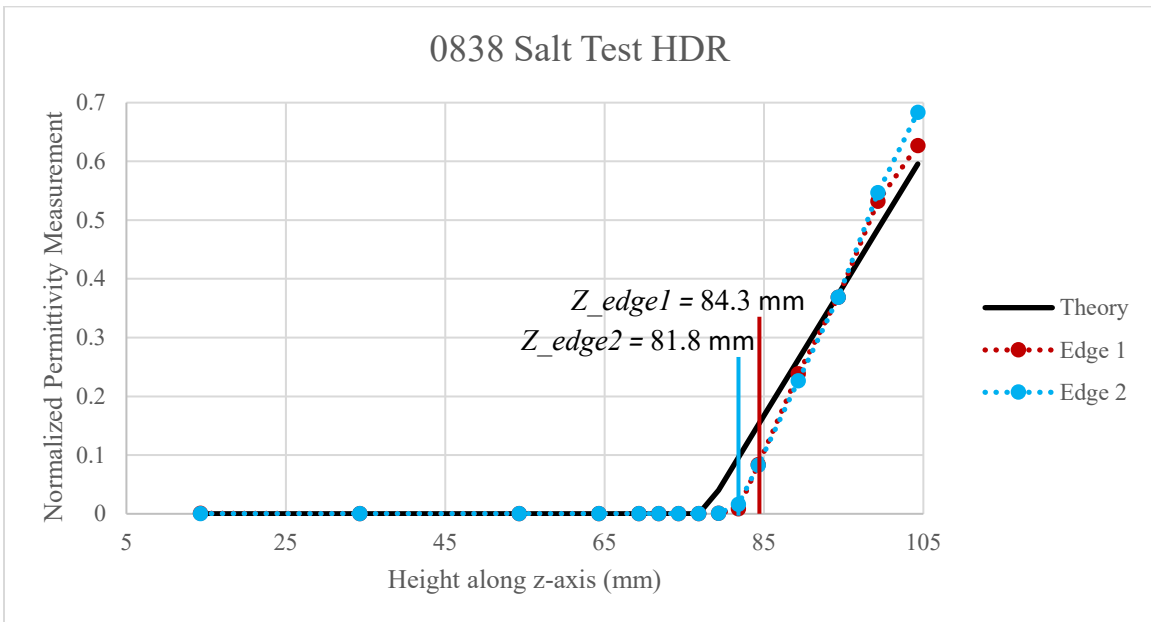
Figure A-3b: Salt test measurement results using HDR for sensor number 0838 with 10.5 mm inner diameter.
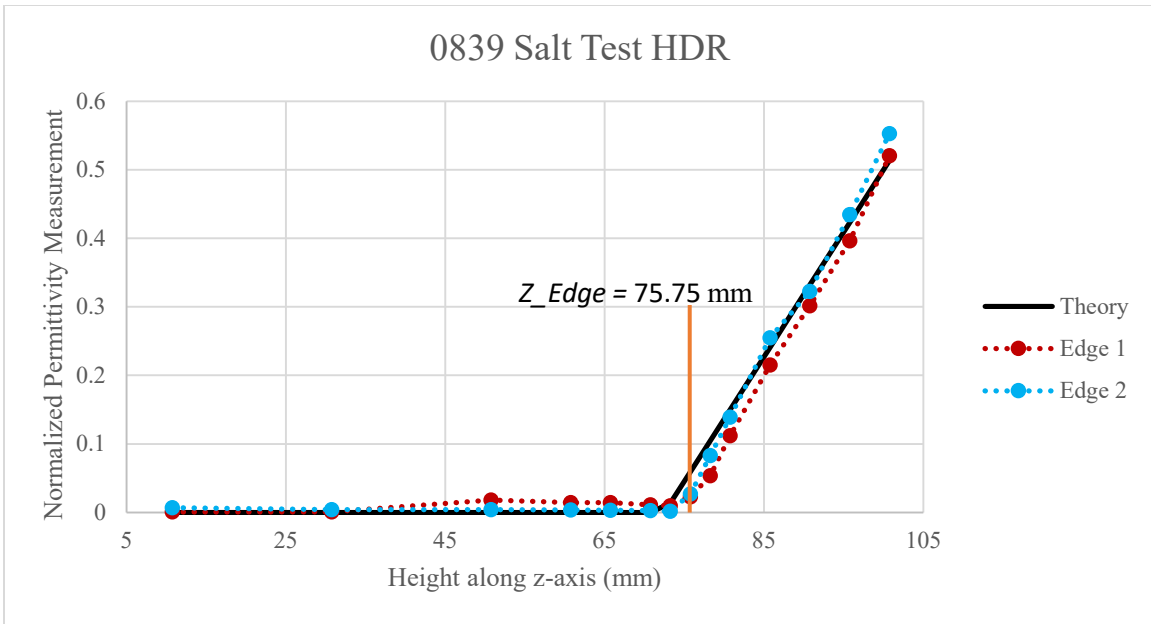
Figure A-3c: Salt test measurement results using HDR for sensor number 0839 with 7 mm inner diameter.
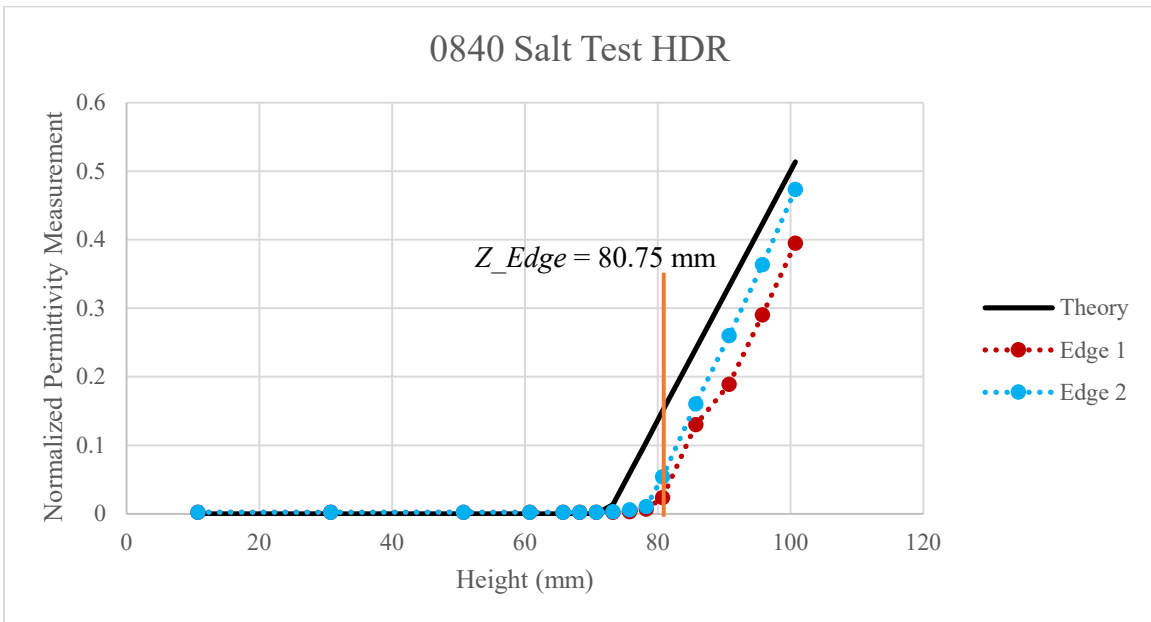
Figure A-3d: Salt test measurement results using HDR for sensor number 0840 with 7 mm inner diameter.

Table A-1: Calculated heights for measured change in permittivity found through salt experiment.

Reconstruction Technique	Sensor ID	Theoretical Edge (mm)	ID (mm)	Edge 1 (mm)	Edge 2 (mm)
LBP	837	77.5	10.5	79.3	79.3
	838	77.5	10.5	81.8	81.8
	839	72.5	7	75.75	75.75
	840	72.5	7	80.75	78.25
HDR	837	77.5	10.5	79.3	81.8
	838	77.5	10.5	84.3	81.8
	839	72.5	7	75.75	75.75
	840	72.5	7	80.75	80.75

a) 30° Orientation 1, with long edge on top.

c) 45° Orientation 1, with long edge on top.

b) 30° Orientation 2, with long edge on bottom.

d) 45° Orientation 2, with long edge on bottom.
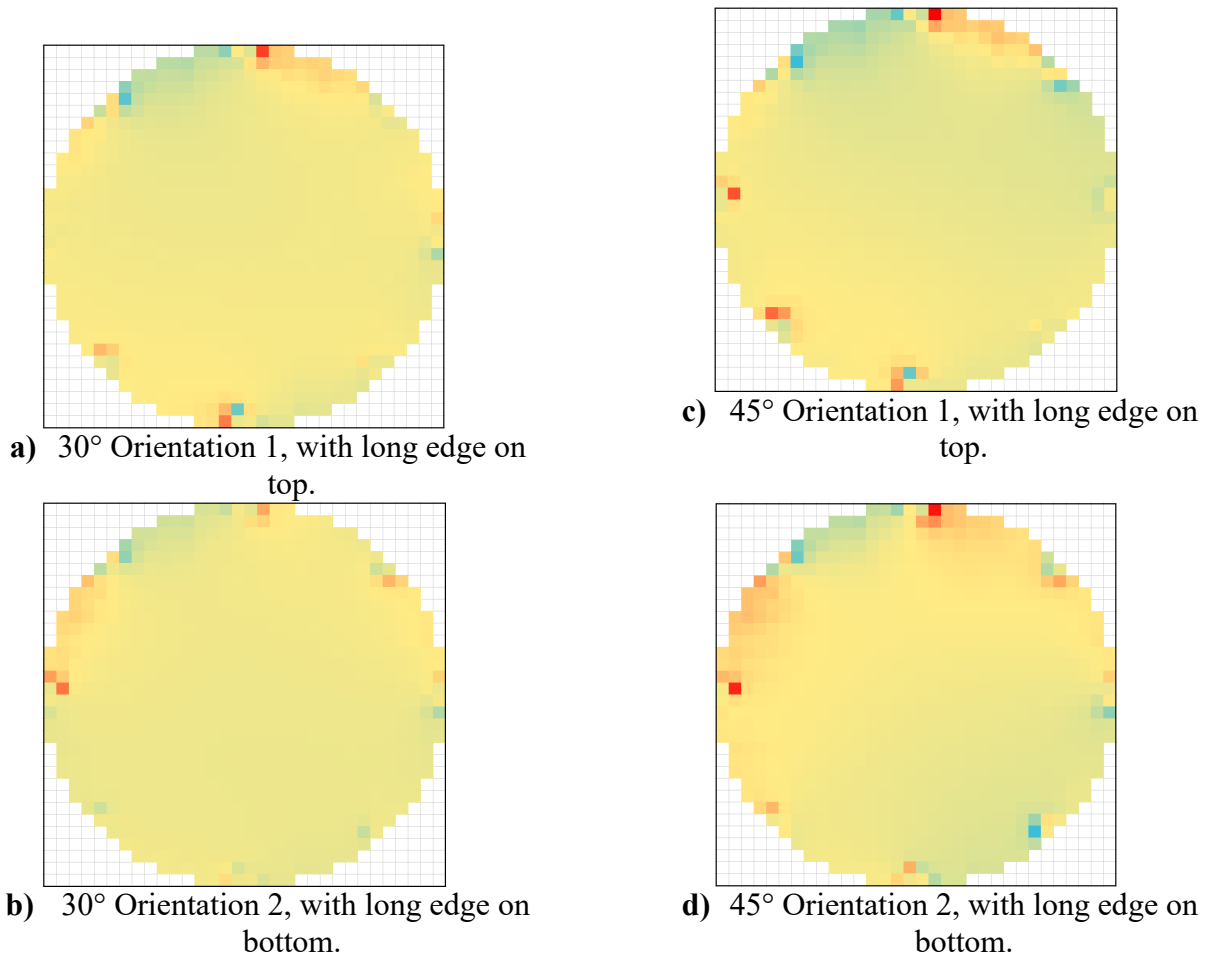
Figure A-4: Angled salt surface tomograms reconstructed in HDR
a) 30° Orientation 1, b) 30° Orientation 2, c) 45° Orientation 1, d) 45° Orientation 2.

a) 30° Orientation 1, with long edge on top.

c) 45° Orientation 1, with long edge on top.

b) 30° Orientation 2, with long edge on bottom.

d) 45° Orientation 2, with long edge on bottom.
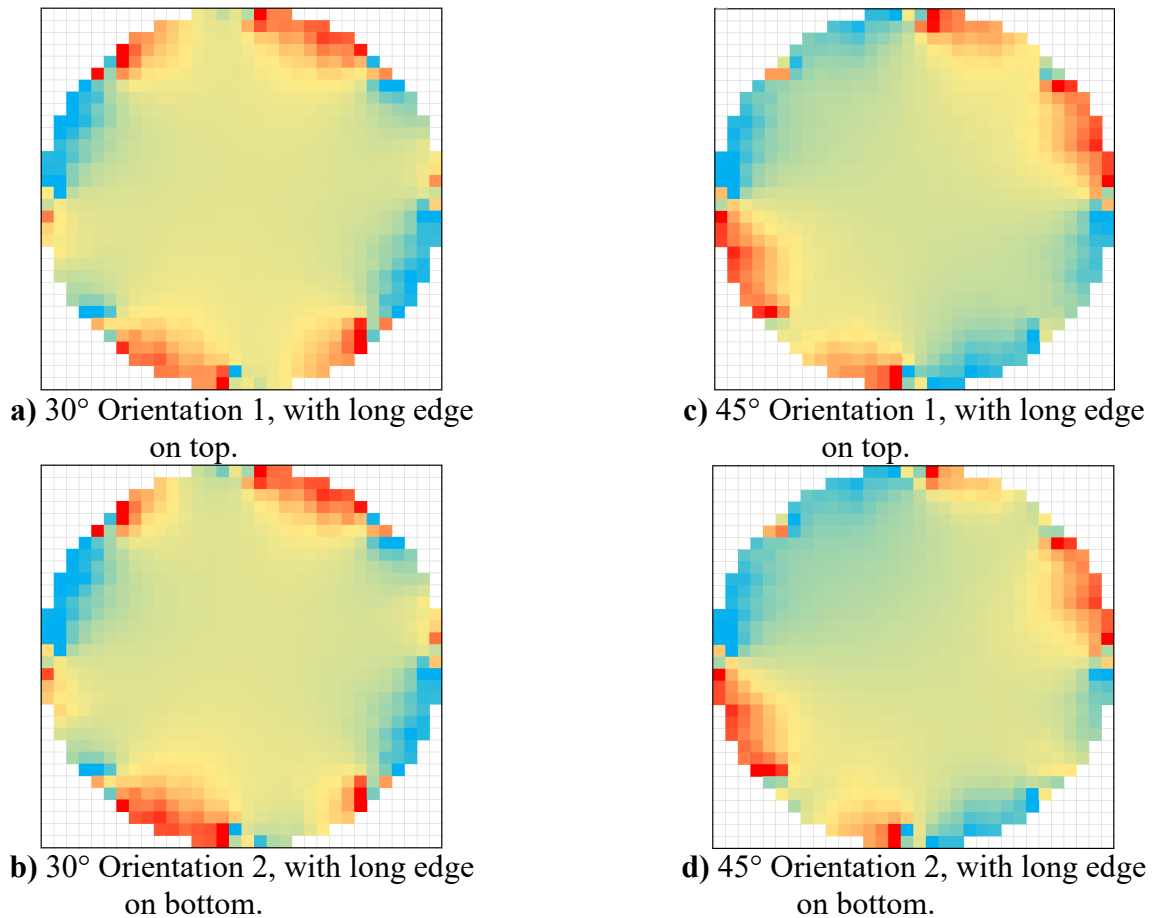
Figure A-5: Angled wooden rod tomograms reconstructed in HDR
a) 30° Orientation 1, b) 30° Orientation 2, c) 45° Orientation 1, d) 45° Orientation 2.

Table A-2: Pressure drop data when comparing experimental pressure recordings with Romie, Collier and Thome, and Lottes correlations.

x	Experimental (kPa)	Romie (kPa)	Collier and Thome (kPa)	Lottes (kPa)
0.001	0.16536	0.01451	0.02292	0.01438
0.010	0.12979	0.01951	0.02302	0.01783
0.052	0.10250	0.04102	0.02932	0.03760
0.092	0.02646	0.05972	0.03850	0.06373
0.151	0.13581	0.08384	0.05439	0.11725
0.204	0.18415	0.11210	0.07679	0.20134
0.264	0.01297	0.13574	0.10055	0.32314
0.322	0.16104	0.16290	0.13049	0.51170
0.372	0.49758	0.18801	0.16149	0.75204
0.431	0.48301	0.21543	0.19951	1.15714
0.487	0.96570	0.23549	0.23426	1.69000

APPENDIX B
TEMA MOTION ANALYSIS OPERATION

GENERAL TEMA PROCESS/ CAPABILITIES
    I.   Opening the program/ video file
          a. When first opening TEMA Motion, a **Select Template** window automatically pops up. Select which template is best to use for the specific test. Typically with Two-Phase Flow the Single Cam with XT is chosen, however with any of the templates that are chosen additional diagrams can be added at any time. A description of each template can be found below.
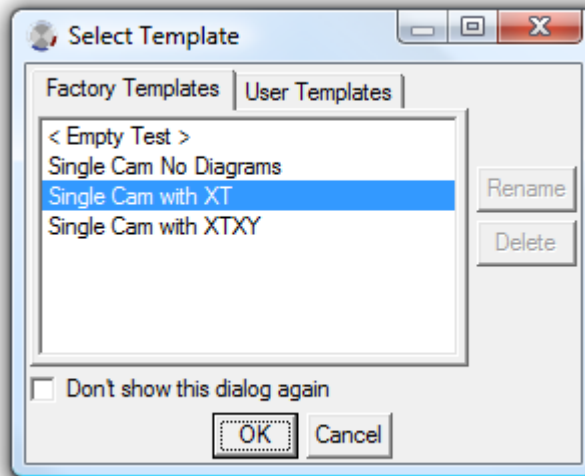
          i. < Empty Test >
             1. Blank Workspace; need to manually insert video and graphs
         ii. Single Cam No Diagrams
             1. Automatically opens window to select video to analyze
             2. No Graphs automatically
        iii. Single Cam with XT
             1. Automatically opens window to select video to analyze
             2. X-axis vs Time graph created automatically
        iv. Single Cam with XTXY
             1. Automatically opens window to select video to analyze
             2. X-axis vs Time graph created automatically
             3. X-axis vs Y-axis graph created automatically

II. Opening video in TEMA
    a. Once a template is chosen, an **Open Image Sequence – View #1** window will
       open automatically. From this window select the video file to analyze.

DISTRIBUTION STATEMENT A: Approved for public release. Distribution is unlimited.
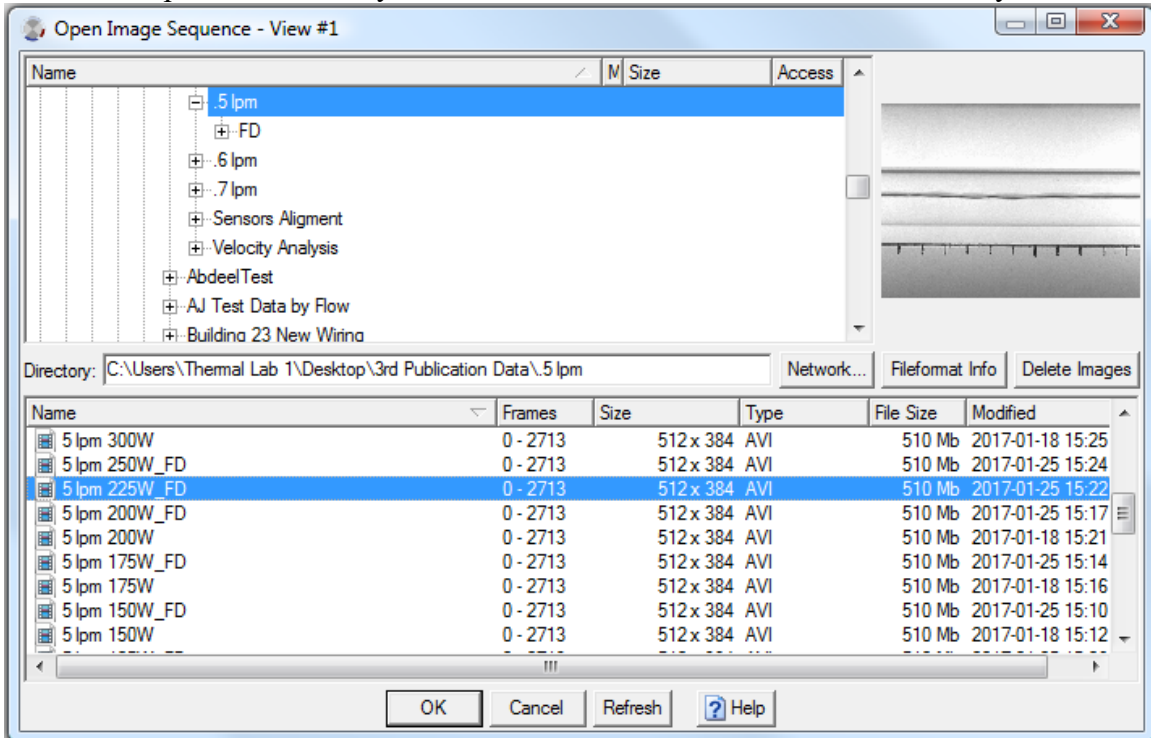
III. Editing video/ image enhancement
   a. Editing Video
   b. Time Properties – Click **Edit**, **Time Properties**. The **Time Properties** window
      will open. The User Defined Interval box allows the user to adjust a defined time
      interval for the video to play, allows the user to manually set the speed of the
      animation, and choose what happens when the video ends.
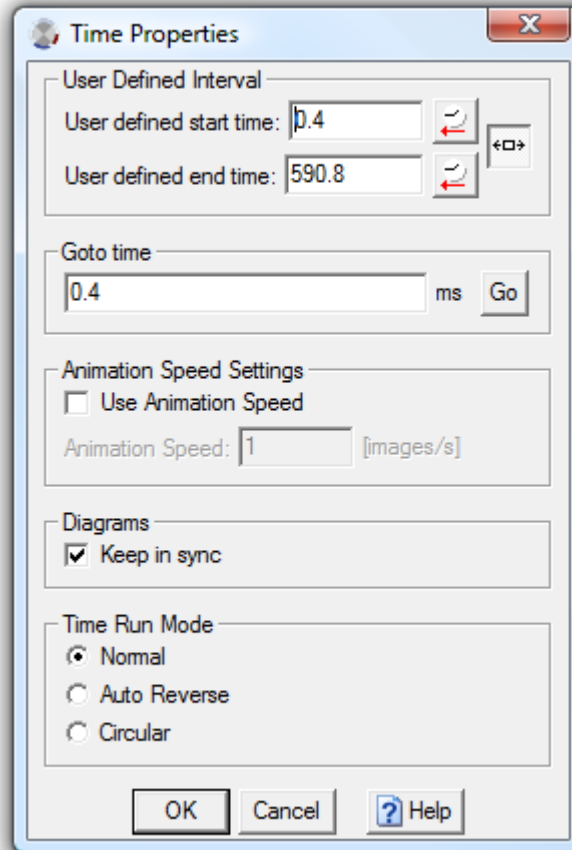
      i. Trimming Video Length
          1. In the User Defined Interval section of the Time Properties box,
             enter the start time and end time that you would like to trim the
             video to.
      ii. Adjusting Animation speed
          1. Check the Use Animation Speed box to manually adjust the speed
             of the playback of the video by manually entering frames per
             second. This adjusts the speed at which the pictures goes to the
             next frame with respect to time.
      iii. End of the video options (Time Run Mode)
          1. Normal – the video stops playing at the end of the file
          2. Auto Reverse – the video reverses and plays the file backwards

3. Circular – the video restarts from the beginning of the file
c. Image enhancement
   i. Right click the video display to select **Image Enhancement**. This allows the user to adjust the brightness, contrast, and gamma to get a better image

DISTRIBUTION STATEMENT A: Approved for public release. Distribution is unlimited.
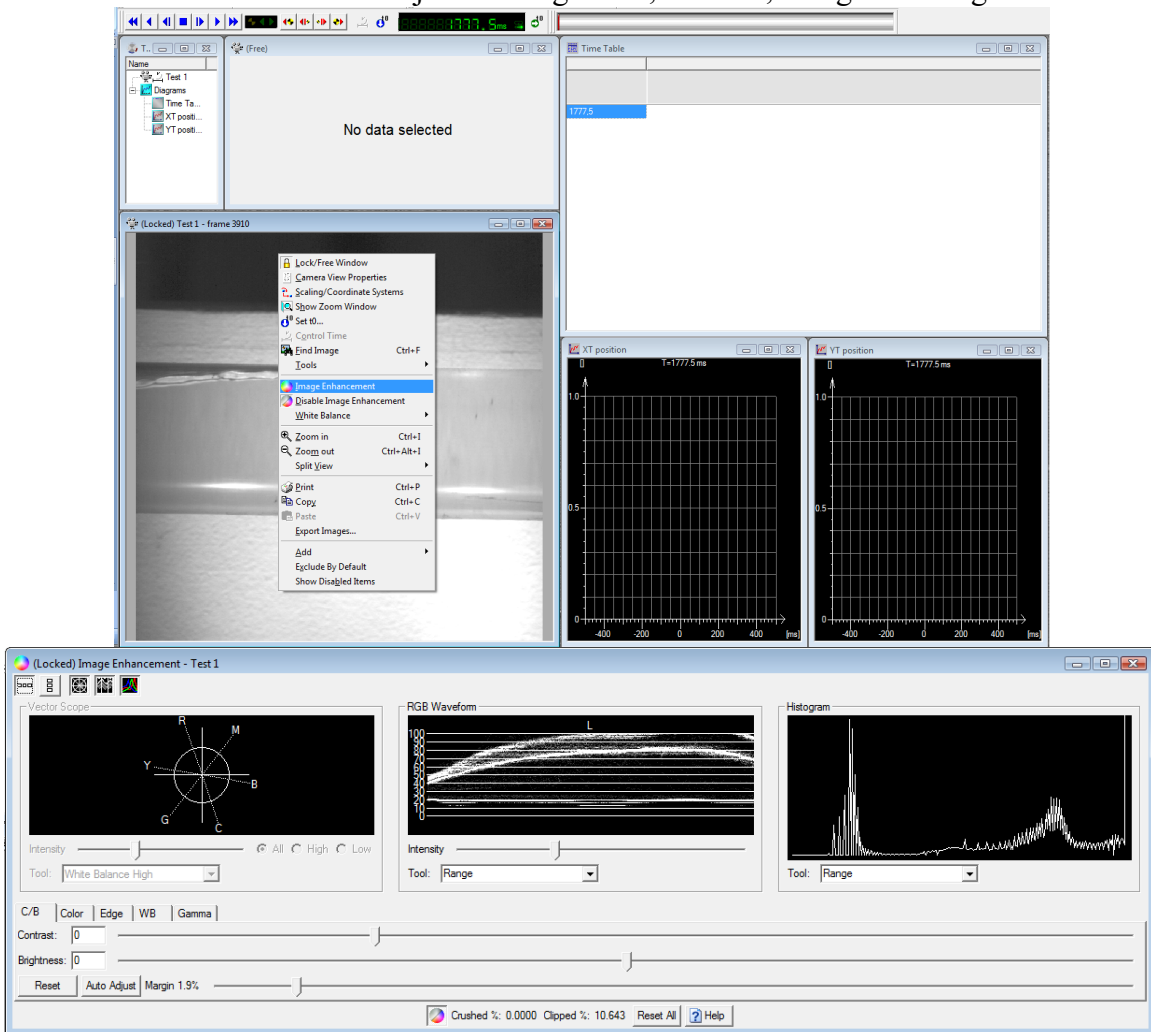
IV.   Tracking points
   a. In order to track points, left click the **Add Point** button in the toolbar shown
       below. This will create crosshairs in the video display where the user can select
       the location of a point to track.
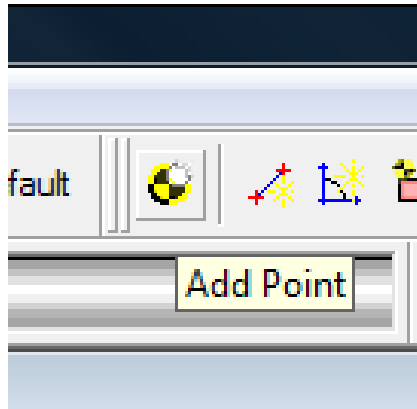
   b. Point Setup
       i. Select a created point in the **Test Contents** window on the left hand side
           of the program interface. Click **Edit** and select **Properties**. This will open
           the **Point Setup** window.

DISTRIBUTION STATEMENT A: Approved for public release. Distribution is unlimited.
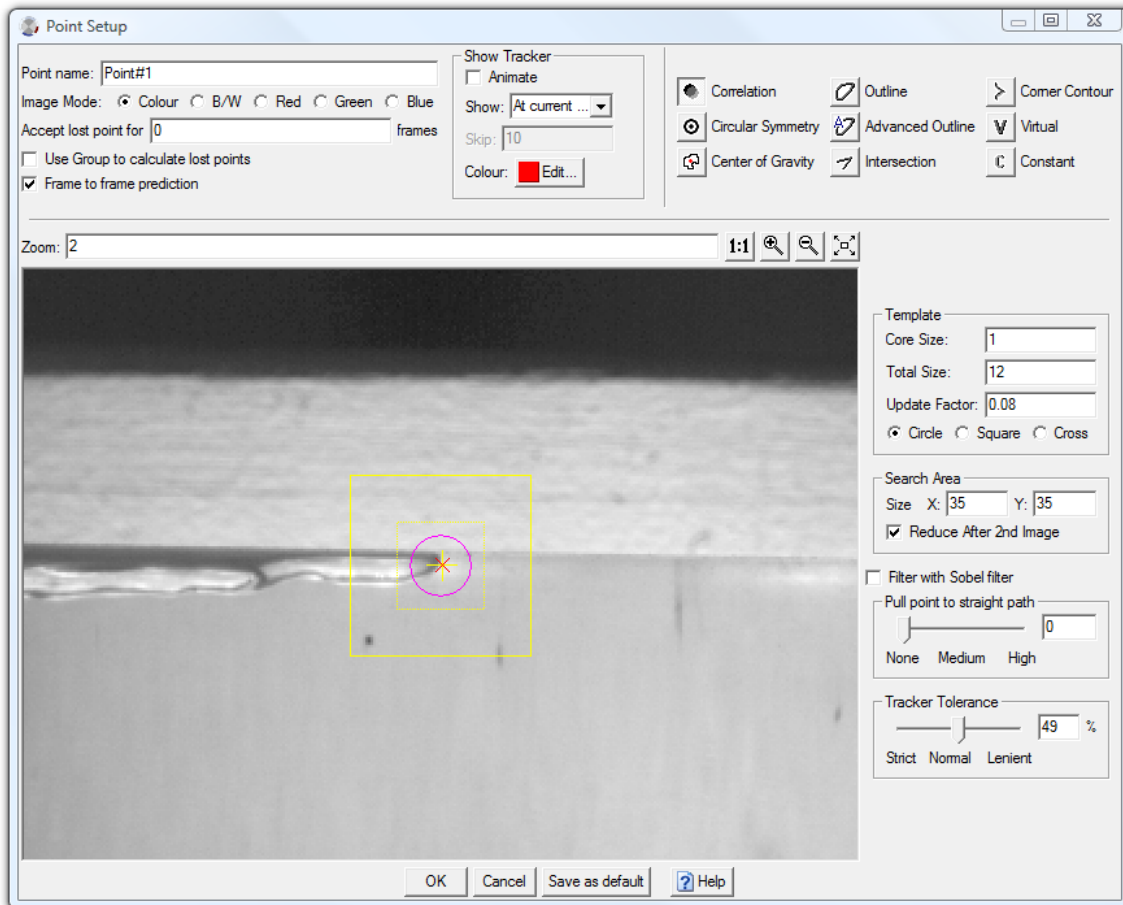
c. Types of Trackers
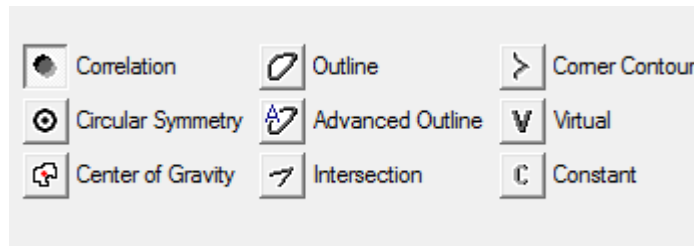
i.   Correlation - looks in each successive image for the area contained within the correlation template. This method is applicable to most cases.
ii. Circular Symmetry - finds the symmetry center of the image within the search area and is applicable to concentric circles, spokes on a bicycle wheel or combinations thereof.
iii. Center of Gravity - tracks a regular, roughly circular shaped object that does not change size and shape during the tracking process.
iv. Outline - tracks the outline of an irregular shaped object that may change size and shape during the tracking process.
v.   Advanced Outline - tracks the outline of an irregular shaped object that may change size and shape during the tracking process. It uses a different method from the Outline tracker in order to track the outline.
vi. Intersection – description not available.
vii. Corner Contour - tracks the curvature of edges, e.g. corners in any shape.

viii. <u>Virtual</u> - specifies that the point is virtual, i.e. its position in successive images is calculated from the positions of the other points in its point group, rather than by measurement. There is no setup procedure.

ix. <u>Constant</u> - specifies a fixed point in the image that can subsequently be used as a reference point for analysis and display.

d. Distances

i. Distances can be tracked between two points by going into **Camera** and selecting **Add Distance**. This will open the **2D Distance Setup** window, where the distance can be assigned between two points.
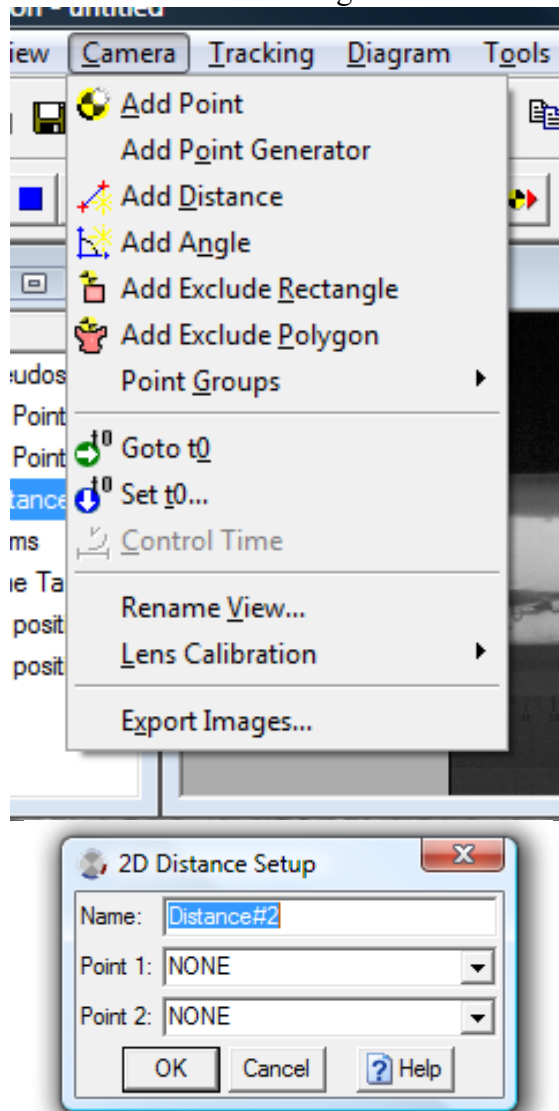
e. Angles

i. Angles can be calculated with either 2 points compared with a horizontal or vertical axis, or an angle described by 3 or 4 points. Click **Camera** and select **Add Angle**. This will open up the **Angle Setup** dialogue box which allows the user to define the angle being measured.
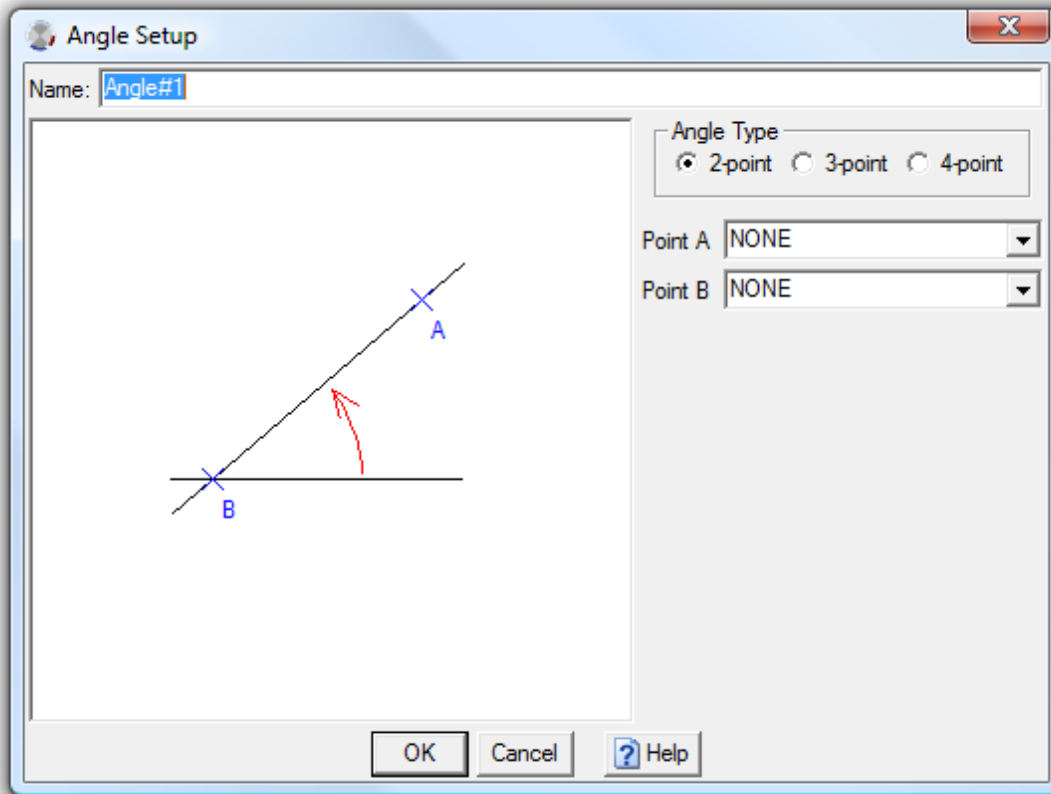
  f. Scaling and coordinate systems <mark>**MUST USE FIRST FRAME OF VIDEO**</mark>
    i. Scaling
      1. Create two points on the measuring scale that are a known distance apart.

DISTRIBUTION STATEMENT A: Approved for public release. Distribution is unlimited.
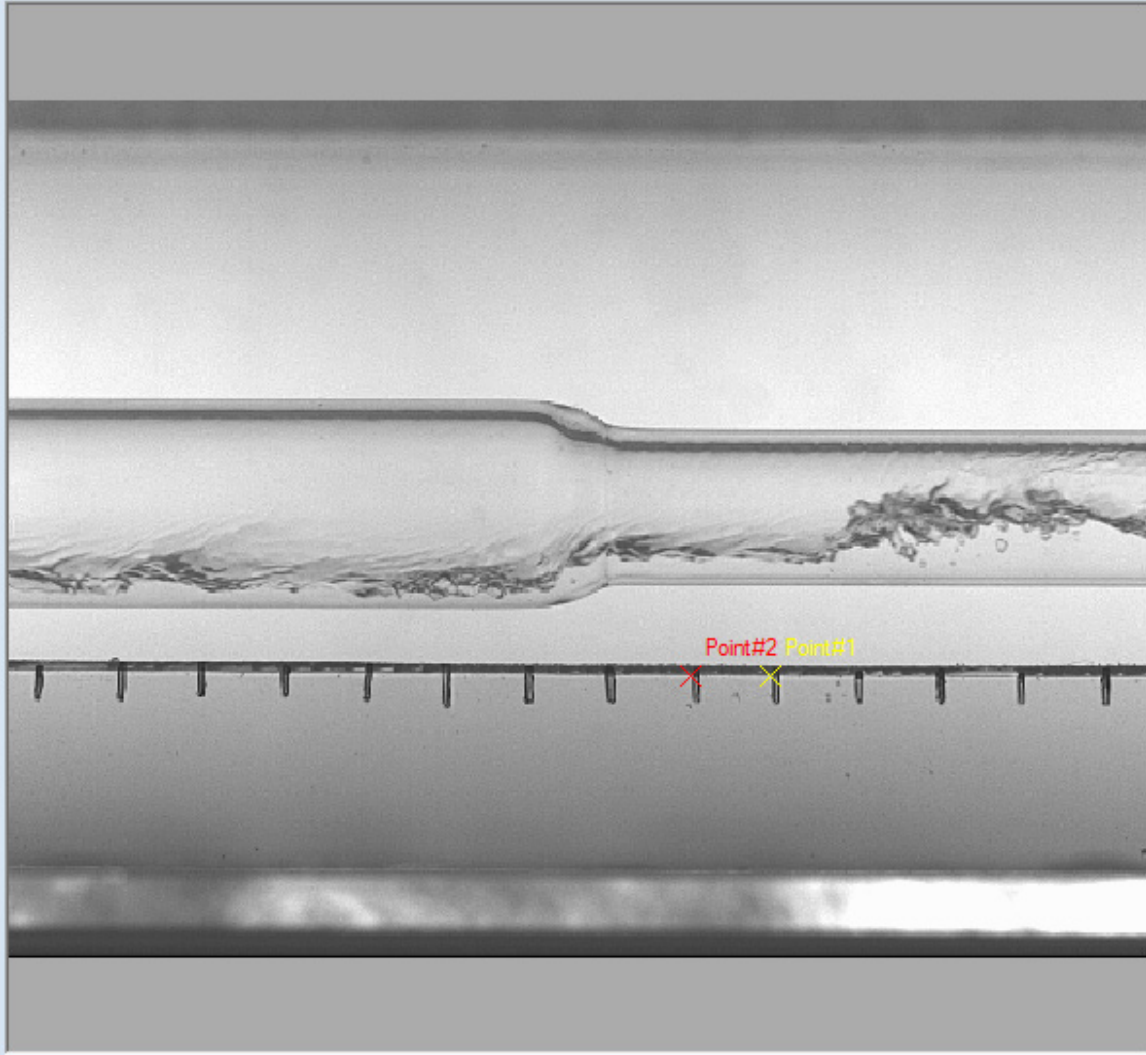
2. Click **Edit** and select **Scaling/ Coordinate Systems**
3. Under the **Mode** box, select **Single Parallel**.

DISTRIBUTION STATEMENT A: Approved for public release. Distribution is unlimited.
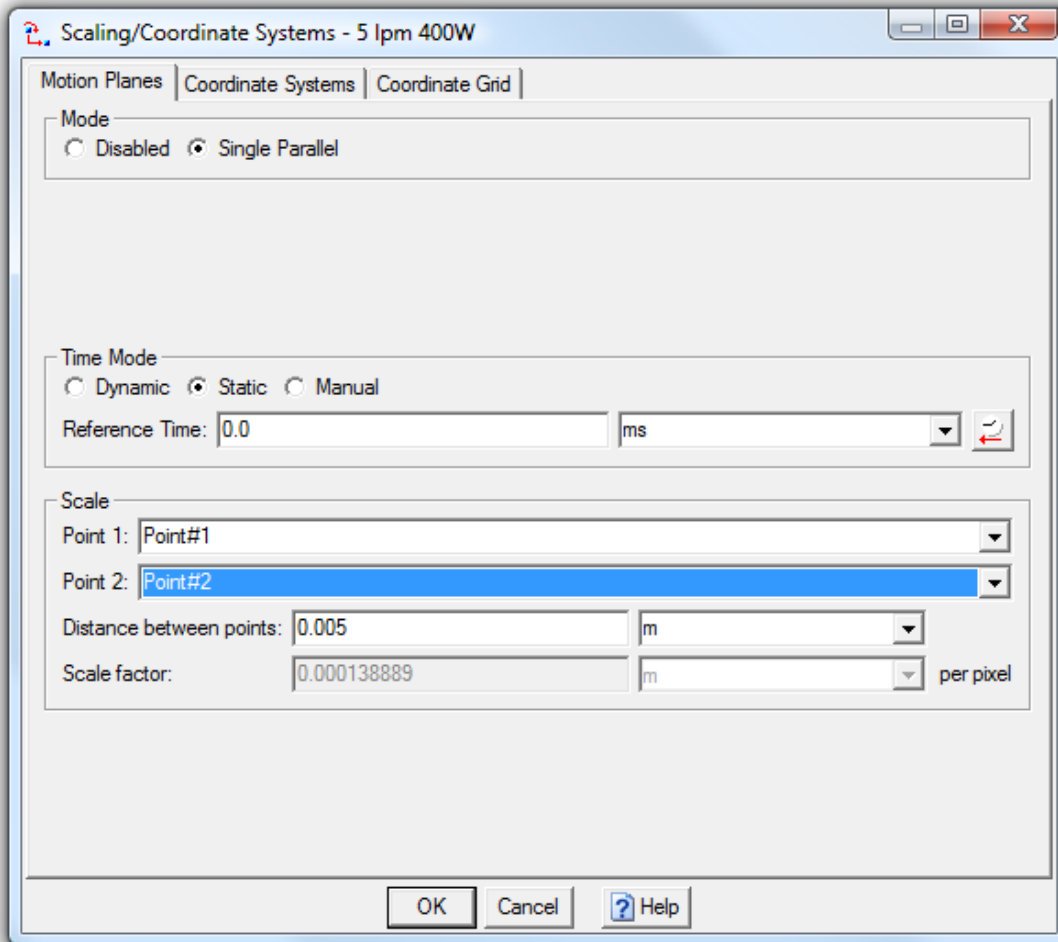
4. In the Scale box, select Point 1 and Point 2 and type in the actual distance between points. This will convert the scaling from pixels into meters.
5. Select the **Coordinate Systems** tab and click **Add** to create a new coordinate system.
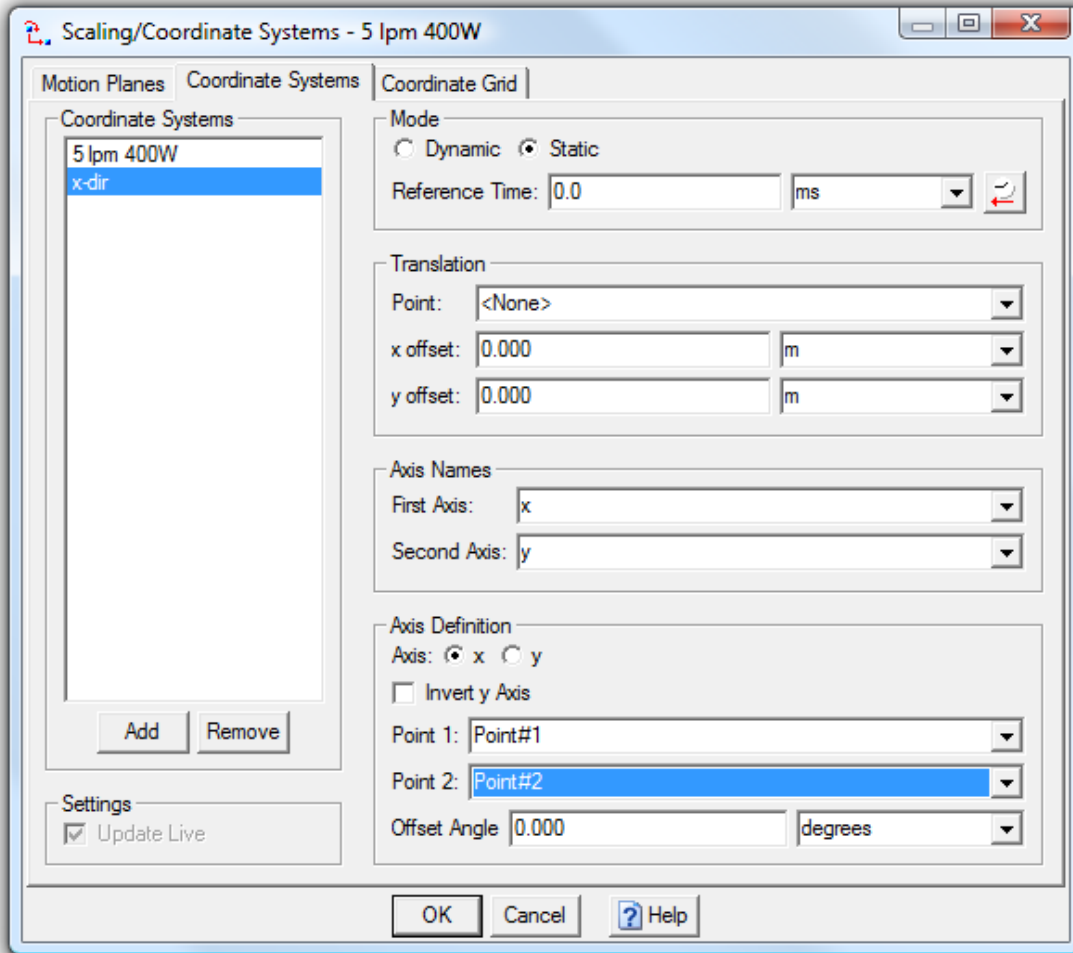
6. Name the new coordinate system.
7. Under Axis Definition select which points will create the new axis, starting at the point defined by **Point 1:** going through the point defined by **Point 2:**. In this example the new x-axis for the coordinate "x-dir" goes from Point#1 through Point#2.

g. Creating Graphs
    i. When TEMA first opens and a template is chosen, 0-3 graphs will open automatically depending on which template that is chosen beginning. "Single Cam No Diagrams" produces zero graphs. "Single Cam with XT" produces two graphs: XT Position and YT Position, and "Single Cam with XTXY" produces 3 graphs: XY Position, XT Position, and YT Position. Graphs can be edited or added at any time to display different information.
        1. Create a new graph by clicking **Diagram** and selecting **New** to open a pull down menu. Here you can create a new diagram from the following options:
            a. XT Diagram
            b. Multi-Axis Diagram
            c. XY Diagram
            d. Advanced Diagram

47

e. Image Diagram
f. Time Table
g. Tiled Window.
    ii. Editing Graphs
        1. Select a graph you would like to edit by clicking anywhere on the diagram and go to **Edit** and select **Properties.**
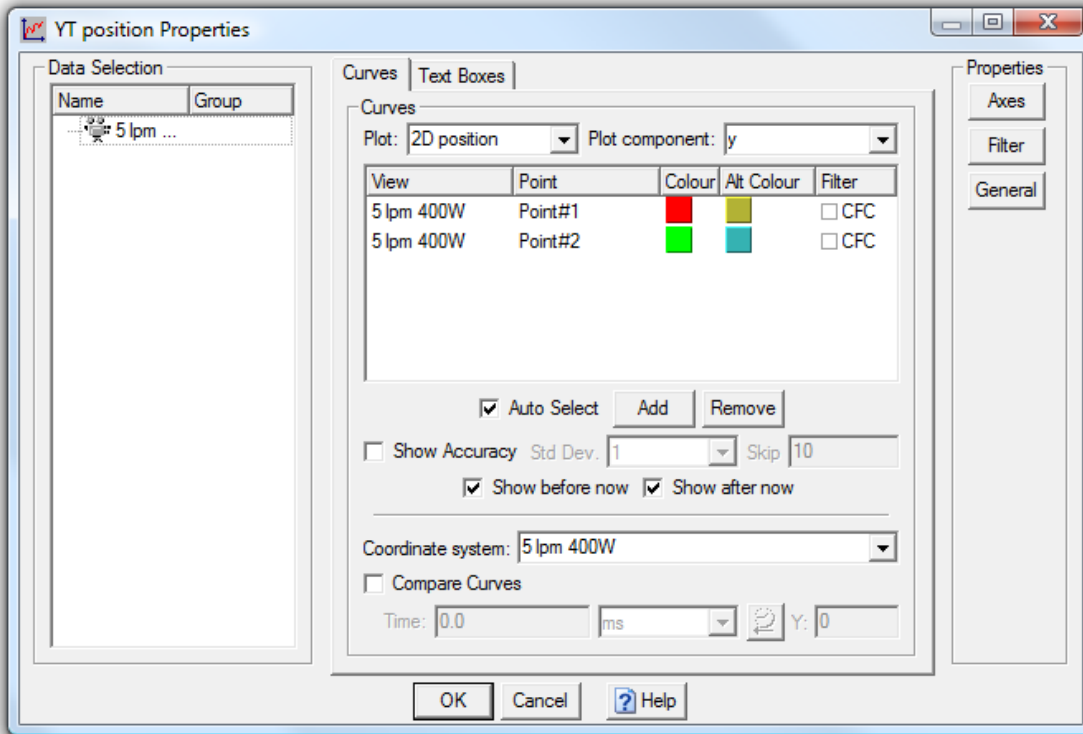
        2. Here you can select the **Coordinate System**, what information is plotted, and what component is being plotted. You can also **Add** and **Remove** points that are being plotted in the diagram. In the **General** tab on the right hand side, you can edit the title of the graph as well as the legend.
h. Time Table
    i. After points of interest have been tracked and automatically graphed, the data can be shown numerically as well in the **Time Table**. The properties can be edited by clicking anywhere in the **Time Table** and clicking **Edit** and selecting **Properties.**
    ii. In the **Time Table** properties, data can be selected from different points. Time derivate can be chosen as well as alternate coordinate systems.
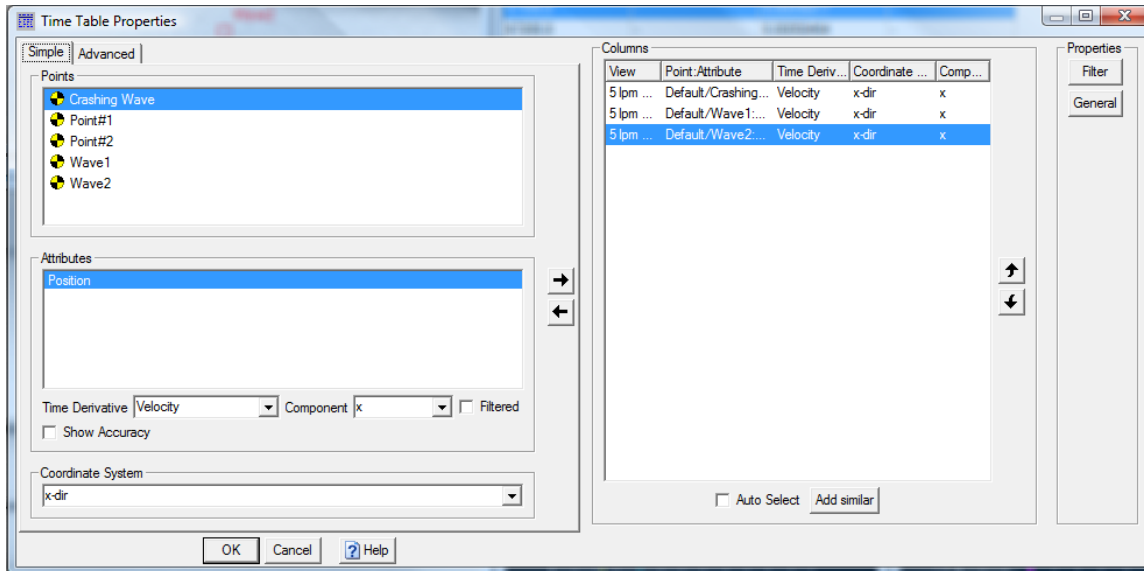
iii. Click the **Right** arrow to enter the data into the table. The order of the data in the **Columns** box can be altered with the UP and DOWN arrows.

iv. After clicking **OK**, the data automatically is entered into the table. The data will trim itself automatically to not include time steps where there are no points being tracked.

i. Transferring Data from **Time Table** into **Microsoft Excel**

i. Select all of the data by pressing **CTRL+A**.

ii. Copy all of the data either by **right clicking** and selecting **Copy**, or by typing **CTRL+C.**

iii. Paste data into a new Microsoft Excel workbook either by **right clicking** and selecting **Paste**, or by typing **CTRL+V.**

iv. All of the data that is copied over from TEMA will contain an "X" where there is no recorded data and a "," instead of a decimal point. In order to correct this, press **CTRL+F** to open up a **Find and Replace** window.
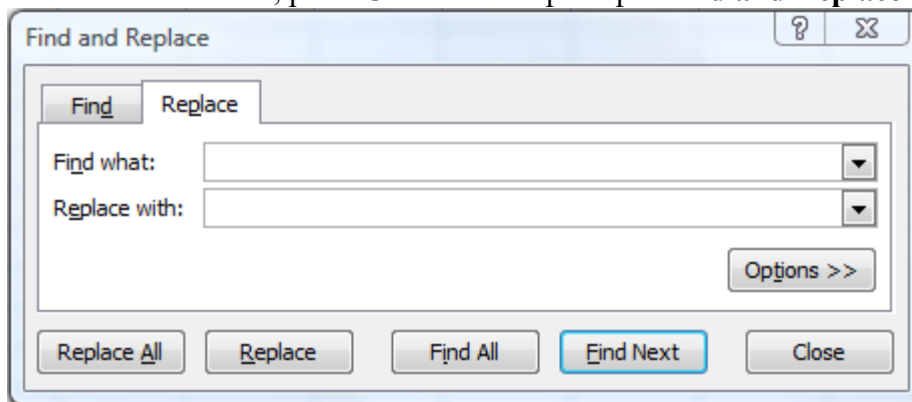
v. In the **Find what:** box, type in "," without the quotes. In the **Replace with:** box, type in "." without the quotes. The completed box should look like the box below. Click **Replace All**. This will replace every "," with a "." Throughout the worksheet.

49
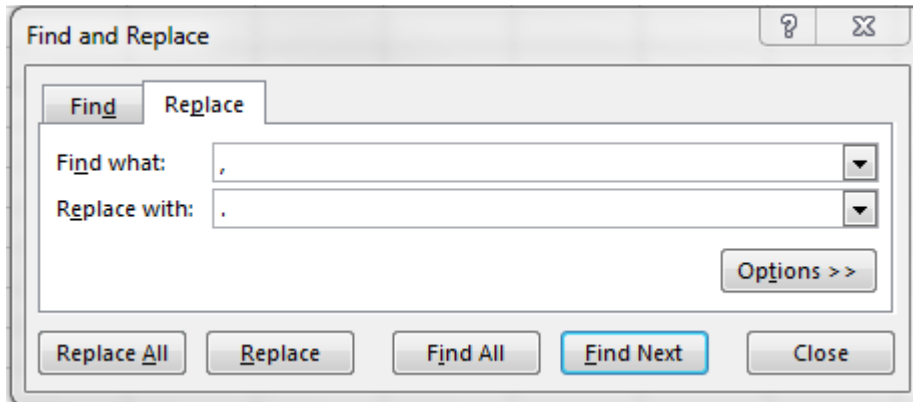
vi. In order to get rid of the "X", open the options by clicking the **Options >>** Button.
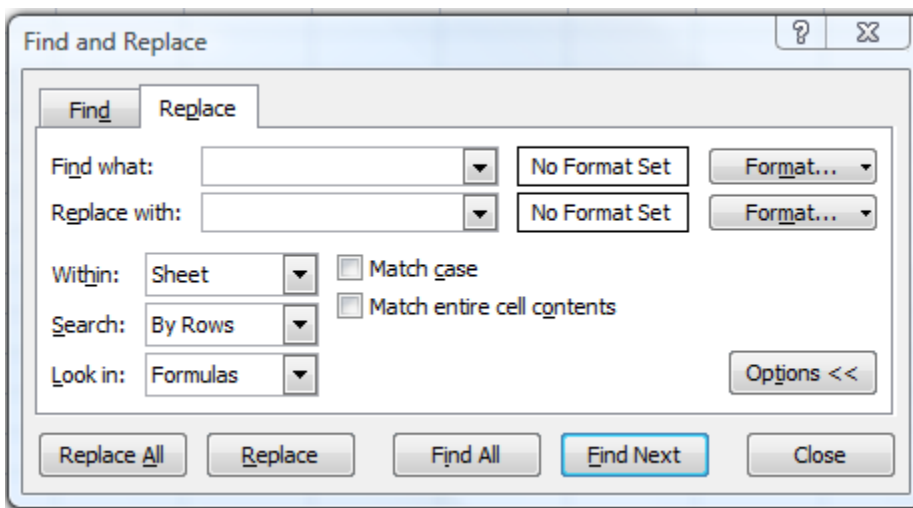
1. In the **Find what:** box, type in "X" without the quotes. Leave the **Replace with:** box empty.
2. Select the box to **Match case**, and click **Replace All.** This will remove every "X" in the worksheet and allow the user to manipulate the data like any other Excel worksheet. The completed **Find and Replace** window should match the one below.
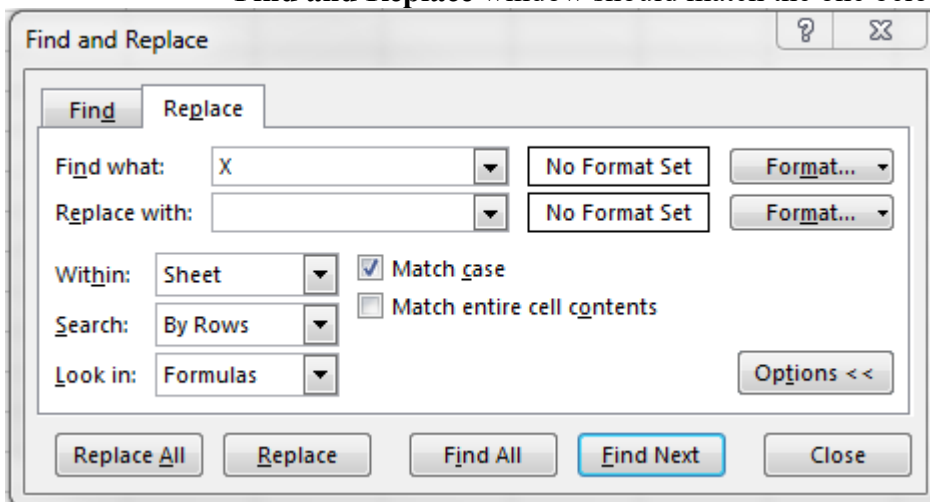
V. Trace
   a. The Trace feature allows the user to view the path traveled by a tracked point. You can either view the path before the point gets there, have the program track the path after the point passes, or show the path before and after the point passes.
   b. Click anywhere on the video display and go into **Edit** and select **Properties** to open up the **Camera View Properties Window.** Select the **Tracking** tab at the top of the window.
   c. In the **Trace** box, you can select if you would like the path to appear before the point gets there and disappear after the tracked point has gone through it, select **Show before now.** If you would like the path to appear after the point passes through the path, select **Show after now**. Alternatively, if you would like the path to show all times and the tracked points can go along the path, select **All.**
   d. The trace length can also be adjusted at any time by typing in the number of frames to trace in the **Trace Length** box.
   e. Select **OK** to close the box and apply the changes that you have made.

VI. Additional Help

DISTRIBUTION STATEMENT A: Approved for public release. Distribution is unlimited.
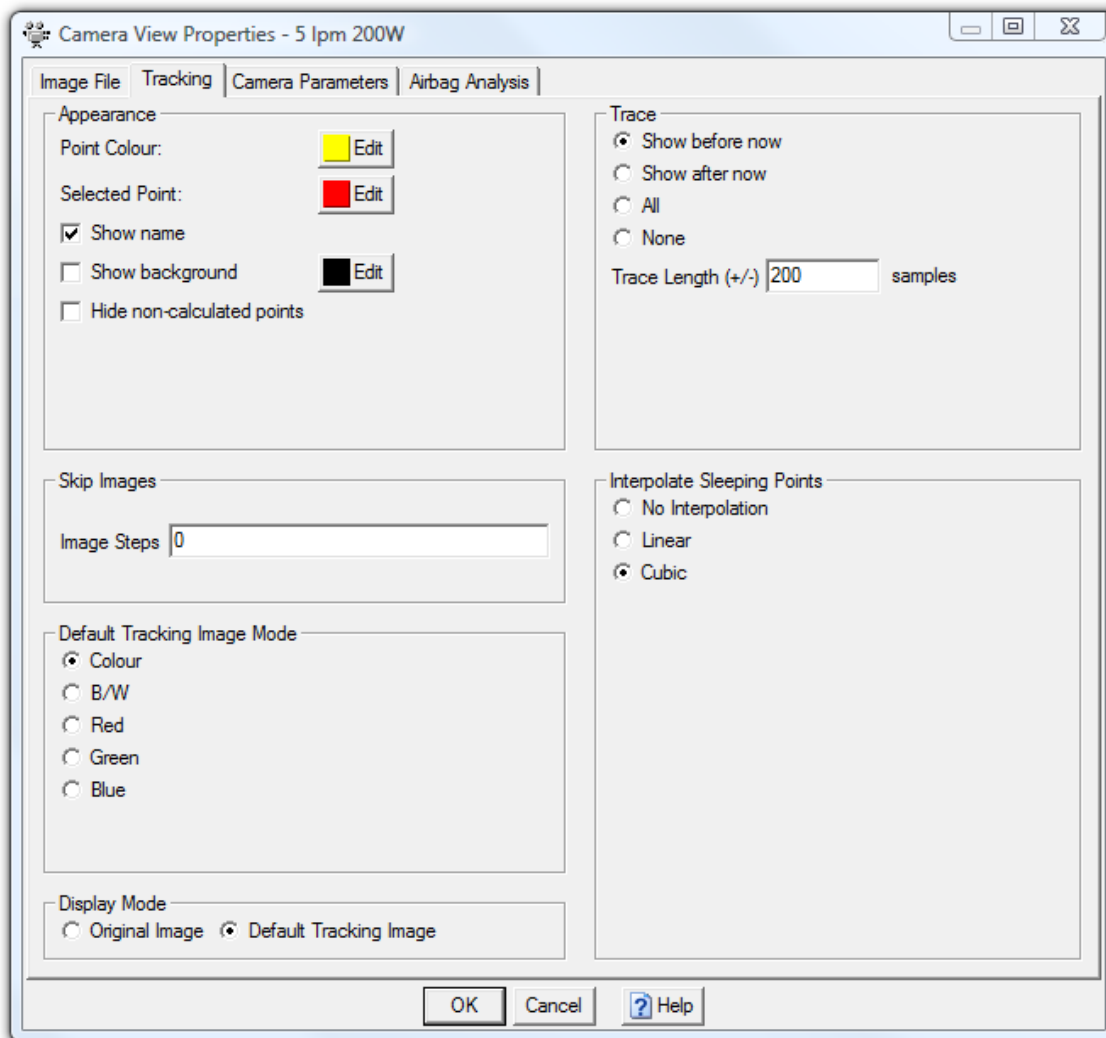
a. For additional help for these or other processes, the TEMA Manual is available under the **Help** tab by selecting **Main Window**. This document can be searched for specific information; however, it does include information for features that are not available on this specific version of TEMA Motion.

GUIDE FOR TWO PHASE FLOW

1. Create new test by either opening TEMA or clicking the [icon] icon.
2. Under the **Select Template** box, select **Single Cam with XT**
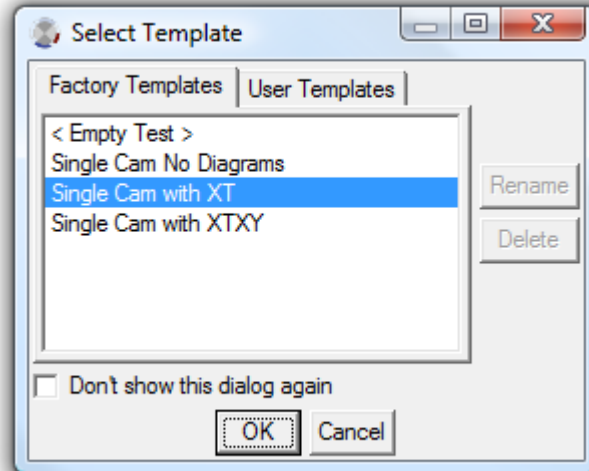
3. This will automatically open up the **Open Image Sequence – View #1** box. In this box, select which video file you would like to analyze and click **OK**.

DISTRIBUTION STATEMENT A: Approved for public release. Distribution is unlimited.
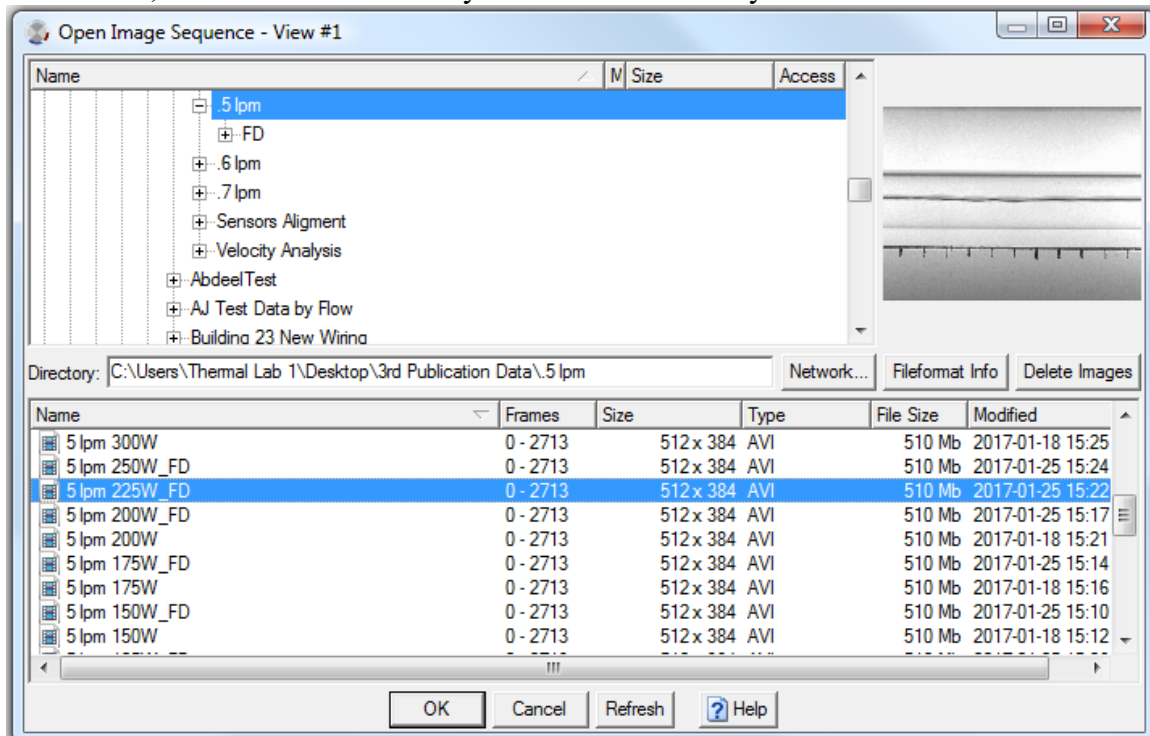
4. Create a new scaling/ coordinate system
   a. Add two points a known distance apart along the x-axis.
      i. Click ⬤ on the toolbar to add a new point. This will change your cursor to crosshairs over the video frame. **Left Click** to place a point. This will automatically be named Point#1; however this can be changed later.
      ii. Choose a location for Point#1 along the known scale in the video. Select the general location for the point in the large video frame, and then fine tune your selection once the smaller window automatically zooms into the new point. For accuracy, always try and choose the same side between markers. For example, in this case, Point#1 is located on the left side of the vertical hash marker and the bottom horizontal line.

(Free) 5 lpm 225W_FD - Point#1
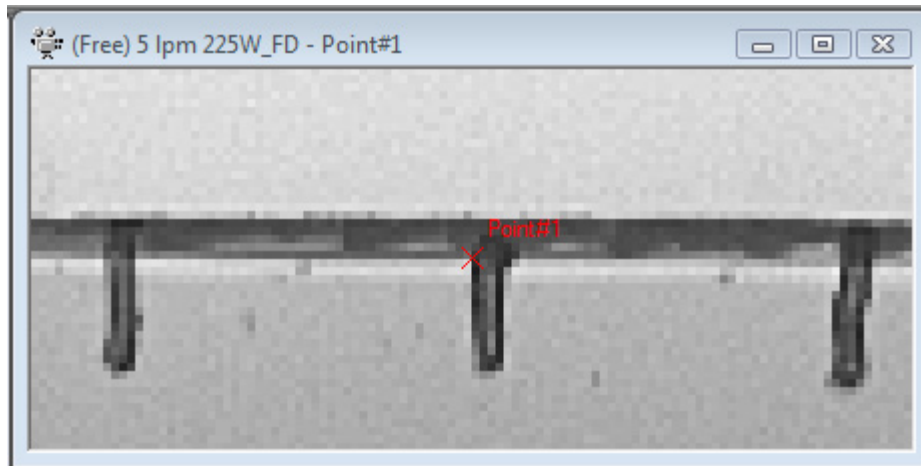
      iii. Once Point#1 has been chosen, click ⬤ again to create another new point. This will automatically be named Point#2.
      iv. Choose a location for Point#2 along the same horizontal line. Typically the vertical hash marker directly to the left is chosen. Ensure that the same side of the hash marker is chosen for Point#2 as was chosen Point#1. For example, Point#2 will also be located on the left side of the marker and the bottom of the horizontal line.

(Free) 5 lpm 225W_FD - Point#2
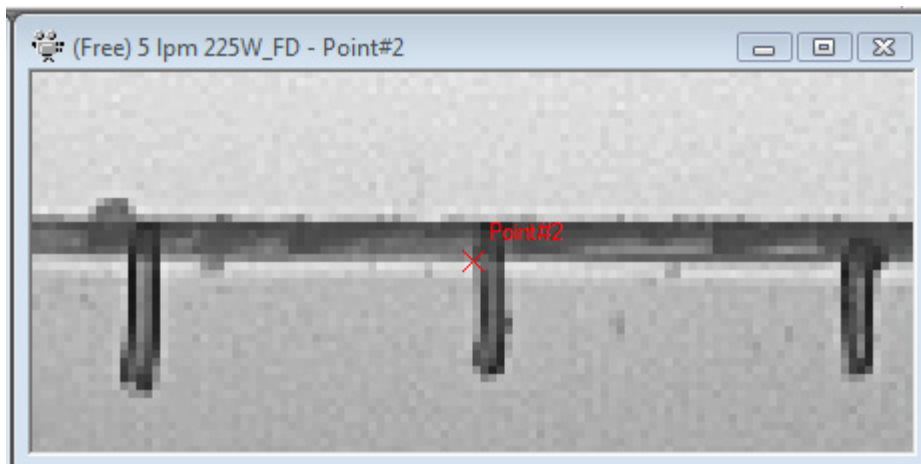
      v. Ensure that both points are along the same horizontal axis by looking at the **YT position** graph on the right side of the TEMA program. You may

need to adjust the height of Point#2. When the two points are at the same height, the **YT position** graph will show the two points on the graph as one.
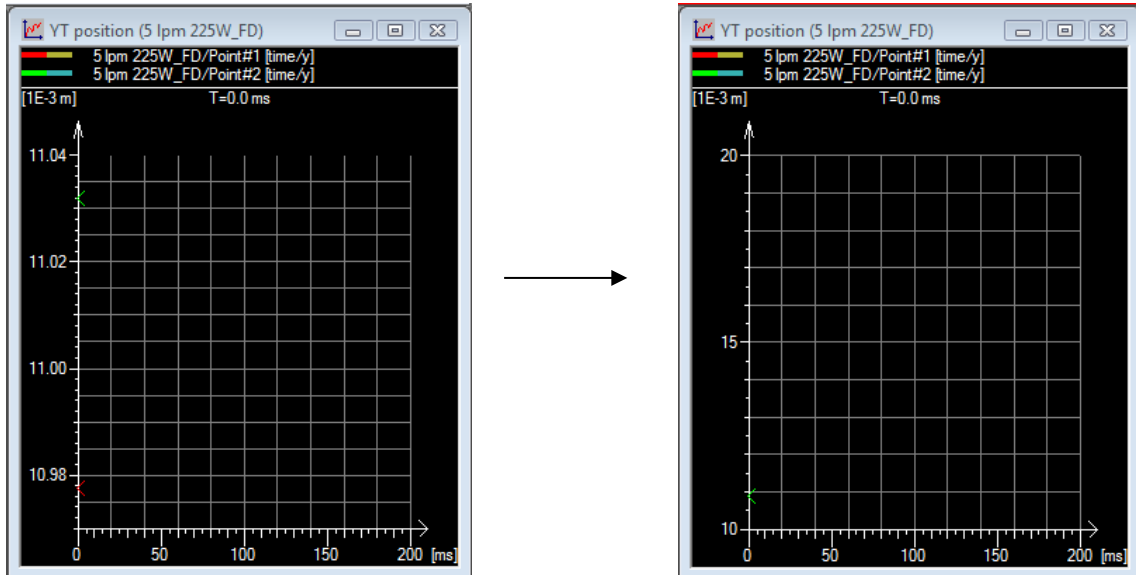
b. Under the **Edit** tab, select **Scaling/ Coordinate Systems.** This will open up the **Scaling/ Coordinate Systems** box for this video file.

DISTRIBUTION STATEMENT A: Approved for public release. Distribution is unlimited.

Scaling/Coordinate Systems - 5 lpm 225W_FD

Motion Planes | Coordinate Systems | Coordinate Grid

Mode
- ⦿ Disabled ○ Single Parallel

OK   Cancel   ? Help
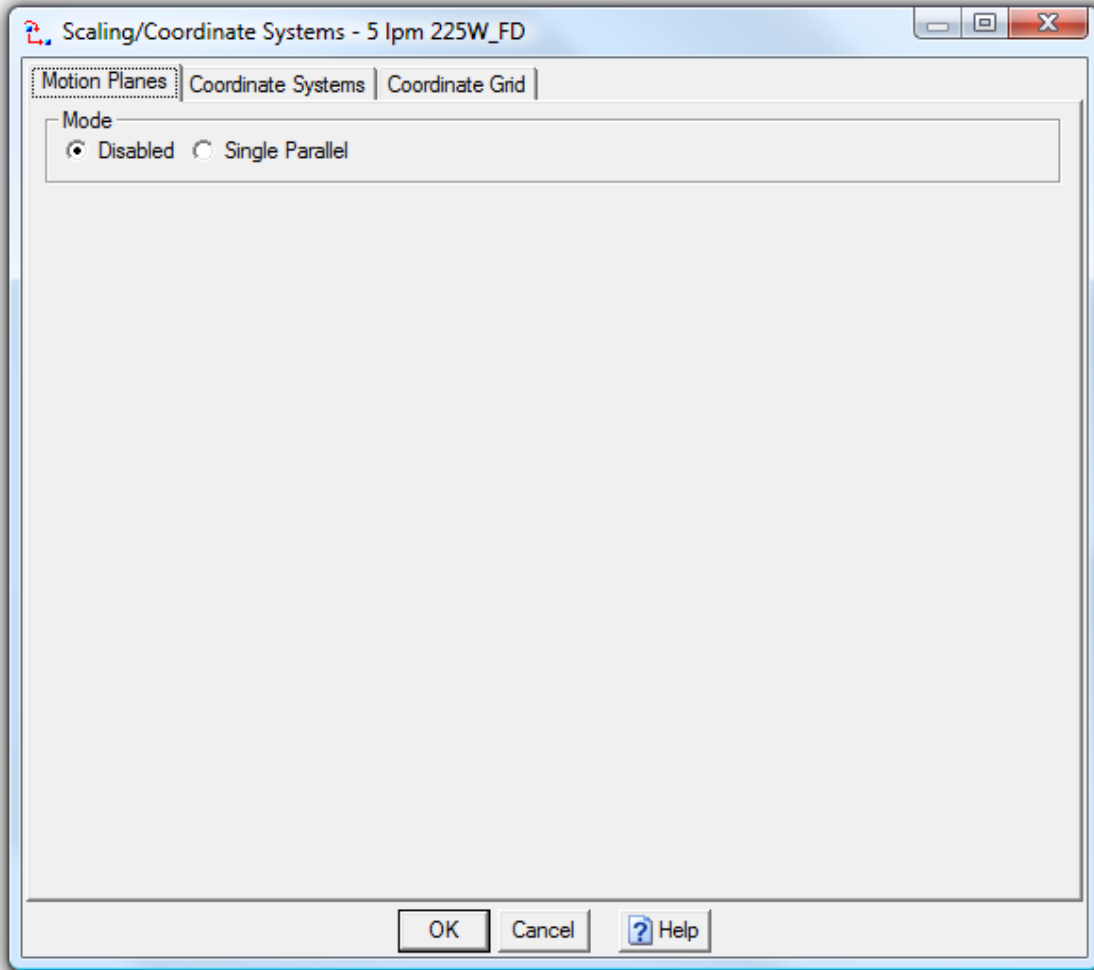
c. Under **Mode** select **Single Parallel**.
d. Under the **Scale** section, choose **Point 1:** as the right-most point along the horizontal axis. In this case it is Point#1. Under **Point 2:** select the left-most point along the horizontal axis. In this case it is Point#2. The distance between these points is the physical distance between the two points. In this case using this measurement device the distance is 5mm or 0.005 m. This will automatically change the graphs to plotting with a scale in meters versus pixels. A completed box described above can be seen below.

Scaling/Coordinate Systems - 5 lpm 225W_FD

Motion Planes | Coordinate Systems | Coordinate Grid

Mode
○ Disabled   ● Single Parallel

Time Mode
○ Dynamic   ● Static   ○ Manual
Reference Time: 0.0   ms

Scale
Point 1: Point#1
Point 2: Point#2
Distance between points: 0.005   m
Scale factor: 0.000108696   m   per pixel

OK   Cancel   ? Help
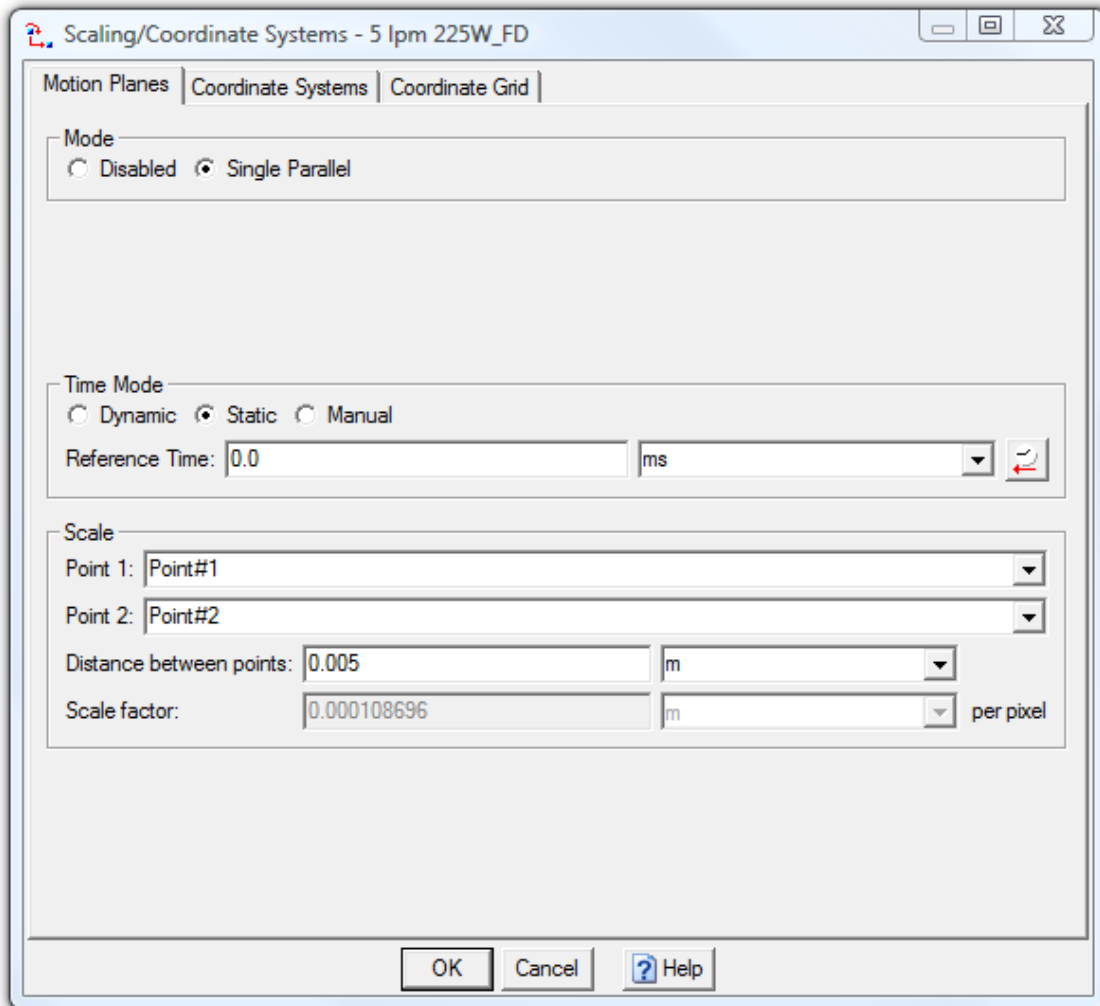
e.   Select the **Coordinate Systems** tab in the **Scaling/ Coordinate Systems** box.
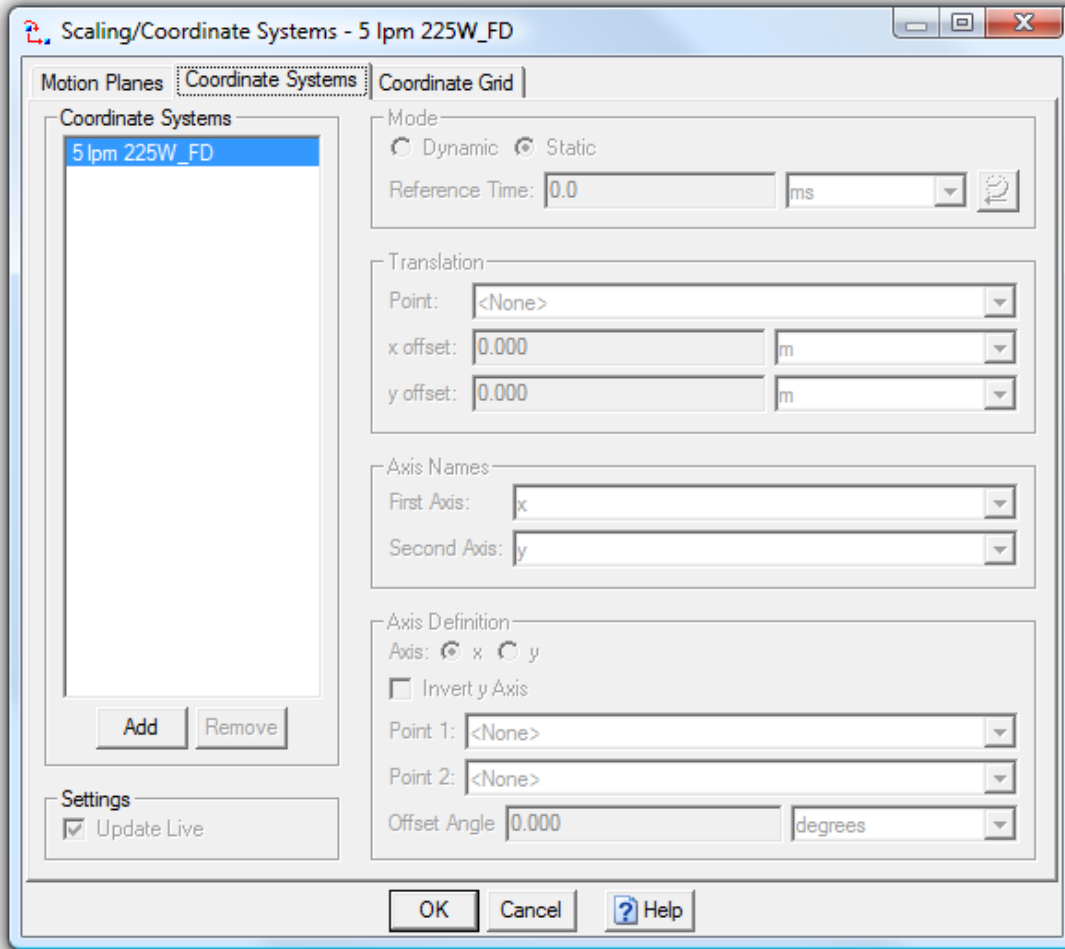
f.   On the left hand side of the box, select **Add** to create a new coordinate system. This will open an addition box where you can name the new coordinate system. Name the new coordinate system, in this case the system will be named X-dir_NEW.
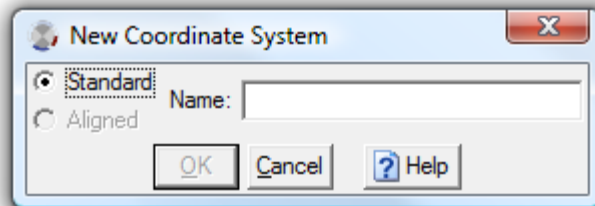
g. Under the **Axis Definition** of the new coordinate system, define the new x-axis by selecting the **X bubble** under **Axis.** Select **Point 1:** as Point#1 and **Point 2:** as Point#2. **Note**: This will create a new x-axis FROM Point#1 TO Point#2. If you have created Point#1 on the left side of Point#2, you may need to either add an **Offset Angle** or select different points for **Point 1:** and **Point 2:**. Otherwise, the new axis will be made properly. This new coordinate system is necessary with our two-phase flow videos as it will allow the flow to be traveling in the positive X direction, which will make our velocities and accelerations positive.
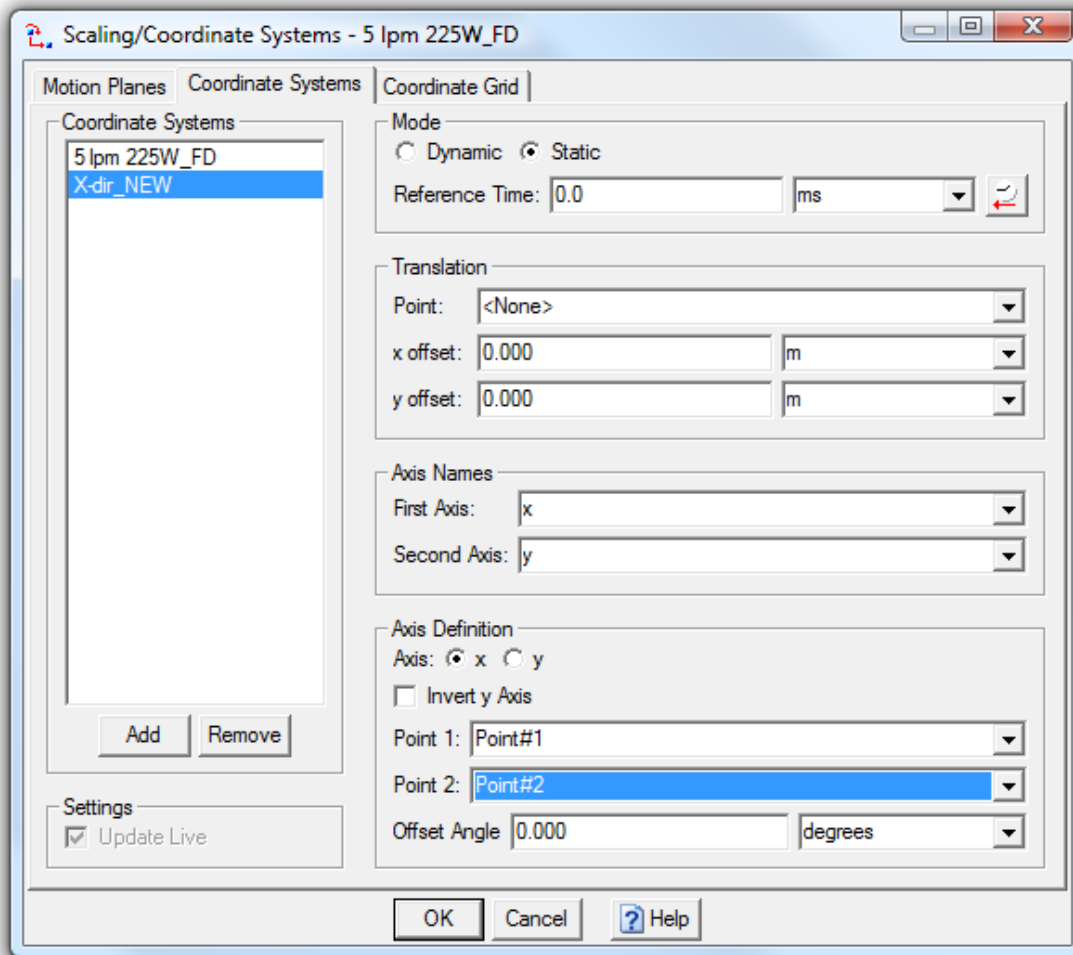
h. Click **OK** to close the box.

5.   Now that a new scaling and coordinate system has been made, it is a good idea to save the work. Select **File**, **Save Test As…**, and type in the file name. The naming convention for TEMA analysis videos is: TEMA_(Flow Rate)_(Heater Power)_(Expansion/Fully Developed Flow). After the File name has been typed, select **Save.** Be sure to save your work often.
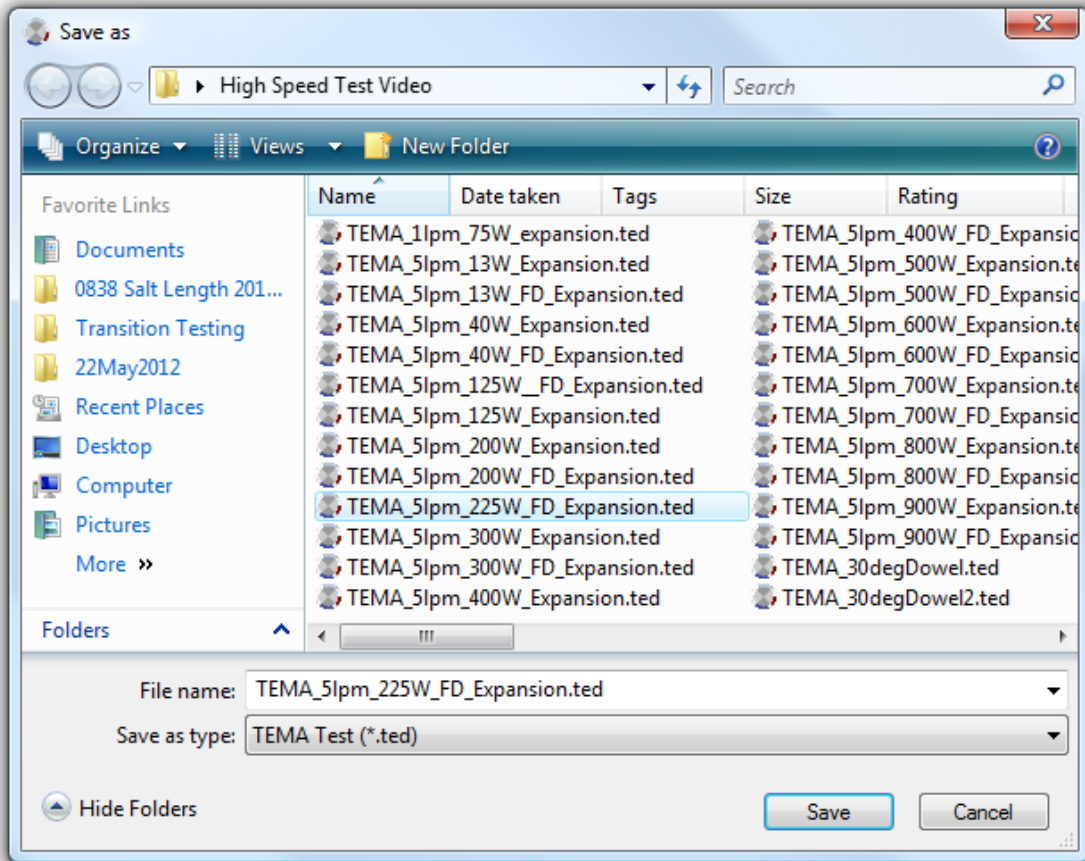
6.   In the **Test Contents** box on the left hand side of the window we can select between Point#1 and Point#2.
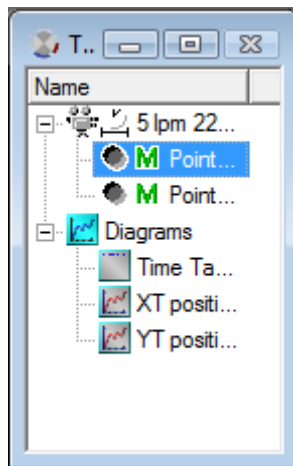
Since we are done with these points, disable them by selecting a point and pressing

CTRL+D or by selecting on the toolbar. You will notice a new icon of a red X will appear on the left side. Disable both Point#1 and Point#2. Disabling points allows TEMA to ignore the location of disabled points when tracking other points.

Points can be re-enabled at any time by pressing **CTRL+E** or by selecting on the toolbar.
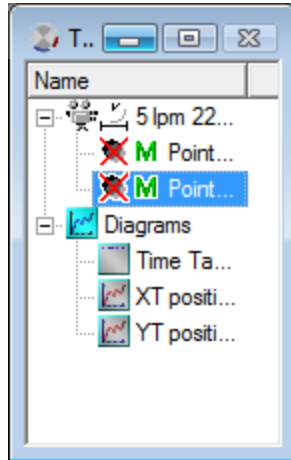
7.   Select the **XT position** graph by clicking anywhere on the graph. Press **ALT+P** to open up the properties window for this graph.
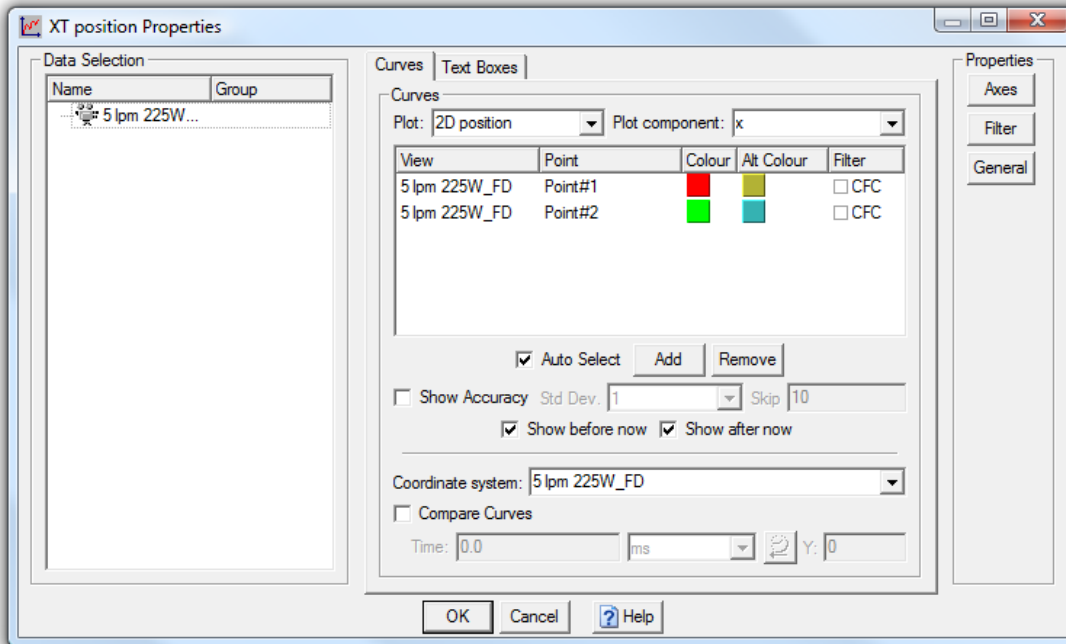
8.   Change the **Coordinate system:** to the new coordinate system that we created and select **OK.** This will change the coordinate system of the **XT position** diagram to a positive displacement in the left direction.

9.   Select the **YT position** graph by clicking anywhere on the graph. Press **ALT+P** to open up the properties window for this graph.

DISTRIBUTION STATEMENT A: Approved for public release. Distribution is unlimited.
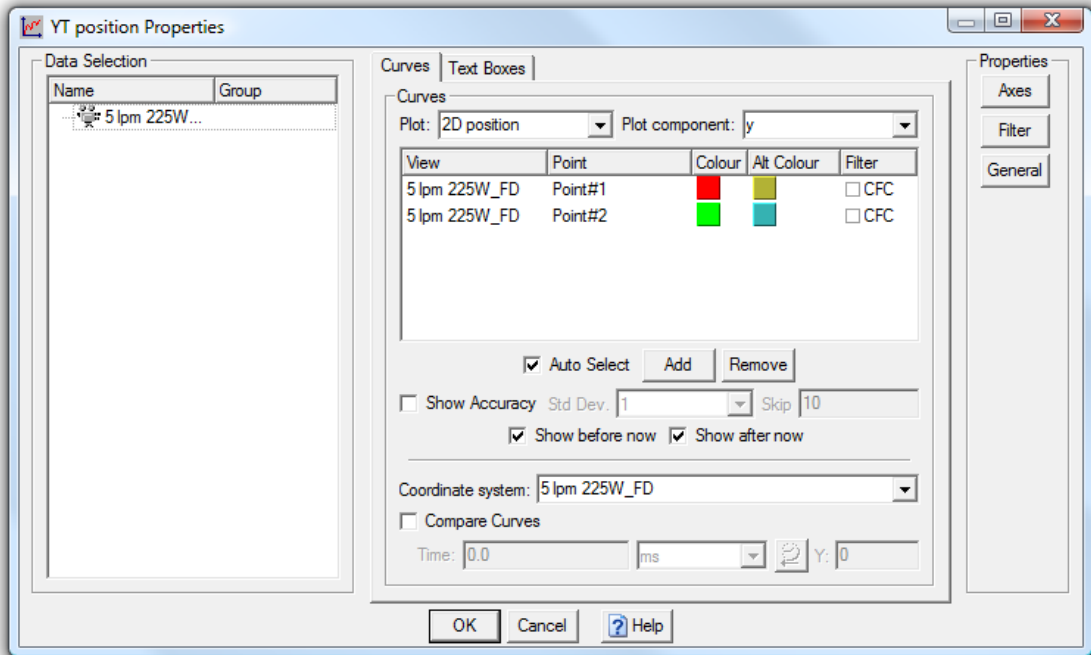
10. Change the **Coordinate system:** as before, but do not close out of this window. Since YT position is usually not of interest for our research, we will change this graph to XT velocity.
   a. Under the **Plot:** pull down menu, select 2D velocity.
   b. Under the **Plot component:** pull down menu select x.
   c. In order to change the title for this graph, go into the **Properties** box on the right side and select **General**. Change the title to XT velocity. The properties should now look like the window below.
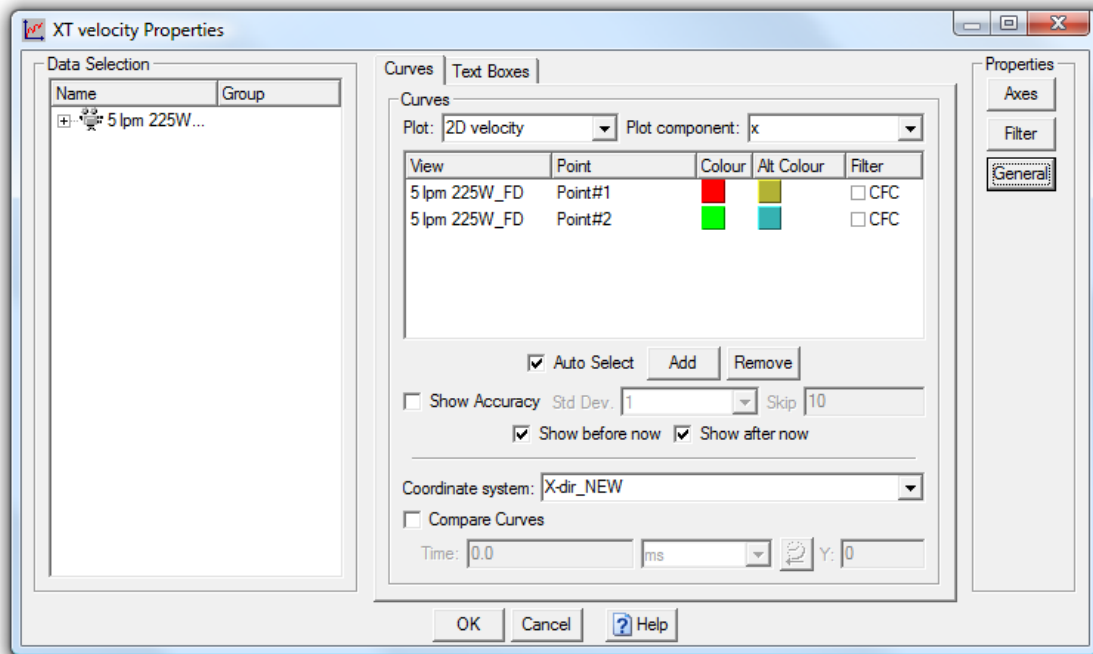
   d. Select **OK** to close the window.

11.	Go into **Edit** and click **Time Properties** to open the **Time Properties** box. Under **Time Run Mode** select **Circular**. This makes the video loop back to the beginning when it reaches the end, which will make it easier when watching the film for points to track.
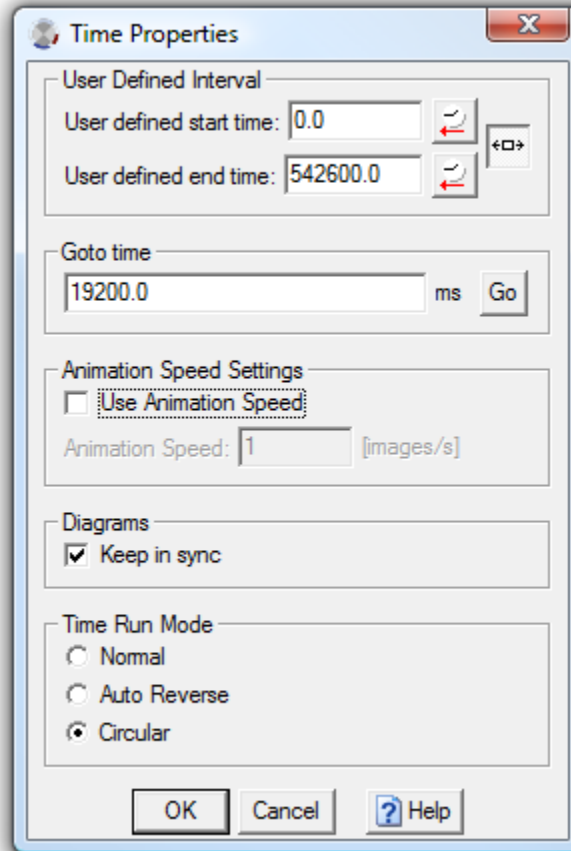
12.	Scan through the video by clicking [▶]. While watching the flow, look for features that either represent the flow or are features of interest to track. Such features could be a droplet of liquid traveling through the vapor section or tracking a bubble of vapor through the sudden expansion. Ideally, the point you intend to track should not intersect with other objects or features that may make it difficult to track the point.

13.	Once a feature is chosen, pause the video where you would like to begin tracking the feature by clicking [■]. Add a new point to track by clicking [⊙] and select the location in the video frame of the point that you wish to track. When the smaller video frame zooms into this point, you can fine tune the location that you wish to track. The software seems to do best if tracking the edge of a light or dark colored area or a dark colored spot surrounded by a light colored area or vice versa. An example of a light spot surrounded by a dark area is below.
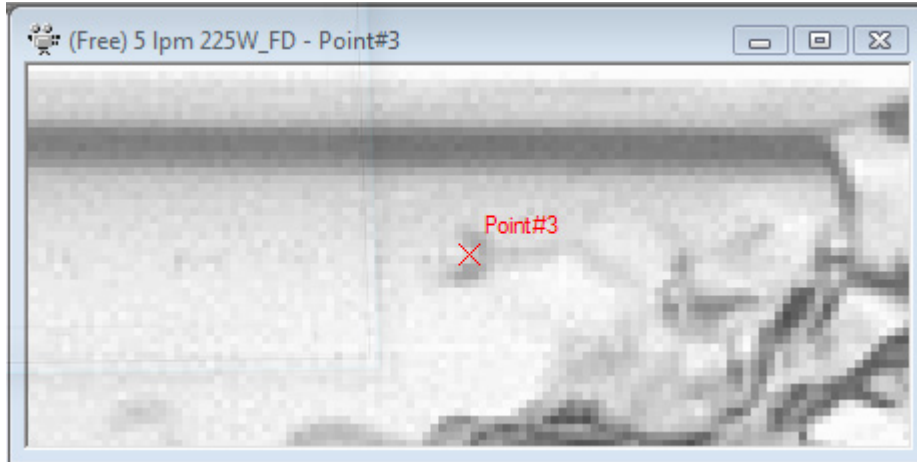
TEMA Motion allows the user to automatically track certain features. However with the two-phase flow system, the tracking software can get easily confused because at times there is not a sharp contrast between what we are tracking and the background. As a result the automatic tracking feature can be used, but be sure to monitor closely what the program is tracking to ensure that it has not wandered away from the intended feature. To help combat this, the user can automatically track one frame at a time.

14. Tracking features with automatic tracking (a) or frame by frame tracking (b)

   a. To automatically track the feature as fast as the video plays, click . Be sure to watch closely what is being tracked and be ready to click pause if it begins tracking the wrong feature. Be sure to act quickly as this automatic tracking feature can run out of control quickly if not monitored. This tracking type is usually best to use with solitary features such as a single wave front or single vapor bubble where there are not many other features that can confuse the TEMA software.

   b. A safer but potentially more tedious option is to automatically track each feature one frame at a time. If you only wish to track one frame at a time click .

      i. Sometimes the automatic tracking tracks the feature closely, but does not track the exact location frame after frame. As a result sometimes the user may need to manually correct the location of the automatically tracked point. To do this pause the video by clicking and click the correct location of the point. You can flip quickly between the current frame and the previous from by clicking (previous frame) or (next frame). Tracking the exact location typically smooths out the position and velocity graphs as well as provides a more accurate result. Continue tracking the feature for as long as you would like for analysis.

15. If at any time you track a point additional frames that you do not need or want to clear any tracking that you have done in a section of film, you can unregister the points in a selected interval of the video.

a. To do this, go to the first frame that you wish to remove the tracking from. In the time panel slider,

hold the **Shift** key while dragging the slider between the first and the last sample in the interval. This will highlight a section in the time panel slider as well as in the graphs.

b. In the test contents window, **right click** the point that you wish to unregister the tracked data during this interval. Click **Unregister in Selected Interval**.
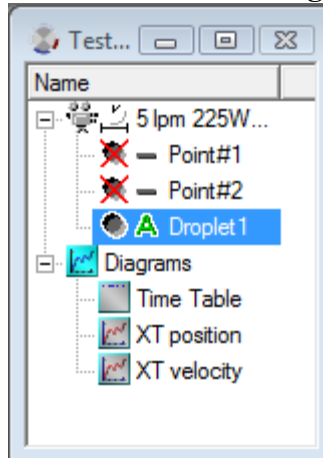
16. You can rename the feature that you are tracking by going into the Test Contents window and clicking the name of the point once. This can be useful for categorizing tracked points as well as during post analysis in Microsoft Excel to avoid confusion between tracked points.

17. After tracking of the feature is complete, and you would like to move onto another feature, disable the point by selecting the point and pressing **CTRL+D** or by clicking

 on the toolbar. This is key when tracking multiple points, otherwise TEMA will request a position for each active point every frame that a feature is being tracked.

18. For tracking additional points, repeat steps 12-17.

19. At times the graphs repeat colors of points which can make it confusing when trying to analyze the graphs. As a result, in the properties (select graph and press **ALT+P**) the colors of each point can be altered to make graphs clear and easy to understand. To change the color, right click the color in the properties box and a drop down menu will provide colors to choose from. Click **OK** to close the window.

DISTRIBUTION STATEMENT A: Approved for public release. Distribution is unlimited.
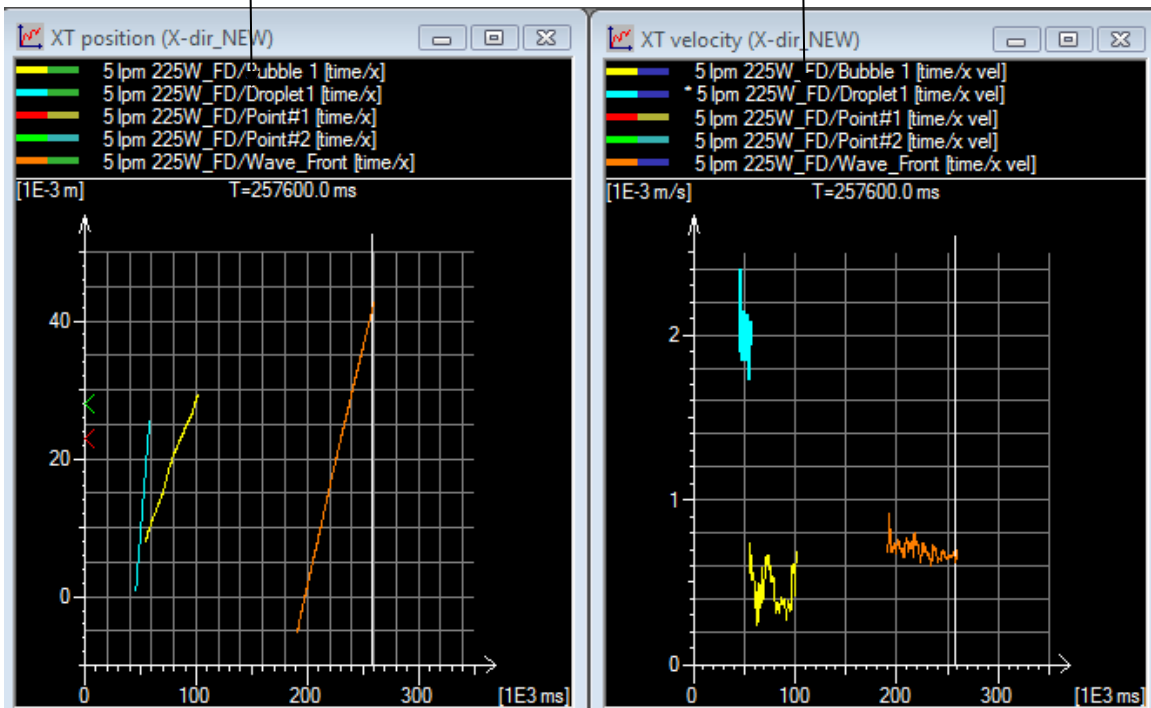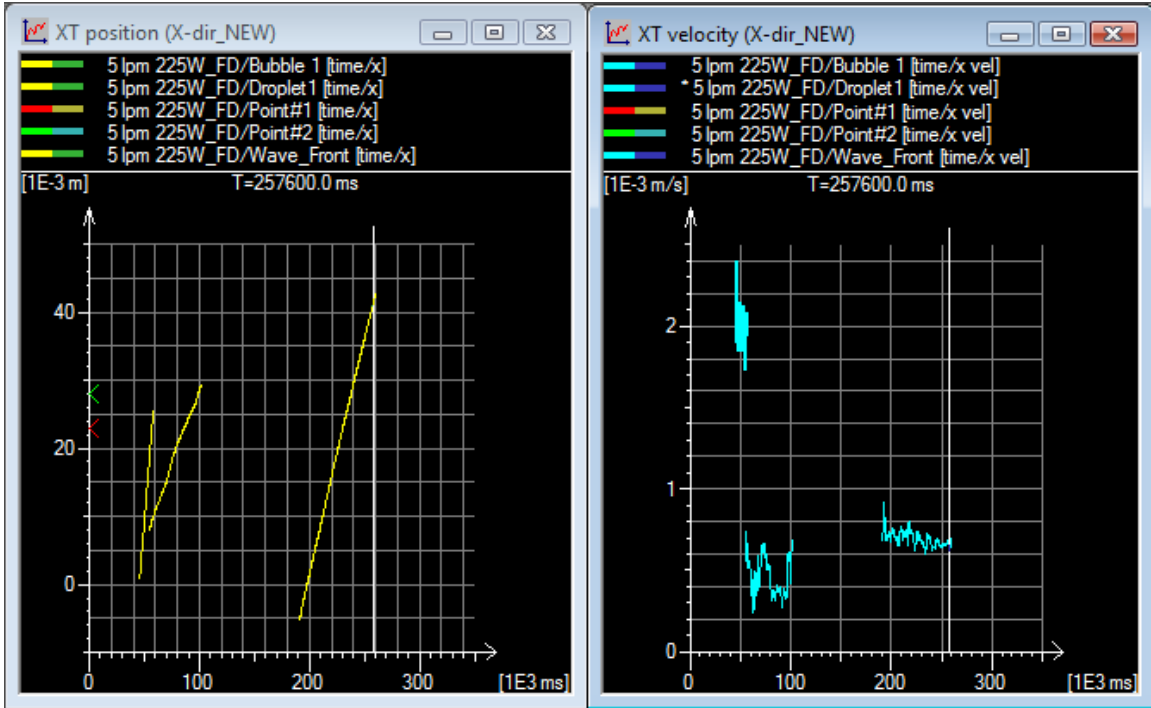
20. Click anywhere in the Time Table seen below and press **ALT+P** to open up the properties dialogue box for the Time Table.
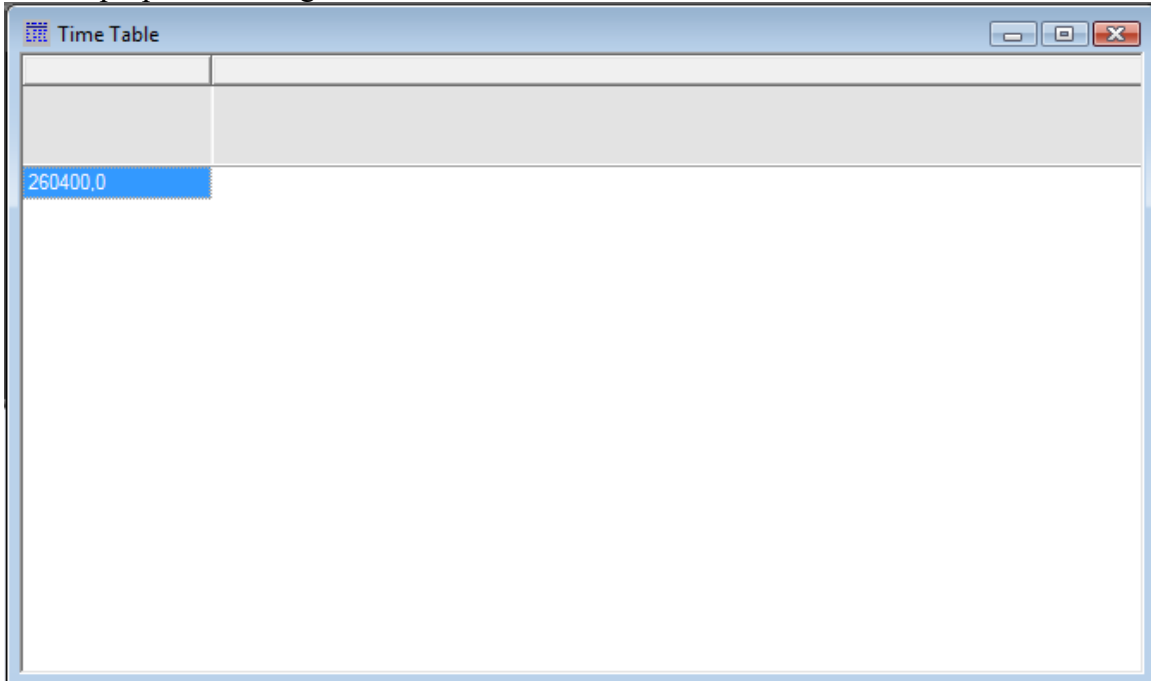
a. In the Time Tables Properties box, you can select which tracked points you would like data for.
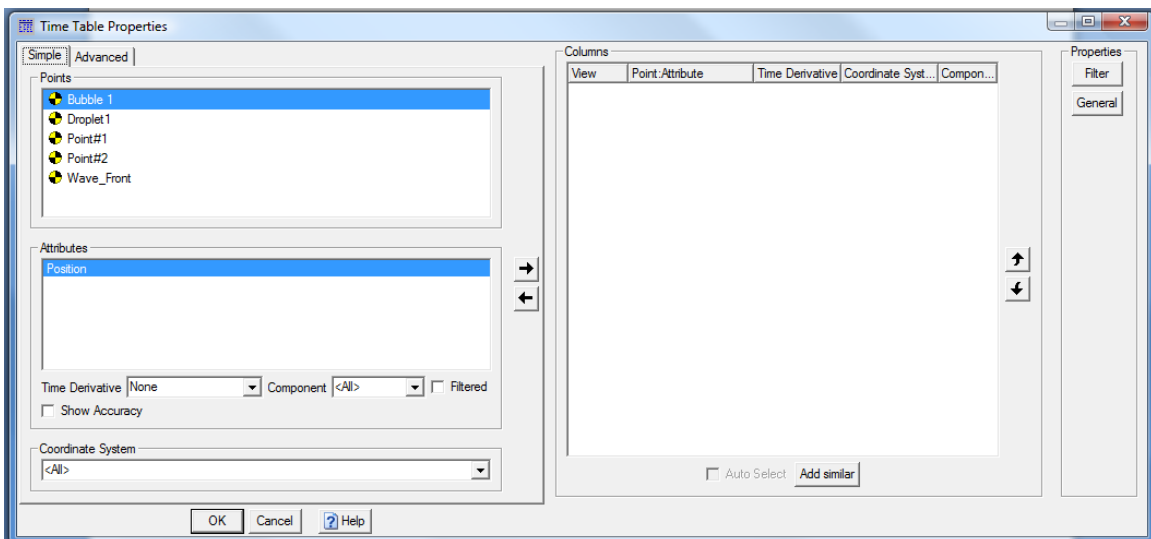
b. Select each point that you have tracked excluding Point#1 and Point#2 since those were used as reference points. In this example the tracked points are Bubble 1, Droplet 1, and Wave_Front.

c. Under **Time Derivative:** use the drop down menu to select Velocity.

d. Under **Component**, select x.

e. Under **Coordinate System**, select the coordinate system that we created earlier, in this case, X-dir_NEW. Click the right arrow to transfer the x component of the velocity data from all three points that was recorded in the new coordinate system

DISTRIBUTION STATEMENT A: Approved for public release. Distribution is unlimited.

into a table similar to Excel. Click **OK** to close. The data should automatically populate the Time Table.

1	CS1:1	CS2:1	CS3:1	
Time	Velocity (Default/Bu...	Velocity (Default/Dr...	Velocity (Default/W...	
	x[m/s]	x[m/s]	x[m/s]	
[ms]	X-dir_NEW(5 lpm 2...	X-dir_NEW(5 lpm 2...	X-dir_NEW(5 lpm 2...	
257600,0	-	-	0,00062104	
257800,0	-	-	0,00062876	
258000,0	-	-	0,00063185	
258200,0	-	-	0,00063456	
258400,0	-	-	0,00064344	
258600,0	-	-	0,00065347	
258800,0	-	-	0,00066139	
259000,0	-	-	0,00066622	
259200,0	-	-	0,00068185	
259400,0	-	-	0,00069054	
259600,0	-	-	0,00068591	
259800,0	-	-	0,00068436	
260000,0	-	-	0,00067730	
260200,0	-	-	0,00067838	
260400,0	-	-	-	

21. Transferring Data from Time Table into Microsoft Excel
    a. Click anywhere in the Time Table window and select all of the data by pressing **CTRL+A**.
    b. Copy all of the data.
    c. Paste data into a new Microsoft Excel workbook.
    d. All of the data that is copied over will contain an "X" where there is no recorded data and a "," as a decimal point. In order to correct this, press **CTRL+F** to open up a find and replace window.
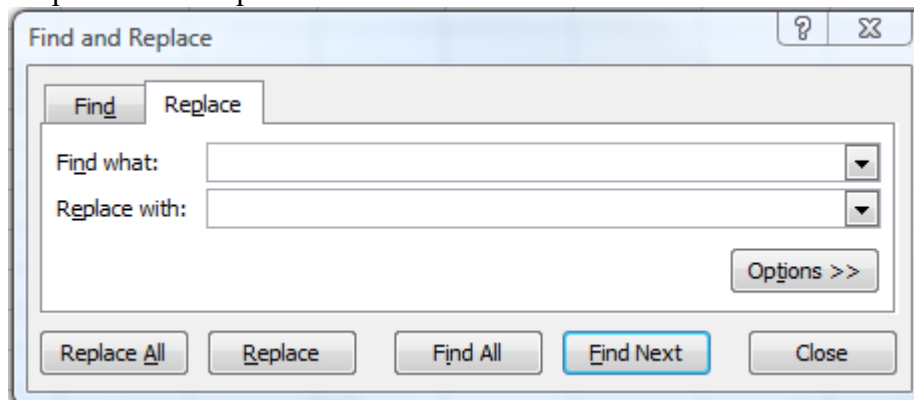
    e. In the **Find what:** box, type in "," without the quotes. In the **Replace with:** box, type in "." without the quotes and click **Replace All.** This will replace every "," with a "." Throughout the worksheet.
    f. In order to get rid of the "X", open the options by clicking the **Options >>** Button.
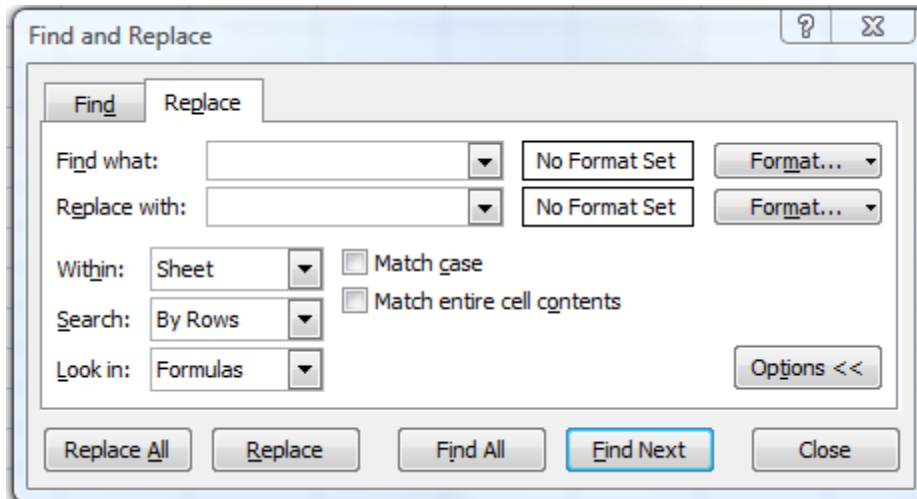
g. In the **Find what:** box, type in "X" without the quotes. Leave the **Replace with:** box empty.

h. Select the box to **Match case,** and click **Replace All**. This will remove every "X" in the worksheet and allow the user to manipulate the data like any other Excel worksheet.

22. Once in Excel and having repaired the "X" and ",", graphs can be made to display the data following standard Excel procedures.